# Stability Analysis
# of the High Performance
# Light Water Reactor

**T. Ortega Gómez**

**Institut für Kern- und Energietechnik**

# Stability Analysis of the High Performance Light Water Reactor

**Tino Ortega Gómez**

Institut für Kern- und Energietechnik

von der Fakultät für Maschinenbau der

Universität Karlsruhe (TH) genehmigte Dissertation

# Stabilitätsanalyse
## des
# High Performance Light Water Reactor

## Kurzfassung

Im Rahmen des internationalen Forschungsprogramms zur Entwicklung innovativer Kernreaktoren, Generation IV, ist der High Performance Light Water Reactor (HPLWR) einer der viel versprechenden Kandidaten. Für diesen Leichtwasserreaktor ist ein überkritischer Betriebsdruck vorgesehen. Der Einsatz von Technologien mit überkritischen Dampfzuständen ist im konventionellen, kohleverfeuernden Kraftwerksbereich wohlbekannt und führte zu hohen Wirkungsgraden (von bis zu 45 %).

In einem HPLWR-Brennelement wird das überkritische Fluid von 280 °C bis 500 °C erhitzt. Diese Aufheizung hat eine starke Änderung der thermohydraulischen Eigenschaften und der Transporteigenschaften zur Folge. Insbesondere fällt die Kühlmitteldichte von 780 kg/m³ auf 90 kg/m³. Somit übersteigt die Dichteänderung diejenige, welche in Siedewasserreaktoren (SWR) vorzufinden ist (ca. 750 kg/m³ bis ca. 198 kg/m³). Auf Grund dieser Tatsache wird für den HPLWR das Aufkommen von Strömungsinstabilitäten in Betracht gezogen. Durch Maßnahmen bei der Auslegung müssen Strömungsinstabilitäten im späteren Betrieb vermieden werden.

In dieser Doktorarbeit wird eine Stabilitätsanalyse für den HPLWR vorgestellt. Sie basiert auf analytischen Überlegungen und numerischen Ergebnissen, für die ein eigener Computercode entwickelt wurde. Als Softwareplattform diente hierbei COMSOL, was eine stationäre, zeitabhängige und Eigenwertanalyse ermöglicht. Der HPLWR zeichnet sich durch ein innovatives Aufheizschema des Kühlmittels aus. Zunächst werden die bezüglich relevanter Strömungsinstabilitäten kritischen Komponenten des Aufheizschemas ermittelt. Die Brennelemente werden numerisch mit einem Satz eindimensionaler gekoppelter Erhaltungsgleichungen wiedergegeben. Diese Methode wird bereits erfolgreich für die Stabilitätsanalyse an SWR eingesetzt.

Eine stationäre Parameterstudie des thermohydraulischen Systems ergibt, dass das Aufkommen von Ledinegginstabilitäten, Massenstromfehlverteilungen und Dichtewellenoszillationen unter HPLWR-Bedingungen ausgeschlossen werden kann. Des Weiteren werden drei Arten von Dichtewellenoszillationen (DWO) untersucht: die Einkanal-DWO, die nuklear gekoppelt gegenphasige DWO und die nuklear gekoppelte DWO in Phase. Hierbei wird eine lineare Stabilitätsanalyse im Frequenzraum vorgenommen. Die Ergebnisse werden in Stabilitätskarten wiedergegeben, in denen linear stabile und linear instabile Betriebszustände unterschieden werden. Diese Stabilitätskarten werden von neuen Kennzahlen für überkritische Fluide aufgespannt, welche sich für unterkritische Drücke auf die bekannten Kennzahlen für Zweiphasenströmungen reduzieren lassen. Die Effekte von Auslegungs- und Betriebsparameter auf die Stabilitätsgrenze werden in einer Sensitivitätsstudie aufgezeigt und diskutiert. In einer zeitabhängigen Analyse werden nichtlineare Phänomene untersucht und ein Verzweigungsdiagramm ermittelt. Im HPLWR werden neun Brennelemente zu einer funktionalen Einheit - dem so genannten Brennelementbündel - zusammengefasst. Dies stellt aus strömungsmechanischer Sicht einen Verbund von neun parallelen Kanälen dar, welche durch ein gemeinsames Zwischenplenum ge-

koppelt sind. In einer Mehrkanalanalyse wird aufgezeigt, dass eine Gemeinschaftsblende am Eintritt des Zwischenplenums keinen stabilisierenden Effekt hat. Zur Untersuchung nuklearer gekoppelter DWO-Moden wurde das thermohydraulische Modell um ein punkt-kinetisches Neutronikmodell erweitert. Es wird aufgezeigt, dass die aus den Rechnungen resultierenden Stabilitätsgrenzen der gekoppelten DWO-Moden näherungsweise mit der Einkanal-DWO übereinstimmen.

Aus den zahlreichen Analysen ergeben sich neue Richtlinien bei der konstruktiven Auslegung des HPLWR. Hierbei werden, ähnlich dem Vorgehen bei SWR, Einlassblenden für die Brennelemente des Verdampfers ausgelegt, wodurch ein sicherer Betrieb für den HPLWR gewährleistet wird.

# Abstract

In the Generation IV international advanced nuclear reactor development program, the High Performance Light Water Reactor (HPLWR) is one of the most promising candidates. Important features are its inherently high thermodynamic efficiency (of approximately 45 %) and the ability to use existing supercritical water technology which previously has been developed and deployed for fossil fired power plants.

Within a HPLWR core, the fluid experiences a drastic change in thermal and transport properties such as density, dynamic viscosity, specific heat and thermal conductivity, as the supercritical water is heated from 280 °C to 500 °C. The density change substantially exceeds that in a Boiling Water Reactor (i.e., HPLWR: density changes from 780 kg/m$^3$ to 90 kg/m$^3$; BWR: density changes from 750 kg/m$^3$ to 198 kg/m$^3$). Due to this density change, the HPLWR can be - under certain operation parameters - susceptible to various thermal-hydraulic flow instabilities, which have to be avoided.

In this thesis a stability analysis for the HPLWR is presented. This analysis is based on analytical considerations and numerical results, which were obtained by a computer code developed by the author. The heat-up stages of the HPLWR three-pass core are identified in respect to the relevant flow instability phenomena. The modeling approach successfully used for BWR stability analysis is extended to supercritical pressure operation conditions. In particular, a one-dimensional equation set representing the coolant flow of HPLWR fuel assemblies has been implemented in a commercial software named COMSOL to perform steady-state, time-dependent, and modal analyses.

An investigation of important static instabilities (i.e., Ledinegg instabilities, flow maldistribution) and Pressure Drop Oscillations (PDO) have been carried out and none were found under operation conditions of the HPLWR. Three types of Density Wave Oscillation (DWO) modes have been studied: the single channel DWO, the core-region-wide out-of-phase DWO, and the in-phase DWO. As a first step, the linear stability characteristics of a typical fuel assembly were computed by evaluating the eigenvalues of the thermal-hydraulic model. The results of the analysis are presented in stability maps to define stable and unstable operation points of the HPLWR. This stability maps are expanded by new characteristic numbers which have been derived for fluids at supercritical pressure conditions. For subcritical pressures, these new non-dimensional numbers are related to the well known non-dimensional groups of phase change systems. The sensitivity on various design and operation parameters of the stability limits have been investigated, and the results are summarized in a table. Non-linear phenomena were investigated in the time domain. Complicated mixed supercritical bifurcations were found and the resulting limit cycles were evaluated.

In a HPLWR core, nine fuel assemblies form one functional unit: the fuel assembly cluster. This special design feature can be seen as an array of nine coupled parallel flow channels with a common intermediate inlet plenum. By extending the thermal-hydraulic model, it has been shown that a common inlet orifice has almost no effect on the onset of density wave oscillations. Furthermore, the thermal-hydraulic model was coupled with a point-kinetic neutronic model via a heat transfer model. It was found out that the threshold of instability is approximately at the same values of Pseudo-Phase-Change-Numbers for all three types of DWO modes.

As a consequence of the various analyses, it has been shown, while no inlet orifices are required for the fuel assemblies of the superheaters, the fuel assemblies of the evaporator

must have single inlet orifices at the entrance of each fuel assembly (in respect to avoid DWOs). To design these inlet orifices, the stability criteria for BWRs have been extended for the HPLWR.

# Contents

# 1 Introduction

Mankind is expected to increase from about six billion individuals today to ten billion people in 2050 [52]. This fact results in big challenges for politicians and scientists not only in respect to alimentation and habitation; the standard of living is directly correlated with the consumption of power. This is shown quite plainly by a satellite picture of the Korean peninsular at night (Figure 1.1) [68]. No other border of the world separating the rich and the poor can be seen that spectacularly from space. South Korea is one of the four "Tigers". An example of a former emerging nation, which successfully developed to a country with a high income per person, excellent health care, education, and very broad distribution of advanced technology. In clear contrast, North Korea is a third world country, where the population lives with disastrous health care, with dearths and an approximately fifteen years minor expectancy of life compared to the the rich brothers in the south. As Japan, South Korea appears brightly lightened at night. The light of millions of bulbs illustrates the prosperity which comes with electricity.

In the next decades first world countries like the USA and the countries in the European Union will still increase their consumption of electricity. Due to the fast industrializing populous countries like India and China, the global increase will be even more drastic. Remembering the humanistic tradition of our universities, it must be one of our goals to provide at least the same life standard we enjoy today not only to western countries, but the whole mankind.

Scientists find more and more evidence that the emission of anthropogenic $CO_2$ is the main reason for global warming, a scenario which is threatening not only countries with low coast lines but maybe the whole mankind. $CO_2$ is emitted by traffic and industry due to the combustion of fossil fuels, but mainly for heating and electrical power production. This way, mankind emits about 8 billion tons of $CO_2$ into the atmosphere for electricity every year. Currently, about 436 nuclear power reactors, most of them Pressurized Water Reactors (PWRs) and Boiling Water Reactors (BWRs), are in operation, generating reliable electricity for more than 1 billion people without emitting $CO_2$. This saves about 2.5 billion tons of $CO_2$ per year [34].

The strong economic and safety performance of the deployed nuclear reactors, the growing demand for energy, and the increasing awareness of the environmental benefits of clean nuclear power form the foundation for a nuclear energy renaissance in the $21^{st}$ century, which can be seen in the extension of the operation period of existing plants up to 40 or 60 years. Furthermore, there are 29 nuclear power plants under construction worldwide and more than 40 are planned. Most of the near-future nuclear reactors are referred to as Generation III reactor types. Besides this development, nuclear experts around the world research on more ambitions and innovative projects: the development of an entirely new generation of nuclear power reactors, the Generation IV.

Figure 1.1: Satellite image of the region around the Korean peninsula.

## 1.1 Supercritical Water Reactor

In 2001 the United States, the United Kingdom, Switzerland, South Korea, South Africa, Japan, France, Canada, Brazil and Argentina founded the Generation IV International Forum (GIF) [69]. This research foundation has the task to evaluate and prioritize next-generation nuclear reactor technologies that have strong potential to be more economical, allow safer operation, are more sustainable, and more proliferation resistant than existing technologies. The GIF established a road map to focus the research activities on the six most promising reactor technologies: the Gas-Cooled Fast Reactor (GFR); the Sodium-Cooled Fast Reactor (SFR); the Lead-Cooled Fast Reactor (LFR); the Very High Temperature Reactor (VHTR); the Molten Salt Reactor (MSR); the Supercritical Water Reactor (SCWR).

A light water reactor concept with supercritical pressure conditions is called SCWR. Water at a pressure and temperature above its critical point ($T_C = 373.9\,°\text{C}$, $p_c = 22.06\,\text{MPa}$) is called supercritical. The use of supercritical water as working fluid is well established for Fossil Fired Power Plants (FFPP). For FFPP one can see the tendency to higher thermal efficiency by increasing system pressure and steam temperature over the last decades to enhance the net efficiency. Today, newly installed FFPP use live steam temperatures and system pressures of up to 600 °C and 30 MPa with a net efficiency of around 46 %. On the other hand, even the most advanced modern nuclear reactors like the European Pressurized water Reactor (EPR) are deployed with a net efficiency of only 36-37 % [24]. In that sense the SCWR is a logical evolutional step of nuclear reactor technologies. Since the water does not undergo a phase change, a SCWR operates at a high temperature level without exhibiting the "Departure of Nuclear Boiling (DNB) problem", which limits
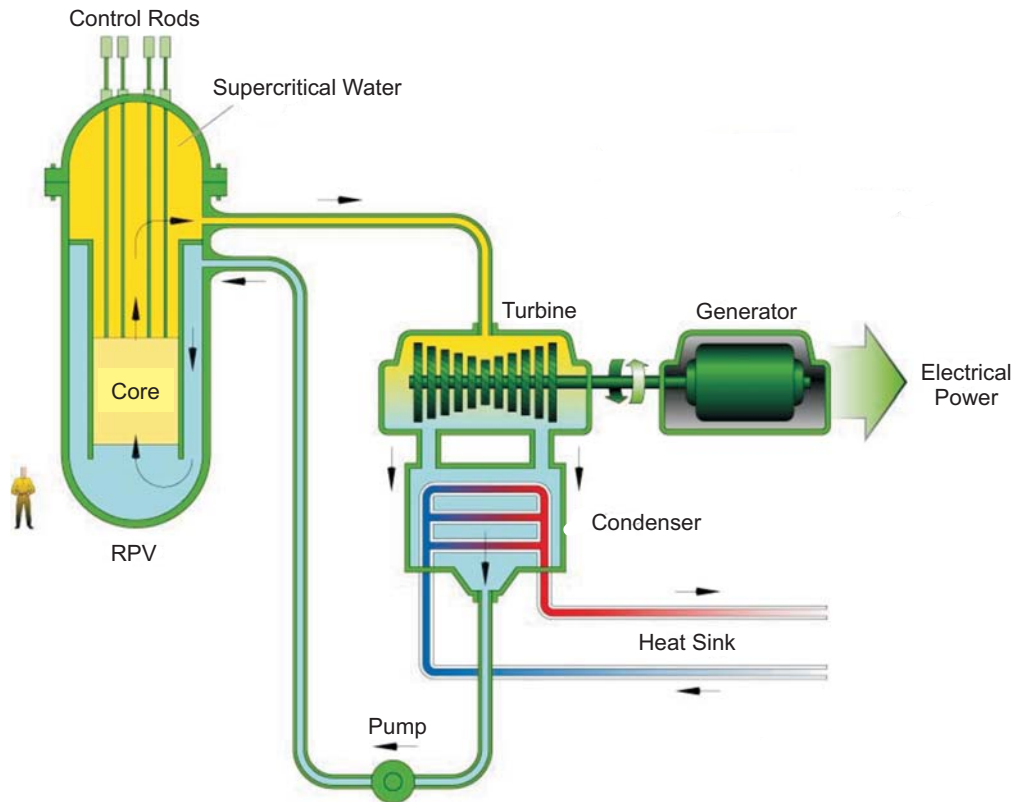
Figure 1.2: Simplified plant scheme of a SCWR. On the left hand side there is the Reactor Pressure Vessel (RPV). In a once-through cycle the fluid at supercritical pressure conditions flows from the reactor core through the turbine, and the condenser to the feed water pump, and back into the RPV.

the Boiling Water Reactors (BWR) in their exit temperature level. Furthermore, steam water separation and recirculations pumps are not necessary which contributes to considerable plant simplifications and compact design. Figure 1.2 shows a schematic layout of a SCWR plant. Light water at a system pressure of 25 MPa is pumped with an average temperature of 280 °C into the reactor pressure vessel. It flows through the reactor core, where it undergoes an average heat up to 500 °C [61]. The hot steam is guided directly to the turbine (direct cycle or once-through cycle), where no steam-water seperation is needed [8]. The turbine drives a generator which provides electrical power. Behind the turbine the working fluid subsequently flows through the condenser and finally back to the feed water pump.

Note that, besides the pressure vessel concept (like SCWR) shown in Figure 1.2, pressure tube (see: Figure 1.3 [73]) reactor concepts are projected. The Generation IV CANDU Super Critical Water Reactor has multiple pressure tubes, rather than a single pressure vessel [67]. Inside the pressure tubes, the fuel elements are located. A CANDU-like reactor is designed to use natural uranium as its fuel, since the pressure tubes are surrounded by a large volume of cool heavy-water moderator within the core.
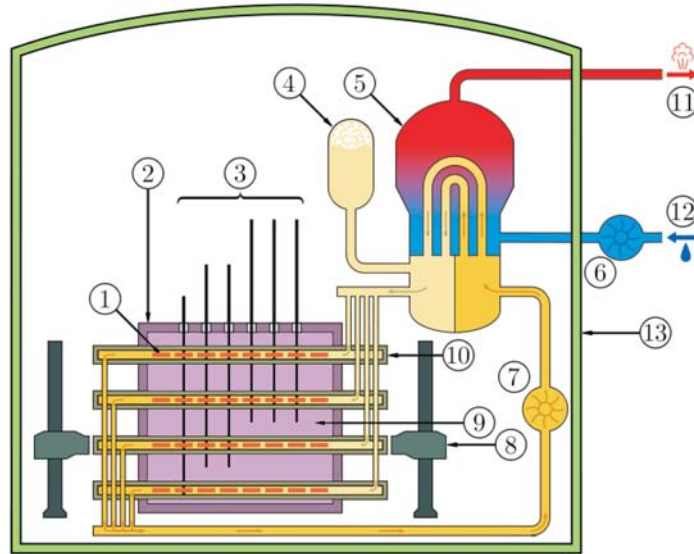
Figure 1.3: Schematic diagram of the pressurized heavy water cooled version of a CANDU (CANada Deuterium-Uranium) nuclear reactor [73]. Labels: (1) nuclear fuel rod, (2) calandria, (3) control rods, (4) pressurizer, (5) steam generator, (6) light water condensate pump (secondary cooling loop), (7) heavy water pump (primary cooling loop), (8) nuclear fuel loading machine, (9) heavy water (moderator), (10) pressure tubes, (11) steam, (10) water condensate,(13) reactor containment building.

## 1.2 Water at Supercritical Pressure Conditions

The equilibrium state of a substance plotted on a pressure-temperature graph is called a phase diagram. Figure 1.4 schematically shows the phase diagram of water. The green line in the diagram is the melting line - it separates ice from liquid water - and the blue line is the boiling line, which separates the vapor phase and the liquid phase. The red line is the so-called sublimation line, along which ice transforms directly to the gaseous state, without the intermediate step of liquid water. All three lines meet at a unique point, which is called the triple point. At this temperature and pressure, all three forms of water can coexist. The second remarkable point is the thermodynamic critical point at the upper end of the boiling line. For water it is found at the critical pressure $p_c = 22.06$ MPa and critical temperature $T_C = 373.9$ °C. The thermodynamic critical point is unique for every substance. A fluid at a temperature or pressure above its thermodynamics critical point is called supercritical fluid (yellow region). At the critical point, the densities of the subcooled liquid and the saturated vapor become identical, resulting in a single phase supercritical fluid. Hence, there is no phase change for supercritical fluids. This fact can be heuristically explained on a microscopic scale. If steam is exposed to rising pressure, the distance between the water molecules gradually decreases. As the critical point is reached, the distance between the molecules of the gas phase equals the distance of molecules of the liquid phase. Hence, no difference in phases (or phase-change) can be observed. However, large variations in the physical properties are an inherent nature of supercritical fluids. The most striking variation is observed for the specific heat capacity (Figure 1.5) (data: IAWPS-IF97 [72]). Its maximum value for various pressures defines
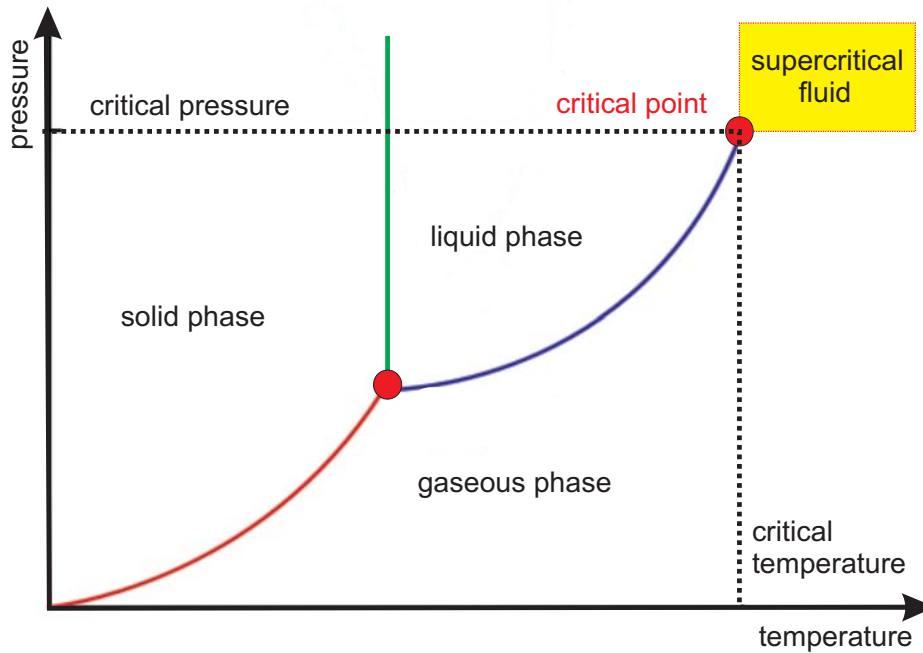
Figure 1.4: Scheme of the phase diagram for $H_2O$. The melting line is given in green. The red line is the sublimation line. The thermodynamic critical point is the upper end of the boiling line (at $p_c = 22.06$ MPa, $T_C = 373.9$ °C).

the pseudo-critical line. For the system pressure of the HPLWR we have a pseudo-critical temperature of $T_{PC} = 385$ °C. Fluid properties around the pseudo-critical temperature have a highly non-linear temperature dependency, which have to be taken into account for thermal-hydraulic analysis of industrial supercritical pressure systems.

## Denotation

Note that the terms "subcritical" and "supercritical" are common in different scientific fields which come together in the context of this thesis. On one hand, the terms are used in the thermodynamic sense indicating fluid state: e.g. water at supercritical pressure conditions (Section 1.2) and - in the same context - water at subcritical pressure conditions (two-phase flow). On the other hand, in nonlinear dynamics, chaos, and bifurcation theory the terms "subcritical" and "supercritical" denote the regions below and above a critical parameter: e.g. subcritical and supercritical bifurcation branches (see Chapter 7). Furthermore, "subcritical" and "supercritical" is commonly in the field of nuclear physics. Here the smallest amount of fissile material needed to sustained a chain reaction is called critical mass. In that context a subcritical mass is a mass that does not have the ability to sustain a chain reaction. A supercritical mass is characterized by an increasing rate of fission. Also a nuclear reactor may have a subcritical or supercritical core (see Chapter 9).

For the sake of completeness it is noted that for the system pressure of a HPLWR (25 MPa) in strict thermodynamic sense the term supercritical water is only applicable for temperatures higher than $T_C = 373.9$ °C. Within the community of nuclear designers
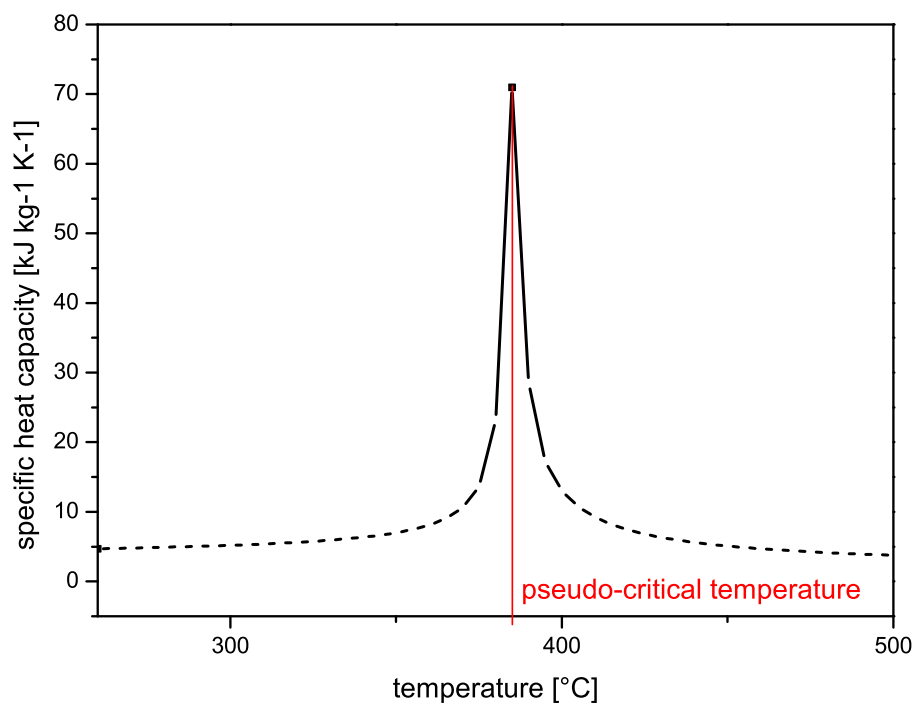
Figure 1.5: Specific heat capacity vs. temperature near the pseudo-critical point for water at 25 MPa. The peak of the specific heat capacity indicates the pseudo-critical point at $T_{PC} = 385$ °C.

the term supercritical water is used for the whole temperature range of a HPLWR.

## 1.3 High Performance Light Water Reactor

In the fifth framework program of the European Commission, the investigation of a SCWR concept is denoted High Performance Light Water Reactor (HPLWR). It is a nuclear reactor of the upper performance class with a projected electrical power around 1000 MW. This value can even be increased in further design steps. The prominent advantage of this reactor is its high thermal efficiency of approximately 45 % (for comparison: 33 % thermal efficiency for current deployed LWR). Bitterman et al. [7] compared the HPLWR to state of the art LWR and pointed out its strong economic merits. In detail, the HPLWR has projected low construction costs of around 1000 Euro per $KW_e$ due to size reduction of buildings and size reduced components, since the hot steam is directly fed to the high pressure turbine with enhanced steam enthalpy. The electricity production costs are expected within 3 to 4 cents per kWh. Even though some efforts were undertaken to investigate the possibility of a fast neutron spectrum, the majority of research groups focus on a reactor core with a thermal neutron spectrum. The HPLWR has a projected mass flow of 1160 kg/s [19].

For a deeper understanding of stability analysis for the HPLWR, which is the subject of the present investigation, it is necessary to get familiar with the basic principles of nuclear reactors and especially with the actual HPLWR design proposal [23].

Even though a nuclear reactor is often described as a "very complicated machine" in the media available for average educated people, it still can be viewed as a simple boiler, where its heating is provided by nuclear reaction rather than electric or fire heating in conventional boilers. The boiler is called reactor core. In modern Light Water Reactors the core is surrounded by a cylindrical object with a hemispherical shape on the top and bottom, the so-called reactor pressure vessel (RPV). The RPV is made of common vessel steel for pressurized water reactors. It forms one of various barriers preventing the escape of radioactivity into the environment. Figure 1.6 shows two cuts through the reactor pressure vessel (RPV) of the HPLWR. The RPV has a total height of 14.3 m and an outer diameter of approximately 5 m. The left figure illustrates some core internals (for a detailed and extended description see Fischer et al. ([20], [21], [22]). Marked with: (1) one of four inlets (with backflow limiter) for the working fluid; (2) one of four hot pipes, where the hot fluid is leaving the RPV to the turbines; (3) the upper mixing plenum; (4) one of three fuel assembly clusters illustrated in the figure.

The HPLWR has 1404 fuel assemblies (FA) in the reactor core. Fuel assemblies, or fuel elements, are the most important and characteristic components of a nuclear reactor. FAs contain the nuclear fuel needed for the nuclear chain reaction inside the so-called fuel rods. The HPLWR uses $^{235}U$ which is the most common fissile nuclear fuel for power reactors. In an early stage of SCWR investigation different FA geometries were proposed (e.g., [10], [45]). In the HPLWR, an optimized fuel assembly is projected [32]. Figure 1.7 shows a cut through one of those fuel assemblies. The quadratic moderator box is situated in the center. It has an edge length of 0.02688 m. Inside the moderator box the fluid is flowing downwards. The nuclear fission takes place in the fuel material (yellow). The fuel is surrounded by a small gap filled with noble gas and enclosed by a cladding preventing
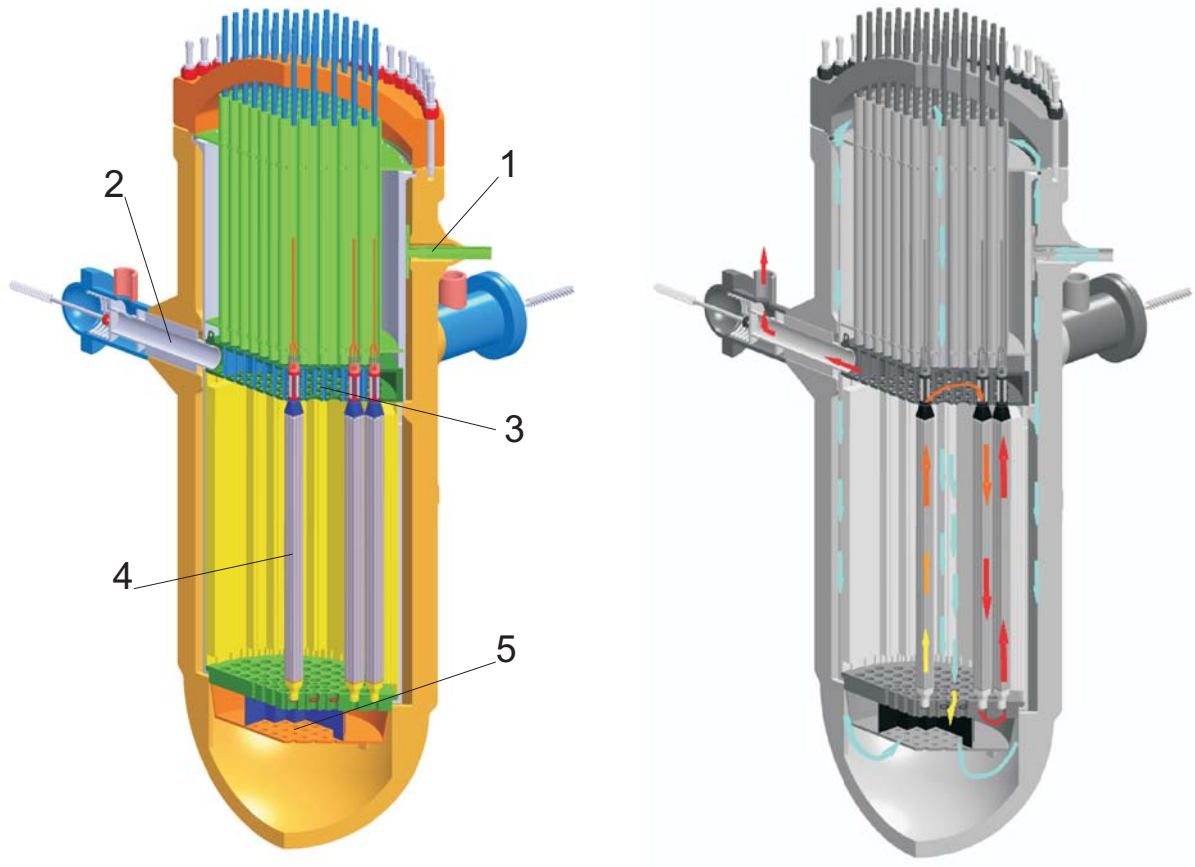
Figure 1.6: Cuts through the reactor pressure vessel of the HPLWR. On the left hand side: (1) one of four inlets for the working fluid; (2) one of four hot pipes; (3) the upper mixing plenum; (4) fuel assembly cluster; (5) lower mixing plenum. On the right hand side: scheme of the coolant flow in the RPV.
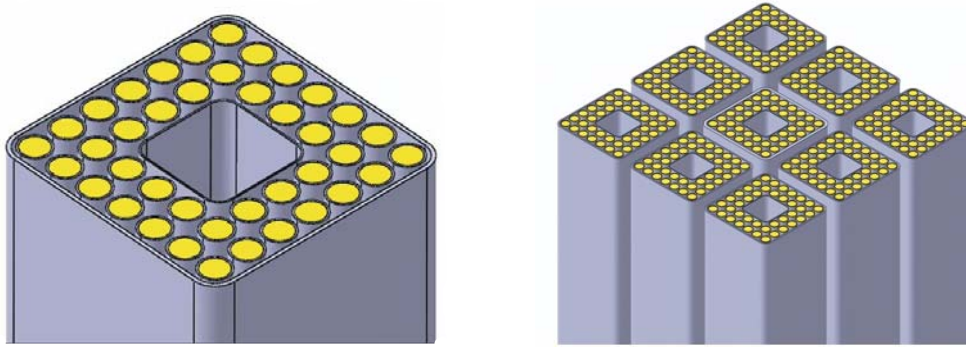
Figure 1.7: Cut through a fuel assembly of the HPLWR (left hand side). The quadratic moderator box is situated in the center. The fluid is flowing downwards herein. Forty fuel rods (in yellow) are located in two layers around the moderator box. Each fuel rod is surrounded by cladding material. Between the fuel rods, the coolant flows through the so-called sub-channels. Like in BWR the fuel assembly is surrounded by a fuel assembly box. Nine fuel assemblies form one fuel assembly cluster (right hand side).

that fuel escapes into the coolant. The composite of fuel, gas gap and cladding material is the fuel rod mentioned above. It has a total height of 4.71 m and an outer diameter of 8 mm. Fuel is not present within the total height of the fuel rod. The central part, where fuel is present and nuclear reactions take place, is called active length. The HPLWR has an active length of 4.2 m. Forty fuel rods are placed in two layers around the moderator box. Between the fuel rods, the coolant flows in sixty so-called sub-channels. As in BWR the fuel assembly is enclosed by a fuel assembly box which has an outer diameter of 76 mm. The cross-section of the flow area of one fuel assembly is 1831 mm$^2$. With a total heated perimeter of 1.005 m, this results in a hydraulic diameter of 5.336 mm. Each fuel assembly is surrounded by gaps, where water flows from top to bottom.

In a HPLWR core, nine fuel assemblies form one functional unit called fuel assembly cluster of which 156 exist within the core. The clustering allows the application of existing already-deployed control rod technologies, since the FA clusters have similar dimensions as fuel assemblies in BWRs. For the guidance of the coolant a foot piece and a head piece are situated on top and bottom of the fuel assembly cluster guiding the flow into a common volume at the inlet and outlet of each cluster.

The right hand side of Figure 1.6 illustrates the flow path inside the RPV. Several innovative ideas for the heat-up scheme of the working fluid are implemented in the design due to the special exigencies of supercritical water. In Figure 1.8, the density change of the fluid is plotted vs. the temperature range occurring inside the reactor pressure vessel (RPV). During the heating from 280 °C up to 500 °C the density decreases from approximately 780 kg/m$^3$ to 90 kg/m$^3$. This would result in an undermoderation of the reactor core in the low density region of the coolant [17]. Additional cold water is needed in the upper part of the core. Therefor, the total mass flow of 1160 kg/s coming from the feed water pump with a temperature of 280 °C is split into two streams after the entrance into the RPV (right hand side of Figure 1.6). 25 % of the water flow upwards to the upper plenum. Further, the water streams downwards between the control rod guide tubes and the upper RPV internals. Before entering the HPLWR core this water is split again. 66.7 %, or in mass flow 183.3 kg/s, passes the core from top to the bottom as

gap water between the fuel assemblies. The other 33.3 % (96.67 kg/s) of the total flow become moderator water flowing downwards inside the moderator box. In comparison to BWR, HPLWR has a counter courant flow of gap and moderator water. In a BWR the moderator and gap water flows upwards through the core where it finally rejoins unified with the coolant in the steam plenum. This reduces the average temperature - and the thermal efficiency of the plant - of fluid at the exit of the RPV since the colder moderator and gap water is mixed with the hot coolant.

The other 75 % (or 870 kg/s) of the fresh water at the entrance of the PPV flow downwards through the downcomer to the lower plenum. In the lower mixing zone (point 5 of Figure 1.6) the downcomer water is mixed with the hotter gap and moderator water, resulting in an average fluid temperature of 310 °C [57].

Note that in a nuclear reactor core not all fuel assemblies operate with the projected desired operating point. Deviations of parameters from their average values in the manufacturing, construction and controlling of core lead to local deviations from the average operational regime. It is essential to estimate the potential of such operational deviations in order to be able to operate reactors safely, not exceeding allowable temperature limits. A hot-channel factor analysis provides a quantitative estimate of the safety margin in the thermal design [60]. In the case of the HPLWR it was found that a heat up of the coolant from 280 °C to 500 °C in one single step would locally exceed the temperature limits of the core internals (in detail: max. cladding temperature of 620 °C) [31]. Therefore, in a HPLWR the coolant is heated in three stages. Between these three stages, there are two intermediate mixing zones. At that way the coolant flow from fuel assemblies with an enthalpy rise in respect to the operating point - the so-called hot spots - will be homogenized in temperature. Hence, an intermediate mixing leads to a more uniform heating and avoids hot spots. Figure 1.9 shows a scheme of the the coolant flow in the III-pass-core. In the center of the core, 52 fuel assembly clusters form the first heat-up stage. Following the denotation of FFPP they are called evaporator. After gap, moderator and downcomer water has been mixed, it flows upwards as coolant into the evaporator with an average entrance temperature of 310 °C. It will be heated up to a average temperature of 390 °C. The corresponding density change is 724 kg/m$^3$ at the entrance down to 215 kg/m$^3$ at the exit of the evaporator. Next, the coolant will be mixed in the upper mixing zone before it flows downwards through the second heat-up stage, the so-called superheater I. The superheater I consists of 52 fuel assembly clusters surrounding the center zone of the core. After the superheater I the coolant will have an average temperature of 435 °C and a density of 121 kg/m$^3$. Following the flow schema, the coolant flows through a third mixing zone before it rises through the superheater II into the steam plenum. The superheater II is composed of 52 fuel assembly clusters arranged in an outer cycle around the superheater I. From the steam plenum the coolant flows directly to the turbines with a projected average temperature of 500 °C and a corresponding density of 90 kg/m$^3$. The relevant geometry and design parameters of HPLWR are listed in Table 11 in the appendix.
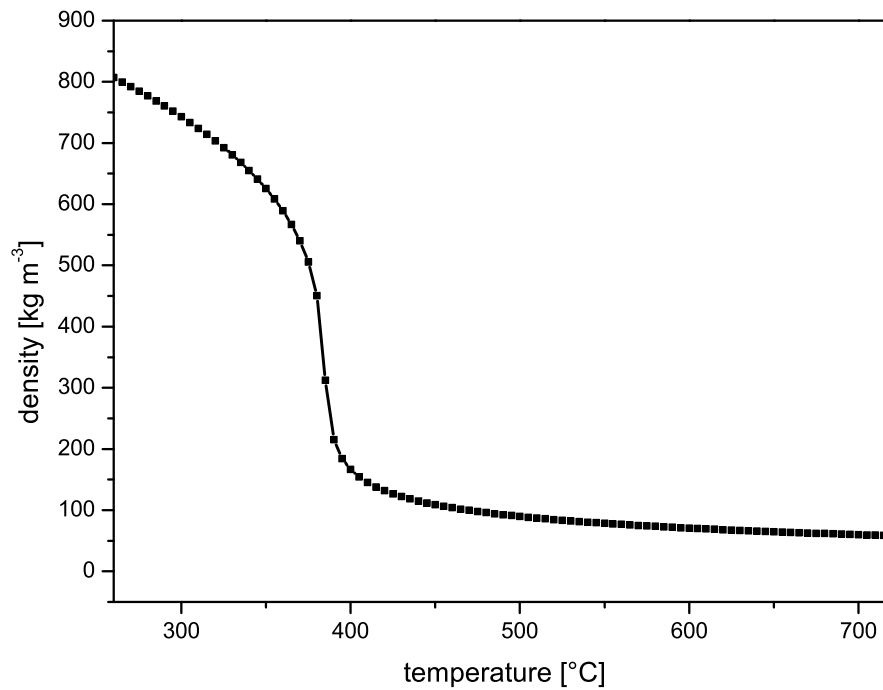
Figure 1.8: Density of water at a pressure of 25 MPa for the temperature range of HPLWR core (in particular: 280 °C - 500 °C). The density decreases from about 780 kg/m$^3$ to about 90 kg/m$^3$.
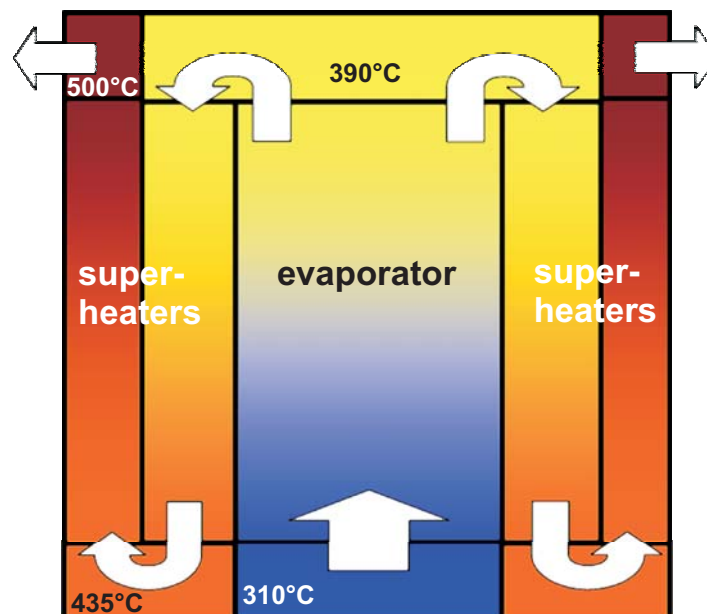


Figure 1.9: Scheme of the the coolant flow in a HPLWR III-pass core. In the center the evaporator; then, the so-called superheater I and superheater II. Between every heat-up stage a mixing zone is situated.

Table 1.1: Temperature range and density change of HPLWR heat-up components.

|  | average FA | | hot FA | |
| --- | --- | --- | --- | --- |
|  | temperature | density | temperature | density |
| evaporator | 310 - 390 °C | 724 - 215 kg/m$^3$ | 310 - 576 °C | 724-74 kg/m$^3$ |
| superheater I | 390 - 432 °C | 215 - 121 kg/m$^3$ | 390 - 604 °C | 215-70 kg/m$^3$ |
| superheater II | 433 - 500 °C | 120 -  90 kg/m$^3$ | 433 - 616 °C | 120-69 kg/m$^3$ |

# 1.4  Similarities of Sub- and Supercritical Water

Boiling flow in water-cooled reactors is susceptible to various thermal-hydraulic instabilities. These flow instabilities have to be avoided since they degrade reactor control and performance, and they erode thermal margins, which in the worst case will lead to mechanical damage of the core structure. The knowledge of the stability threshold and the design parameters for their avoidance is essential for secure operation of modern BWRs. The main reason for the susceptibility to instabilities lies in the density change correlating with the phase change of boiling water. To illustrate this feature, in Figure 1.10 the specific volume is plotted versus enthalpy for a two-phase system at a pressure of 7 MPa representing typical operation conditions for a BWR. The specific volume, $v$, is defined with the density, $\rho$, as:

$$v = \frac{1}{\rho} \quad . \tag{1.1}$$

Water has constant specific volume in the region of subcooled liquid. Rising the enthalpy and passing the fluid state of saturated liquid (with specific volume of saturated liquid $v_f$) a linear slope in specific volume can be observed. In a HPLWR core the fluid experiences a drastic change in density as the supercritical water is heated from 280 °C to 500 °C. The density change substantially exceeds that in a BWR (i.e., HPLWR: density changes from 780 kg/m$^3$ to 90 kg/m$^3$; BWR: density changes from 750 kg/m$^3$ to 198 kg/m$^3$). Even though water at supercritical pressure conditions is a single phase fluid, the physical features of the specific volume plotted vs. enthalpy show remarkable similarities to the conditions of two-phase systems (Figure 1.11). For the low enthalpy values of HPLWR a region of low and nearly constant specific volume can be seen. Heating the water across its pseudo-critical point, specific volume rises with a linear slope.   The striking similarities of water flow under subcritical and supercritical pressure conditions, the research of flow instability phenomena is an important issue for the HPLWR project.  The most susceptible core components are those with the largest density change. The temperature rise of the gap water and the moderator water is relatively small.  The largest density change occurs in the fuel assemblies of the evaporator. A stability analysis not only has to take into account FA at their average operating point but also FA with enhanced exit enthalpy as estimated by the hot channel factor analysis. In this work, a fuel assembly at the operating point will be denoted as "average" (e.g. average FA evaporator).  In the same way, a fuel assembly with enhanced enthalpy will be referred to as "hot" (e.g. hot FA evaporator).  A list of the relevant temperature of the three heat-up stages of HPLWR's III-pass-core is given in Table 1.1.
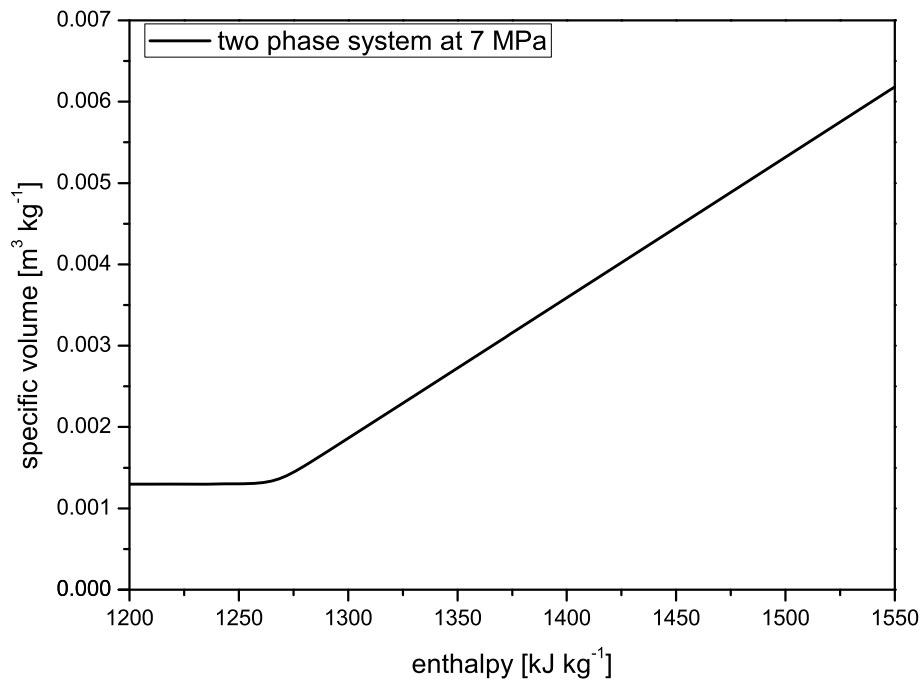
Figure 1.10: Plot of the specific volume vs. enthalpy for water at a pressure of 7 MPa.
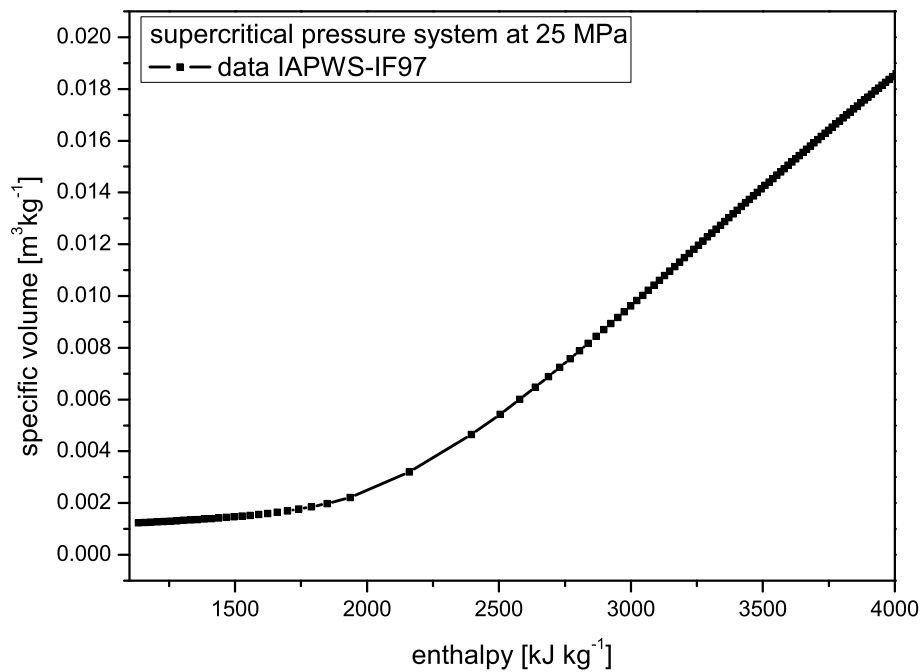


Figure 1.11: Data of specific volume vs. enthalpy for water at supercritical pressure conditions of 25 MPa. Comparison to Figure 1.10 shows remarkably similar behavior for subcritical and supercritical water.

# 1.5 Review of Flow Instabilities

It was shown above, that a flow channel at supercritical pressure heated above the pseudo-critical point has many similarities in the fluid's state behavior to boiling channels even though it is only a single phase liquid. Many types of instabilities are known in two phase flow systems, like steam generators, chemical-process reboilers, and boiling water reactors. Instabilities occur in the presence of boiling and condensation processes, but also in adiabatic flows. They can be associated to feedback mechanisms discussed below, as well as with design features, process, flow regime and controlling. A detailed review of all instability phenomena as well as control problems is beyond the scope of this chapter. Instead, it concentrates on the understanding of thermal-hydraulic instability phenomena in boiling flow which are also relevant for conditions found in a HPLWR.

In a nuclear reactor, flow instabilities are undesirable because they mean large-scale fluctuations in flow that cause large-scale pressure fluctuations. They degrade system control and performance and very often results in a departure from safe steady-state operation in the heat transfer process, which in worst case can lead to mechanical damage of the whole nuclear core. The knowledge of the stable and unstable operation conditions is a must for reactor designers.

To classify the flow instabilities we follow the proposal of Bouré et al. [9]. A first distinction can be made between static and dynamic instabilities. The first type, static instabilities, are flow phenomena whose mechanism can be explained by static/ steady-state characteristics of the thermal-hydraulic system. In particular, the appearances of these instabilities are predicted by the analysis of the steady-state pressure drop/ flow rate characteristic of the channel and its external characteristic. Note that, the word "static" does not describe the time-dependent behavior of the unstable system which is still dynamic. For the second type, the dynamic instabilities, the inertia and feedback mechanisms are essential for the process. The knowledge of the steady-state solution is not sufficient to predict the threshold of instability. Thus, the stability boundaries of dynamic instabilities are predicted on the basis of analysis of the time-dependent characteristics of the system.

Bellow, flow excursion or Ledinegg Instabilities, flow maldistribution, and pressure drop oscillations will be discussed briefly. All three instabilities are characterized by the negative resistance of the pressure drop versus flow rate relationship. In that context, resistance means the pressure drop is decreasing with raising mass flux. Ledinegg instability is induced by the interaction of a boiling flow channel with an external pump system. Flow maldistribution can occur in an array of parallel channels coupled by common plena. Pressure drop oscillations, can occur when a heated channel is connected to a pressure holder.

## 1.5.1 Ledinegg Instability

Flow excursion or Ledinegg instability is a sudden change in flow rate to different higher or lower value [42]. As the name implies, this phenomena has a non-periodic transient behavior. We consider a single boiling channel with coolant supply from a pump. The pressure drop / flow rate characteristic is shown schematically in Figure 1.12 [53]. The left dashed curve represents the case where only steam is passing through the channel.
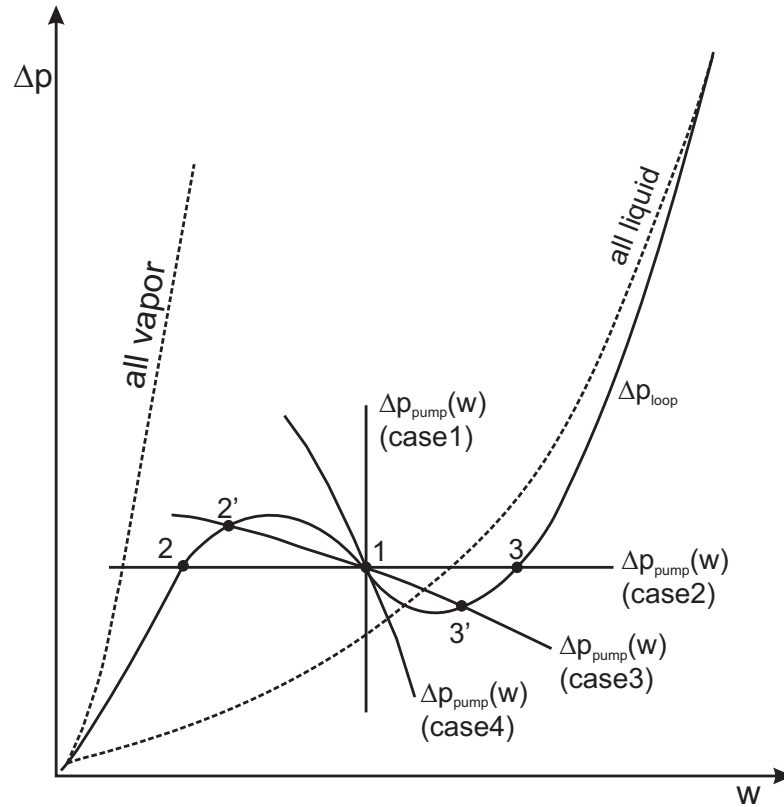
Figure 1.12: The pressure drop over an water flow channel is plotted vs. the flow rate.

Similarly, at higher flow rate, the curve where the flow in the channel is all liquid is shown. Under certain operation conditions, the pressure drop / flow rate characteristic of a boiling channel can have an s-shape. The possible operation points of the system are given by the intersection points of this s-shape with the external characteristic of the pump. Four cases are illustrated: in case 1 the pump characteristic has only one intersection with the internal characteristic (point 1). For case two, three values of flow rate are possible (point 1, 2 and 3) for the same flow rate. Assuming the nominal operation at point 1, a negative perturbation in flow rate can shift the system to new steady-state conditions at point 2 where the flow rate is significantly lower. The operation at lower flow rate can have an impact on the cooling ability of the system. Case 3 represents a realistic pressure drop curve of a pump which still has a multivalued intersection behavior. By steepening the characteristic of the pump, the appearance of Ledinegg instability can be excluded (case 4). It is stated that, the appearance of Ledinegg instability can be predicted by the analysis of steady-state characteristics.

## 1.5.2 Flow Maldistribution

Flow maldistribution is phenomenologically very closely connected to Ledinegg instability. Assuming an array of two parallel boiling channels coupled by an inlet and an outlet plenum, the channels have the internal characteristic of Figure 1.12. A constant total mass flow rate, $G_{tot}$, is imposed at the inlet plenum, and the mass flow rate for each channel is given by $G_1$ and $G_2$ ($G_{tot} = G_1 + G_2$). As the total pressure drop over the two plena

is an external boundary condition for both channels, in some region of the pressure drop / flow rate curve, the system still allows multiple mass flux values. Flow maldistribution is caused by the flow excursion or Ledinegg instability between two channels, where one of the channels provides the external characteristic for the other channel. Thus, the stability criterion for appearance of Ledinegg instability can be directly applied for flow maldistribution. When the number of parallel channels is increased, the prediction of the flow distribution can be very complicated. In a nuclear power plant, the number of parallel channels is relatively high. Therefore, to avoid such phenomena, each channel should have a negative resistance characteristic.

## 1.5.3 Pressure Drop Oscillation (PDO)

The pressure drop oscillation is a dynamic instability where a flow excursion initiates an interaction between a flow channel and a pressure holder (Figure 1.13). It is a periodic process at very low frequency (typically 0.1 Hz). A heated flow channel connected to a compressible volume is assumed, where the inlet mass flux depends on the difference of pressure between the flow channel and the compressible volume. The flow channel should have a negative resistance characteristic like in Figure 1.14 [35]. Assuming that the volume of the pressure holder is relatively large, a flow perturbation at the inlet of the flow channel does not affect the liquid level in the pressure holder substantially. The external characteristic in the pressure drop flow rate curve becomes almost horizontal. It may intersects the curve at three mass flux values. The point of negative resistance characteristics is unstable and flow excursion takes place. In Figure 1.14 six points are marked. Assuming that the initial state is a pressure drop and mass flux located at point A, a positive disturbance in flow rate can force the system toward point B. Point B is in the positive resistance region. As the inlet flow rate is constant, mass flow is injected from the compressible volume into the flow channel, which causes a decrease in pressure level in the pressure holder so that the additional flow rate also decreases. After a certain time the system has reached point C. A further decrease in flow rate results in another flow excursion to point D. Now the decrease in flow rate of the heated channel is compensated by an increase of the liquid volume in the pressure holder. With the accumulation of mass, the pressure in the compressible volume is rising. So does the flow rate which enters the boiling channel, moving the system toward point E. Again, flow excursion takes place from point E to point F. This process now repeats periodically. An experimental example of pressure drop oscillations is shown in Figure 1.14. The upper figure is the mass flow rate, the lower figure the pressure drop versus time. The processes E-F and C-D correspond to the flow excursion. The processes F-C and D-E are slow transitions, corresponding to the case where the fluid states approximately follow the steady-state curve. It is interesting to note that in the experimental example density wave oscillation takes place as well.

## 1.5.4 Density Wave Oscillation (DWO)

Density Wave Oscillations are the most common type of encountered flow instability in two-phase flow systems like BWR [54]. Their susceptibility for DWO increases especially for low coolant mass flow and high power operation conditions. The physical mechanism of DWOs is well understood and can be described in a rich number of equivalent ways.
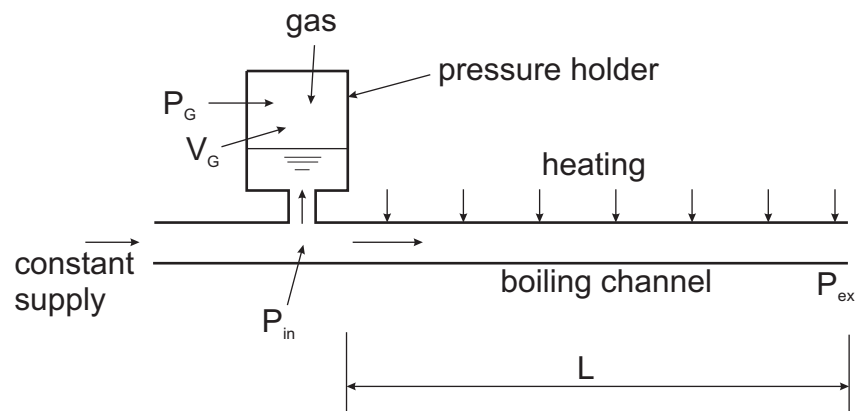
Figure 1.13: Scheme of a heated flow channel coupled with a compressible capacity and constant feed water supply.
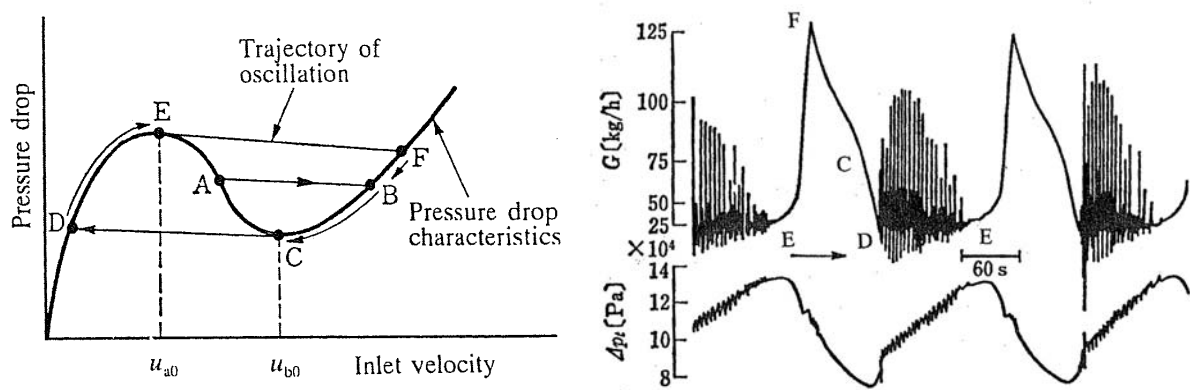


Figure 1.14: Scheme of pressure drop/ flow rate characteristic of a boiling channel with a typical s-shape. Several operation points are indicated to illustrate the path of a pressure drop oscillation (left hand side). The resulting experimental trace of a typical pressure drop oscillation is shown (right hand side). The upper curve shows the mass flux vs. time. Large amplitudes in mass flux can be seen (from E to F, and then to D). From D to E typical relaxation oscillations are observed. This corresponds to the pressure trace in time (bottom of the plot). The signal is oscillating with a rather low frequency.

Various analogies for heated channels with water at subcritical pressure passing the boiling boundary and water at supercritical pressure condition passing the pseudo-critical point can be found. In particular, the density is changing from high density of cold fluid to low density for hot fluid in both cases. For operation conditions foreseen in HPLWR, the coolant mass flow is relatively small and the power level is high. Furthermore, the coolant density change is even bigger for HPLWR than for BWR. The appearance of DWOs is expected in HPLWR and must be avoided by appropriate design parameters. Density Wave Oscillation (DWO), or enthalpy wave oscillation, is classified as a dynamic instability. The phenomenon is an oscillatory system response of a heated flow channel system due to a small fluctuation of a state variable at the channel inlet. DWO is a time-delay feedback instability caused by the finite velocity of propagation of a fluid volume traveling through the thermal-hydraulic system. Hence, the signals frequency is in the range of 0.1 - 1 Hz for the dimensions of a nuclear reactor. To disentangle the various didactic approaches for explaining the DWO mechanism, it is useful to remember that for a boiling channel in steady-state conditions, a certain axial length exists where the average fluid density in thermal equilibrium is exactly $\rho_f$ (the density of saturated liquid). This axial length can be referred to as the boiling boundary separating the low density and the high density region of the flow channel. It is obvious that the various operational parameters (e.g. channel length, hydraulic diameter, power distribution, pressure drop, orifices, etc.) have significant impact on the position of the boiling boundary. For DWO it was found that the ratio of pressure loss in the high density region - so-called in-phase pressure loss - to the pressure loss in the low density region - so-called out-of-phase pressure loss - is sensitively determining the onset of instability. The oscillatory behavior of the boiling boundary is often referred to as the deeper reason of DWO. This explanation is somehow misleading since on one hand DWO can be even observed in experiments with adiabatic flow [40], and on the other hand the boiling boundary does not exist for DWO at supercritical flow.

The DWO mechanism can be explained very clearly referring to Figure 1.16, which is composed of three parts. In the bottom part of this diagram an oscillatory perturbation in inlet flow entering a heated channel vs. time is plotted. An entering fluid volume will travel with the fluid velocity through the channel. Since the inlet flow has sinusoidal behavior, the local pressure drop will also have a sinusoidal behavior. The local pressure drop vs. time of the channel is illustrated for five axial lengths in the center part of Figure 1.16. Since the fluid is heated, the maximum amplitude of the oscillation increases with increasing axial lengths. The fluid propagates with finite speed throughout the heated channel. Thus, the very first peak of the oscillation has a time delay compared to higher axial positions. If the total pressure loss of the flow channel has to be determined, the local pressure losses have to be integrated, resulting in a sinusoidal signal (upper part of Figure 1.16). Now, if inlet flow and total pressure loss are just in the particular phase conditions that an increase in inlet flow coincides with a decrease of total pressure drop (conditions shown), the oscillation is self-sustained - a so-called unstable operation point is achieved. The right hand side of Figure 1.15 schematically shows the unstable response of a heated channel in terms of a state variable vs. time. The channel is disturbed at the time $t_0 = 0$. It can be seen that the channel deviates from the steady-state by a sinusoidal and in maximum amplitude exponentially growing signal. Furthermore, if a sensitive parameter (e.g. the heating) is reduced, the system becomes stable and a small inlet perturbation is damped with sinus-like oscillations of

exponentially decreasing maximum amplitude (e.g., left hand side of Figure 1.15). A flow channel is just at the threshold of instability, the so-called neutral stability boundary, if the deviation of steady-state are infinitesimatly small and the value of any state variable behaves sinus-like in time but neither increases nor decreases in maximum amplitude. DWOs of BWRs are devided into three types [51]. The first one is the single channel DWO or parallel channel DWO. Its main feature is that only a single fuel assembly or a small fraction of the total amount of fuel assemblies is oscillating while the other fuel assemblies of the core remain at steady-state conditions (in detail Chapter 6). The second type is the region wide or out-of-phase instability. As the name implies, in this type of instability half of the core exhibits a 180° (out-of-phase) phase shift compared to the other half [38]. The last type of instability is the core-wide in-phase instability. Here the flow and the power in all fuel assemblies oscillate in-phase. The last two types are also referred to as reactivity instabilities since they are found if a neutronic feed-back exists (both types will be discussed in Chapter 9).

### 1.5.5 Acoustic Instability

The appearance of acoustic instabilities in a HPLWR is not analyzed in this work and must be clearly distinguished from DWO. Acoustic oscillations are pressure waves travelling at the speed of sound. They oscillate at relatively high frequency of 10 - 100 Hz for boiling channels at high subcooled conditions (Bergels et al. [6]), up to audible frequency oscillations of 1000 - 10000 Hz at supercritical pressure conditions (Bishop et al. 1964). The period is related to the time required for a pressure wave to travel through the flow channel. A rough estimation for the frequency of acoustic waves can be made employing the speed of sound for water at 25 MPa computed from the water steam table for the given temperature range of HPLWR and the given fuel assembly length. For HPLWR the acoustic instability should be in the frequency range around 150 - 300 Hz. In summary it can be stated that both phenomena, density wave oscillation and acoustic oscillation, involve the propagation of a disturbance through the thermal-hydraulic system. In a flow channel a disturbance can be transported by two kinds of waves: pressure or acoustics waves. In a real system both kinds of waves exist and interact. Their velocities differ by one or two orders of magnitude. Thus, the two kinds of dynamic instabilities can be distinguished by their frequencies.

## 1.6 Literature Review on Supercritical Pressure Stability Analysis

For boiling channels flow instabilities have been a research objective since decades resulting in a rich amount of publications which provide a good insight into the basic phenomena and modeling techniques. However, the literature on stability analyses of flow at supercritical pressure is rather limited. Nevertheless, since there are strong analogies for stability phenomenas in both subcritical and supercritical systems, the following brief literature review provides first a list of works with general views on two-phase-flow stability research and second gives an overview of recent supercritical pressure stability analyses.

Table 1.2: Classification of flow instabilities in boiling channel

| Category | Pattern | Mechanism | Characteristics |
|---|---|---|---|
| Negative resistance instability | Flow excursion or Ledinegg instability | Negative damping in first order system | Transitional |
| | Flow maldistribution | | Appears in parallel channel system |
| | Pressure drop oscillation | Dynamic interaction between flow excursion and compressible capacity | Relaxation oscillation with large and long period |
| Time-delayed feedback instability | Density wave oscillation | Propagation delay of enthalpy wave | Oscillation period comparable with residence time of fluid in channel |

Boure et al. [9] reviewed two-phase flow instabilities in 1973. The various types of instabilities are classified. The methods used in the field of stability analysis are discussed in terms of their applicability and accuracy.

One of the comprehensive books on thermal-hydraulics of boiling water nuclear reactors was edited by Lahey and Moody [53]. It provides a summary of the analysis methods for static and dynamic instability phenomena. Furthermore, Lahey published a lecture on modern development in multiphase flow and heat transfer, which gives a detailed view of engineering applications of fractal and chaos theory [40].

March-Leuba et al. [38] released a state of the art review on coupled thermal-hydraulic/neutronic instabilities in boiling water nuclear reactors in 1993. In the paper, different types of observed density wave oscillations are discussed with respect to their sensitivity to various physical parameters. Furthermore, customary computer codes are reviewed. Numerical simulations of instability events are presented which occurred in the nuclear power plant of Confrentes (Spain).

Yadigaroglu provided a lecture of two-phase flow instabilities [75]. The topics presented are: instabilities of gas-liquid interfaces, instability mechanisms in two-phase flow and the stability of boiling water reactors. The second part covers the phenomena of Ledinegg instability, flow maldistribution, pressure drop oscillations and density wave oscillations. Non-linear effects like limit cycle, bifurcation and chaotic behavior of DWO are discussed. In the book Steam Power Engineering by Ishigai, Mamuro Ozawa provides an overview on flow instability problems in steam-generating tubes [35]. This overview includes both, static and dynamic instability types. For almost all presented phenomena, experimental data are shown and compared to theoretical models.

One of the earliest works on stability analysis of thermal-hydraulic systems at super-critical pressure conditions was done by Zuber in 1966 [82]. In complete analogy to the

modeling approach for a boiling channel, Zuber assumed an approximated state equation with two regions. In terms of specific volume vs. enthalpy, the first region had constant specific volume. The second region had a linear slope in the specific volume. With the foundation of the GEN-IV international forum the interest in supercritical water stability research increased.

Suhwan et al. did a coupled thermal-hydraulic/ neutronic stability analysis in the frequency domain for the American design concept of the supercritical pressure light-water cooled reactor (SCWR) using the point-kinetic model in 2001 [62]. Linear stability of two reactor options where investigated: the thermal neutron spectrum option and the fast neutron spectrum option. The stability of the nominal operation point was analyzed by evaluating the decay ratio. It was shown that the US design satisfies the stability criteria with a reasonable orifice loss coefficient (6.8) at the nominal operation point. Furthermore, the thermal-stability sensitively depends on the mass flow rate and the coupled thermal-nuclear stability sensitively depends to the coolant density coefficient.

Yi et al. analyzed the stability boundary of a high-temperature supercritical-pressure light water reactor (SCWR-H) in 2003 [64]. A one-dimensional single channel and single phase model was coupled to a point-kinetic approximation. The effect of the moderator box was taken into account. The decay ratio was calculated applying the frequency domain method. The Japanese design of SCWR-H was considered to be stable. In a further paper results on thermal and stability considerations during sliding pressure startup were published [63]. A similar approach for the US-design was made by Yang et al. in 2003 [76] and 2005 [77]. It was found that a core-wide in-phase oscillation decays quickly at operation conditions. The decay ratio of the hot channel for a coupled thermal-hydraulic/ nuclear stability calculations was below the stability margins imposed for BWR.

Zhao et al. analyzed the onset of single channel stability for the U.S. reference design in 2004 [79], [78] and 2005 [80]. The supercritical flow has been simulated using an approximated state equation, in detail, a three region model. This model consists of a region with "heavy fluid" with constant density, a region of "heavy-light fluid" mixture and finally a light fluid region described as an ideal gas. Stability maps were constructed in terms of new non-dimensional groups. Unfortunately, these were derived from the used approximated state equation. Furthermore, U.S. design SCWR stability during sliding pressure start up was analyzed. In a later work Zhao's three-region model was coupled with a point-kinetic neutronic approximation [81]. The resulting data for a core-wide out-of-phase oscillation were compared to typical BWR data. It was found that the out-of-phase oscillation of SCWR was dominated by the thermal-hydraulic model.

Chatergoorgoon did an analytic study of supercritical flow stability in two parallel channels in 2006 [11]. He developed a stability boundary criterion using an idealized point heat source. Further, he pointed out that the accuracy of the state equation is important for a realistic prediction of the stability boundary.

Ambrosini et al. developed new dimensional parameters for heated channels with supercritical fluids [2]. The non-dimensional groups presented in his paper were developed independent to the dimensional parameters which are derived in this thesis [46]. Both were presented on ICONE-14 in 2006, and the differences are discussed by Ortega et al. in detail in [49] and in Chapter 3. Furthermore, the similarities of stability phenomena at supercritical pressure conditions with the phenomena of boiling flow were pointed out by Ambrosini et al. [1].

Ortega et al. performed an analysis of non-linear instability phenomena in the time

domain, and evaluated the supercritical bifurcation branches. The effect of the chosen reference temperature in the characteristic dimensionless groups and the effect of an approximated state equation were investigated by Ortega et al. [48]. Furthermore, Ortega et al. performed an analysis for an array of coupled parallel flow channels under supercritical pressure conditions [47]. In 2008, Ortega et al. published the DWO stability limits of a typical fuel assembly cluster of the HPLWR evaporator heat-up stage [50]. Recently the density wave oscillation stability limits for a heated channel at supercritical pressure were calculated with CFD models (Sharabi et al. [58] ). The results were compared to the obtained stability limits by a one-dimensional calculation. In detail, the used standard $k - \epsilon$ model with wall function and the used low-Reynolds number model were able to predict the onset of stability at the same operation parameters as the one-dimensional approach. This fact confirms the applicability of the one-dimensional stability analysis.

## 1.7  Research Objective

Nuclear engineers assure stable operation of nuclear facilities based on the experience originating from numerous stability experiments and computer code simulations. This thesis presents theoretical considerations on stability phenomena of supercritical water typical for nuclear reactor conditions. A thermal-hydraulic and coupled neutronic/ thermal-hydraulic analysis to various types of flow instabilities is performed for the HPLWR. Compared to deployed BWRs or proposed alternative light water reactors concepts with supercritical pressure conditions (e.g. [71], [16], [45], [10]), the HPLWR provides many new design features which have a strong impact on stability. This thesis represents the first work on stability analysis of the HPLWR three-pass-core concept. The critical core components are identified with respect to relevant flow instability types. Based on the results of the analyses design parameters are proposed. In particular, a set of customized inlet orifices is designed for the coolant channels to assure a stable operation of HPLWR.

The one-dimensional modeling approach successfully employed for the prediction of stability limits in two-phase systems is extended to fuel assemblies in a nuclear reactor at supercritical pressure conditions. The mathematical model which captures the basic phenomena is non-dimensionalized to rigorously derive characteristic non-dimensional groups of the thermal-hydraulic system.
The equations are implemented in a computer package based on COMSOL [14]. COMSOL provides a modern Finite Element Method (FEM) environment for modeling and solving Partial Differential Equations (PDEs). The PDEs can be solved either interactively employing the graphical user interface of COMSOL or in batch with a classical MATLAB interface [43]. All MATLAB library functions can be accessed providing a maximum variety in numerical handling of equations and data structures. Special merit results from formulating the equation system in the weak formulation application mode. In COMSOL, the same application mode can be employed to various types of analysis, including: steady-state linear and non-linear analysis, time-dependent analysis and eigenfrequency analysis. The prediction of the stability limits can be investigated by two independent analysis methods, in the time-domain and frequency-domain. For solving eigenvalue problems the Arnoldi-algorithm is used [3]. By this choice, for the first time

in the field of nuclear stability analysis, large eigenvalue calculations can be realized on a single CPU at reasonable computational cost. In previous works the nodal discretization and the order of shape functions were rather low. In some cases even calculations with approximated state equations were performed. The numerical approach realized in this thesis represents a more flexible and high accuracy software package for investigations of supercritical stability phenomena.

The obtained results of thermal-hydraulic and coupled neutronic/ thermal-hydraulic analyses will not only determine design parameters for HPLWR, but also define stable and unstable operation regions for the HPLWR. These regions are illustrated in stability maps which are spanned by the derived non-dimensional groups. The results of this thesis are of general interest for all light water reactor concepts with supercritical pressure conditions like the PWR-SC [71], the US-SCWR [45] and pressure tube reactor concepts like the CANDU-SC [16].

# 1.8  Outline of the Thesis

Compared to deployed nuclear power reactors the HPLWR has some extraordinary design features. The relevant parameters for stability analysis are presented in Chapter 1. Furthermore, a review of the relevant instability phenomena has been given.

In Chapter 2, the mathematical model is outlined, which describes the coolant flow in the fuel assemblies of the core. This model consists of one-dimensional conservation equations and a state equation representing the physical features of water at supercritical pressure conditions. The given coupled equation system has a highly non-linear structure.

In Chapter 3 the equation system is non-dimensionalized. As a result, new non-dimensional groups for heated flow channels at supercritical pressure conditions are obtained. The new rigorously derived parameters are compared to those of boiling flow in two-phase systems. A discussion on previously proposed non-dimensional parameters by other authors is also included.

For the various numerical analyses, a computer code is developed by the author based on the COMSOL platform. Chapter 4 gives a detailed description of the numerical implementation of the thermal-hydraulic model. Futhermore, some benchmarks for the solver routines are presented.

In Chapter 5, a steady-state analysis of flow channels at HPLWR conditions is presented. Chapter 6 describes single channel density wave oscillations. A frequency domain method of linear stability analysis is applied to the HPLWR design. The neutral stability boundary is defined in stability maps spanned by the previous derived non-dimensional groups. The dependence of the results on discretization is shown. Furthermore, a simplified analytic stability criterion is presented. Results of a sensitivity study on design and operation parameters are presented and listed in a table. The effects of an approximated state equation and various axial power profiles are discussed.

A non-linear analysis is presented in Chapter 7. In detail, the full non-linear equation system is solved in the time-domain yielding limit cycles. A supercritical bifurcation diagram is compiled.

In Chapter 8, the modeling approach used for the single channel DWO is extended to an array of parallel flow channels coupled by common inlet and exit plena. Various arrays of parallel flow channels are discussed in frequency and time-domain. The most relevant

case analyzes the special stability characteristic of the fuel assembly cluster.

A coupled thermal-hydraulic/ neutronic analysis is discussed in Chapter 9. The thermal-hydraulic model is extended by a neutronic model and a fuel rod model. The region-wide out-of-phase DWO and a local in-phase DWO are investigated.

The results of the various analyses have consequences for the HPLWR design parameters. The orifices of the evaporator are dimensioned in Chapter 10.

In the last chapter, the conclusions of all analyses are summarized and recommendations are provided for future works.
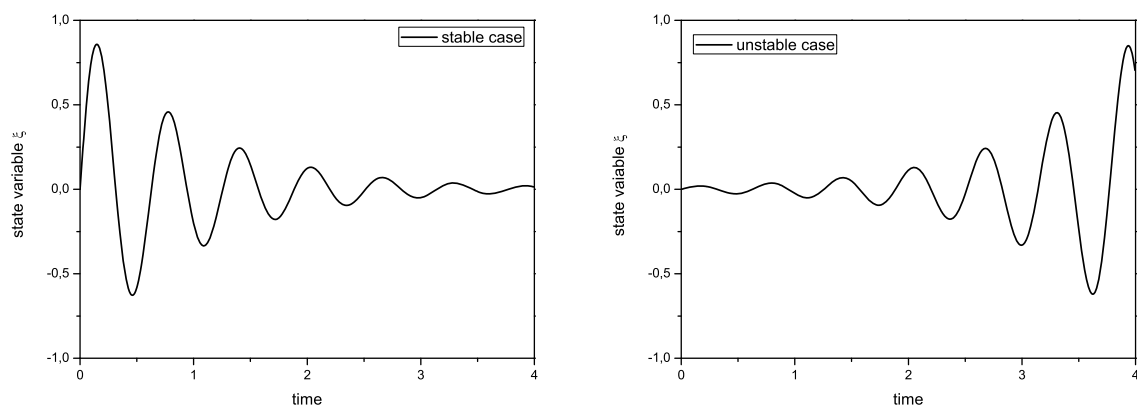
Figure 1.15: Schema of density wave oscillation for the stable (left hand side) and unstable case (right hand side). The system response is illustrated in terms of perturbation of a state variable $\xi$ out of steady-state conditions vs. time.
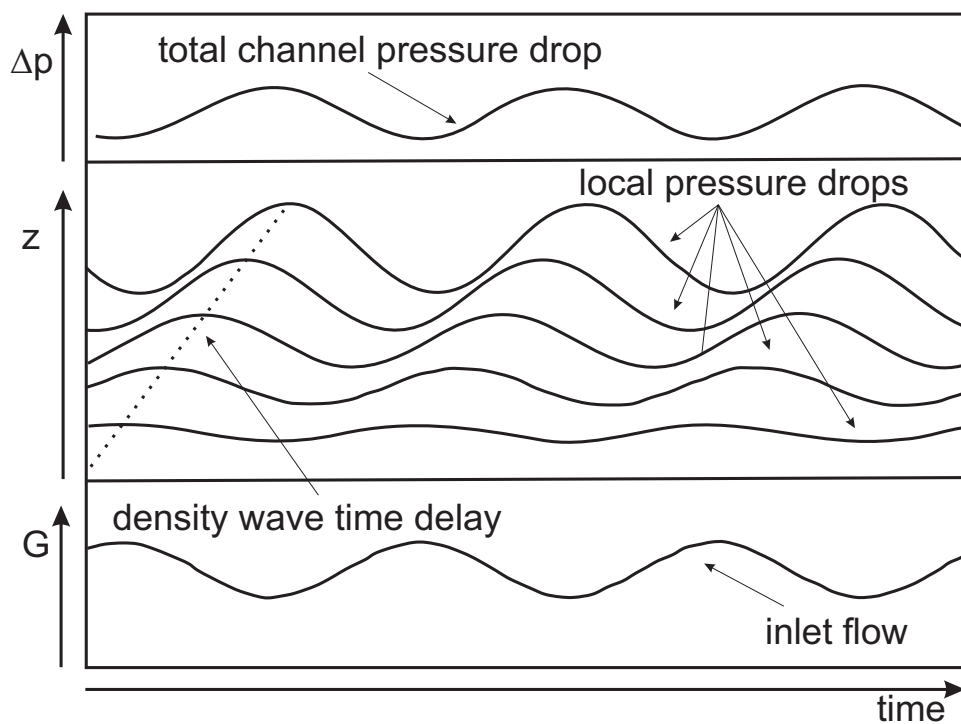


Figure 1.16: Illustration of the density wave oscillation mechanism.

# 2 Equation System

The flow of coolant in a one-dimensional channel is governed by the conservation equations for mass, momentum, and energy. The equation of state relates pressure, density, and temperature and is needed to close the system of equations. The state equation is in algebraic form. Any fluid state is determined by defining three independent variables and one state variable. For the various thermal-hydraulic analyses, the variables will be chosen as: pressure $p$, enthalpy $h$, mass flux $G$ and density $\rho$. Before introducing the mathematical formulation in detail, it is useful to characterize the coolant flow of HPLWR fuel assemblies in terms of thermal-hydraulic characteristic numbers.

## 2.1 Characterization of Coolant Flow

In nature there are many types of hydro-dynamic instability phenomena [28]. This thesis focuses on flow instabilities in the sense of large scale fluctuations in coolant flow. Thus, other typical hydro-dynamic instabilities like flow fluctuation in the slug flow regime or flow pattern transition are not investigated in this thesis, although these phenomena may provide triggers for flow instability. The instabilities of interest here are macroscopic phenomena, which are not localized in a rather small area. The one-dimensional modeling approach often used for BWR stability analysis is extended to supercritical pressure operation conditions. The validity of a one-dimensional approach is not only strengthened by successful prediction of stability limits in deployed BWRs during the last four decades, but also by the comparison to numerically computed onsets of stability from one-dimensional and three-dimensional-CFD calculations for simplified geometries at supercritical pressure conditions [58]. An heuristic reason for the one-dimensional approach is the axial height of nearly 5 m for a fuel assembly with a hydraulic diameter of only $D_H = 5.336$ mm (i.e. a ratio of length scales of $\approx 10^3$).

Similar to the Favre-average [26], density weighted cross-sectional averaged quantities are introduced as

$$\tilde{f} = \frac{\overline{\rho f}}{\overline{\rho}} \quad , \tag{2.1}$$

where

$$\overline{\rho f} = \frac{1}{A_{x-s}} \int\int_{A_{x-s}} (\rho f) \, \mathrm{d}A_{x-s} \quad , \tag{2.2}$$

and $A_{x-s}$ is the cross-sectional flow area of a fuel assembly. The case of $f = 1$ the density $\rho$ yields

$$\overline{\rho} = \frac{1}{A_{x-s}} \int\int_{A_{x-s}} \rho \, \mathrm{d}A_{x-s} \quad . \tag{2.3}$$

The Mach number is defined as the density weighted cross-sectional averaged velocity, $\tilde{u}$,

of the coolant in the fuel assembly, divided by the speed of sound, $u_s$, of water at 25 MPa [27]:

$$\text{M} = \frac{\tilde{u}}{u_s} \quad . \tag{2.4}$$

The projected mass flow and the temperature rise of the coolant is given for the HPLWR core, so $\tilde{u}$ can be determined. Furthermore, the speed of sound for water can be obtained using the water steam table (IAWPS-IF97 [72]). For the projected temperatures Mach numbers in the range of 0.001 - 0.03 are obtained. Hence M $\ll$ 1 and a low Mach number approximation can be applied.

The local Reynolds number Re describes the ratio of inertial forces to viscous forces:

$$\text{Re} = \frac{\text{inertial forces}}{\text{viscous forces}} = \frac{\tilde{u}D_H}{\overline{\nu}} \tag{2.5}$$

with the hydraulic diameter $D_H$ of a typical fuel assembly and the cross-sectional averaged kinematic viscosity of the fluid, $\overline{\nu}$. $D_H$ is given by

$$D_H = \frac{4A_{x-s}}{P_f} \quad , \tag{2.6}$$

where $P_f$ is the wetted perimeter. The Reynolds number for an equivalent one-dimensional flow channel representing the conditions given in a HPLWR fuel assembly are plotted in Figure 2.1. The Reynolds numbers vary in a wide range from the fuel assembly inlet to the outlet while the most drastic variation can be observed around the pseudo-critical point. Obviously, the whole flow is turbulent.

The dimensionless number comparing inertial and gravitational forces is the Froude number:

$$\text{Fr} = \frac{\text{inertial forces}}{\text{gravitational forces}} = \frac{\tilde{u}_{\text{in}}^2}{gL} \tag{2.7}$$

where $g$ is the acceleration due to gravity for a vertical flow channel, $L$ is the length of the flow channel and $\tilde{u}_{\text{in}}$ is the inlet velocity of the fluid. The Froude number is approximately around 0.1.

The local Prandtl number, Pr, is the ratio of momentum and thermal diffusivity [26]:

$$\text{Pr} = \frac{\text{momentum diffusion rate}}{\text{thermal diffusion rate}} = \frac{\overline{c}_{p,\text{fluid}} \, \overline{\mu}}{\overline{\lambda}_{\text{th}}} \quad , \tag{2.8}$$

where $\overline{c}_{p,\text{fluid}}$ is the heat capacity of water at 25 MPa (see Figure 1.5), $\overline{\mu}$ is the dynamic viscosity of the fluid and $\overline{\lambda}_{\text{th}}$ is the thermal conductivity. The distribution of the Prandtl number is plotted in Figure 2.1. As for the Reynolds number, the most drastic variation occurs while the supercritical fluid is heated beyond the pseudo-critical point resulting in a peak of the Prandtl number.

A one-dimensional (global) modeling approach will be applied. Local profiles of fluid temperature, static pressure, velocity and shear stress are homogenized across the cross-section of one fuel assembly. A fuel assembly is treated as one flow channel [53].
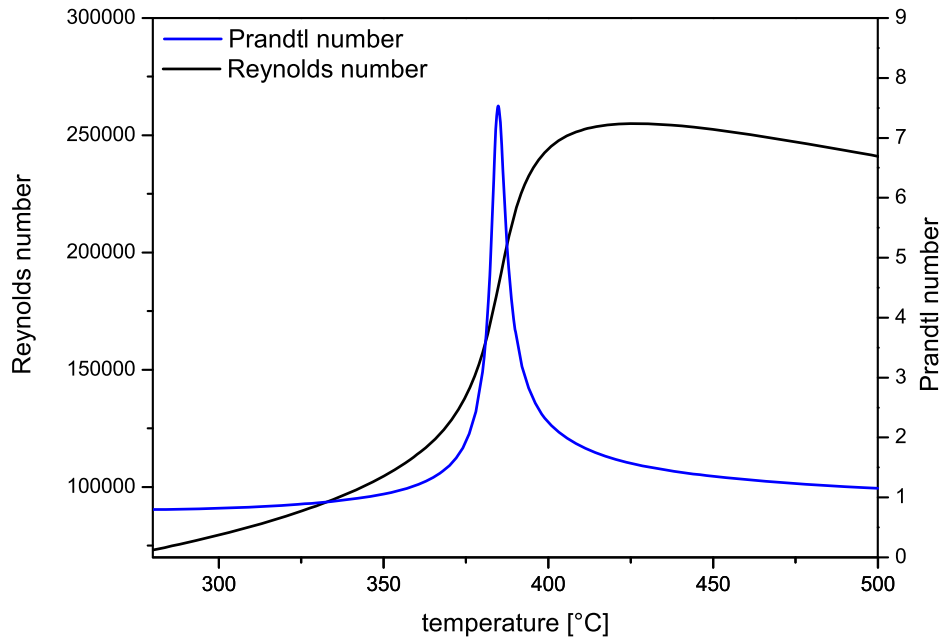
Figure 2.1: Reynolds number (blue) and Prandtl number (black) vs. temperature.

## 2.2 State Equation

Since the Mach number is small (M << 1), a low-Mach-number-approximation can be applied. Hence, the physical properties of the fluid are only dependent on temperature. The validity of this assumption can be illustrated by the most sensitive parameter, the heat capacity $c_p$. For nominal operating pressure of 25 MPa, fluid properties are weakly dependent on the local pressure (Figure 2.2). The state equation is given by

$$\rho = \rho(h)_p \quad . \tag{2.9}$$

In principle the state equation can be expressed in terms of temperature or in terms of enthalpy. The density vs. the temperature range of interest for the HPLWR is illustrated in Figure 1.8. The formulation chosen for the numerical implementation is plotted in Figure 2.3. Here, the density is given by an algebraic equation dependent on the enthalpy. The advantage of this formulation is the smooth behavior passing the pseudo-critical point, which provides high numerical stability and fast convergence.

## 2.3 Mass Conservation Equation

The basic conservation of mass can be written for a control volume as [53]

$$
\begin{bmatrix} \text{rate of} \\ \text{creation of} \\ \text{mass} \end{bmatrix}
\triangleq
\begin{bmatrix} \text{mass} \\ \text{outflow} \\ \text{rate} \end{bmatrix}
-
\begin{bmatrix} \text{mass} \\ \text{inflow} \\ \text{rate} \end{bmatrix}
+
\begin{bmatrix} \text{mass} \\ \text{storage} \\ \text{rate} \end{bmatrix}
= 0 \quad . \tag{2.10}
$$
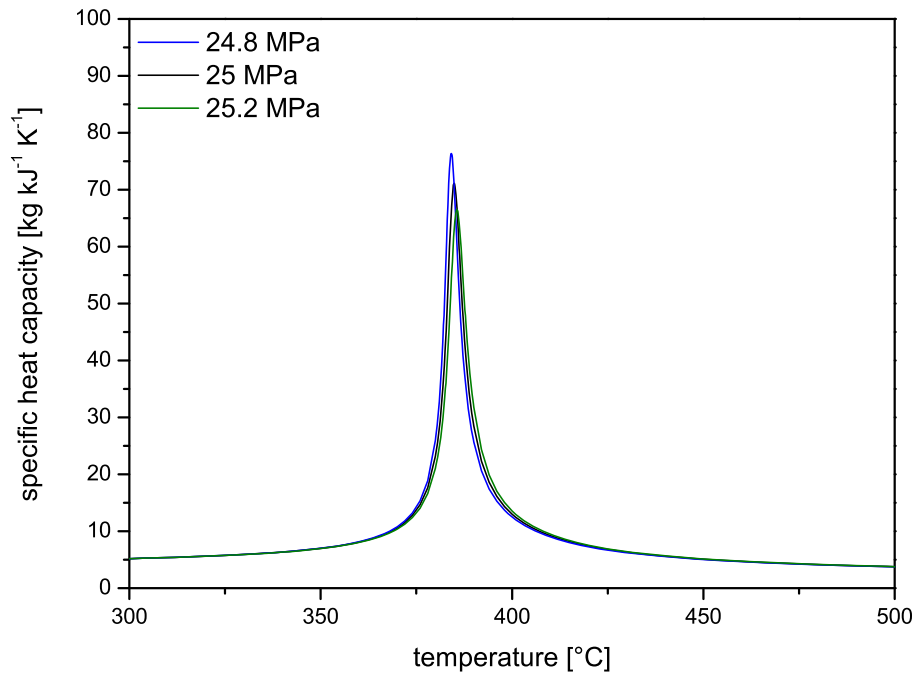
Figure 2.2: Specific heat capacity vs. temperature around the pseudo-critical point for different pressure levels.
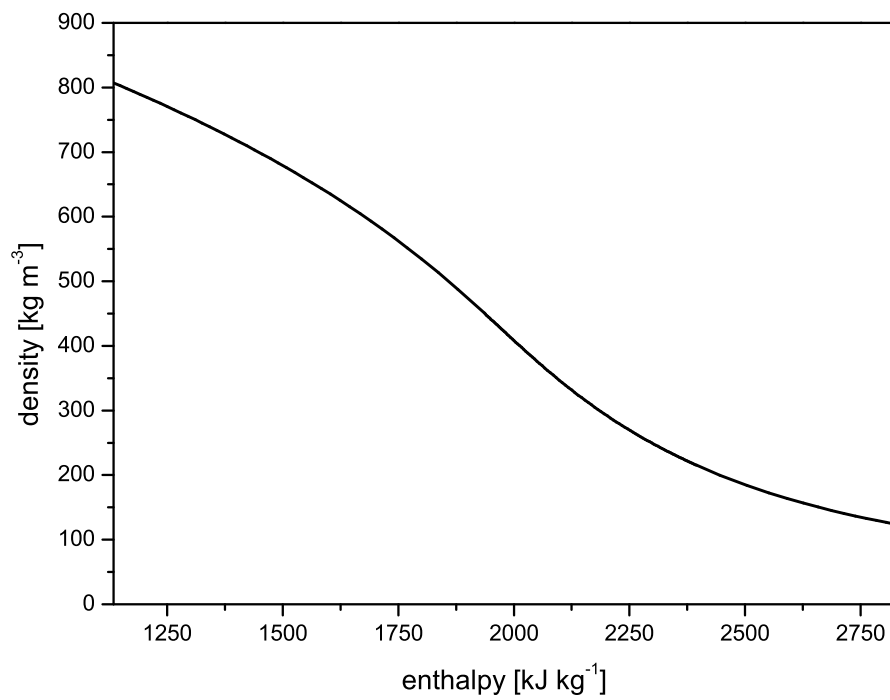


Figure 2.3: Density vs. enthalpy at 25 MPa.

This implies the conservation equation of mass given by [26]

$$\frac{\partial \rho}{\partial t} + \frac{\partial (\rho u)}{\partial x} + \frac{\partial (\rho v)}{\partial y} + \frac{\partial (\rho w)}{\partial z} = 0 \ . \tag{2.11}$$

where $\rho$ is the density and $u$, $v$, $w$ are the velocities x-, y-, and z-direction, respectively. Each velocity component can be expressed as the sum of the cross-sectional averaged quantity $\tilde{f}(x,t)$ or $\overline{f}(x,t)$ (Eq(2.2)) and its local deviation $f''(x,y,z,t)$ or $f'(x,y,z,t)$, respectively. In particular, we have

$$\begin{aligned} \rho &= \overline{\rho} + \rho' \ , \quad p = \overline{p} + p' \ , \\ u &= \tilde{u} + u'' \ , \quad v = \tilde{v} + v'' \ , \quad w = \tilde{w} + w'' \ . \end{aligned} \tag{2.12}$$

As density $\rho$ and pressure $p$ are simple cross-sectional weighted quantities their local deviation are indicated with a single prime. For two quantities $f$ and $l$ the following rules apply

$$\overline{\frac{\partial f}{\partial s}} = \frac{\partial \overline{f}}{\partial s} \ , \quad \overline{f+l} = \overline{f} + \overline{l} \ , \quad \overline{f'} = 0 \ , \quad \overline{\rho f''} = 0 \ . \tag{2.13}$$

The cross-sectional averaged mass conservation equation is

$$\frac{1}{A_{x-s}} \int \int_{A_{x-s}} \left( \frac{\partial \rho}{\partial t} + \frac{\partial (\rho u)}{\partial x} + \frac{\partial (\rho v)}{\partial y} + \frac{\partial (\rho w)}{\partial z} \right) \mathrm{d}A_{x-s} = 0 \ , \tag{2.14}$$

in the more compact notation

$$\overline{\frac{\partial \rho}{\partial t} + \frac{\partial (\rho u)}{\partial x} + \frac{\partial (\rho v)}{\partial y} + \frac{\partial (\rho w)}{\partial z}} = 0 \ , \tag{2.15}$$

applying Eqs(2.12) and Eqs(2.13) yields

$$\frac{\partial \overline{\rho}}{\partial t} + \frac{\partial \overline{[\rho(\tilde{u}_i + u_i'')]}}{\partial x_i} = 0 \ , \tag{2.16}$$

where the index $i = 1, 2, 3$ for spatial coordinates. Note that

$$\frac{\partial \overline{[\rho(\tilde{u}_i + u_i'')]}}{\partial x_i} = \frac{\partial \overline{(\rho \tilde{u}_i)}}{\partial x_i} + \frac{\partial \overline{(\rho u_i'')}}{\partial x_i} = \frac{\partial (\overline{\rho} \tilde{u}_i)}{\partial x_i} \ . \tag{2.17}$$

For the y-direction and z-direction we have

$$\frac{\partial (\overline{\rho} \tilde{v})}{\partial y} = \frac{\partial}{\partial y} \underbrace{\frac{1}{A_{x-s}} \int \int_{A_{x-s}} (\rho v) \mathrm{d}A_{x-s}}_{f_1(x)} \equiv 0 \ , \tag{2.18}$$

$$\frac{\partial (\overline{\rho} \tilde{w})}{\partial z} = \frac{\partial}{\partial z} \underbrace{\frac{1}{A_{x-s}} \int \int_{A_{x-s}} (\rho w) \mathrm{d}A_{x-s}}_{f_2(x)} \equiv 0 \ . \tag{2.19}$$

Employing Eq(2.18) and Eq(2.19), the one-dimensional mass conservation equation is given by

$$\frac{\partial \overline{\rho}}{\partial t} + \frac{\partial (\overline{\rho}\tilde{u})}{\partial x} = 0 \quad . \tag{2.20}$$

Next, the cross-sectional averaged mass flux $\overline{G}$ is defined as

$$\overline{G} = \overline{\rho u} = \overline{\rho}\tilde{u} \quad . \tag{2.21}$$

Thus, we have

$$\frac{\partial \overline{\rho}}{\partial t} + \frac{\partial \overline{G}}{\partial x} = 0 \quad , \tag{2.22}$$

combining the transient term in Eq(2.22) with the state equation leads to

$$\frac{\partial \overline{\rho}}{\partial t} = \frac{\partial \overline{\rho}}{\partial \overline{h}}\frac{\partial \overline{h}}{\partial t} = \frac{\partial (1/\overline{v})}{\partial \overline{h}}\frac{\partial \overline{h}}{\partial t} \quad , \tag{2.23}$$

where $\overline{v}$ is the cross-sectional averaged specific volume defined as the reciprocal cross-sectional averaged density

$$\overline{v} = \frac{1}{\overline{\rho}} \quad , \tag{2.24}$$

thus,

$$\frac{\partial \overline{h}}{\partial t} = \overline{v}^2 \frac{\partial \overline{G}}{\partial x} \left(\frac{\partial \overline{v}}{\partial \overline{h}}\right)^{-1} \quad . \tag{2.25}$$

As all flow and state variables are treated as cross-sectional averaged quantities, we drop the overbar and overtilde for convenience. Therefore, Eq(2.25) is presented as:

$$\frac{\partial h}{\partial t} = v^2 \frac{\partial G}{\partial x} \left(\frac{\partial v}{\partial h}\right)^{-1} \quad . \tag{2.26}$$

## 2.4 Momentum Conservation Equation

Conservation of momentum can be denoted as [66]

$$\begin{bmatrix} \text{rate of} \\ \text{creation of} \\ \text{momentum} \end{bmatrix} \triangleq \begin{bmatrix} \text{momentum} \\ \text{outflow} \\ \text{rate} \end{bmatrix} - \begin{bmatrix} \text{momentum} \\ \text{inflow} \\ \text{rate} \end{bmatrix} + \begin{bmatrix} \text{momentum} \\ \text{storage} \\ \text{rate} \end{bmatrix} \tag{2.27}$$

$$= \begin{bmatrix} \text{sum of forces} \\ \text{on the} \\ \text{control volume} \end{bmatrix}$$

applying the same approach used for the mass conservation equation for the x-direction results in [26]

$$\overline{\frac{\partial(\rho u)}{\partial t} + \frac{\partial(\rho u^2)}{\partial x} + \frac{\partial(\rho uv)}{\partial y} + \frac{\partial(\rho uw)}{\partial z}} = \overline{F_x - \frac{\partial p}{\partial x} + \frac{\partial \sigma_{xx}}{\partial x} + \frac{\partial \tau_{yx}}{\partial y} + \frac{\partial \tau_{zx}}{\partial z}} \quad , \qquad (2.28)$$

where

$$\sigma_{xx} = \mu \left( 2\frac{\partial u}{\partial x} - \frac{2}{3}(\nabla \cdot \mathbf{v}) \right) \quad , \quad \tau_{yx} = \mu \left( \frac{\partial v}{\partial x} + \frac{\partial u}{\partial y} \right) \quad , \quad \tau_{zx} = \mu \left( \frac{\partial w}{\partial x} + \frac{\partial u}{\partial z} \right) \quad . \qquad (2.29)$$

With Eqs(2.13) and applying similar considerations as in Eq(2.18) and Eq(2.19) to the third and fourth term on the left hand side of Eq(2.28). In particular

$$\frac{\partial(\overline{\rho uv})}{\partial x_\alpha} = \frac{\partial}{\partial x_\alpha} \underbrace{\frac{1}{A_{x-s}} \int\int_{A_{x-s}} (\rho uv) \, \mathrm{d}A_{x-s}}_{f_\alpha(x)} \equiv 0 \quad , \qquad (2.30)$$

where $\alpha = 1, 2$ denotes lateral directions. This yields

$$\frac{\partial \overline{(\rho u)}}{\partial t} + \frac{\partial \overline{(\rho u^2)}}{\partial x} = \overline{F_x} - \frac{\partial \overline{p}}{\partial x} + \frac{\partial \overline{\sigma_{xx}}}{\partial x} \quad . \qquad (2.31)$$

Employing Eqs(2.12) and Eqs(2.13) the second term on the left hand side becomes

$$\frac{\partial \overline{(\rho u^2)}}{\partial x} = \frac{\partial \overline{[\rho(\tilde{u} + u'')^2]}}{\partial x} = \frac{\partial(\overline{\rho}\tilde{u}^2)}{\partial x} + \frac{\partial \overline{(\rho u''^2)}}{\partial x} \quad . \qquad (2.32)$$

Now, $\overline{F_x}$ is

$$\overline{F_x} = -g\overline{\rho} \sin \Theta \quad . \qquad (2.33)$$

Applying Eq(2.32) and Eq(2.21) the momentum conservation equation becomes

$$\frac{\partial \overline{G}}{\partial t} + \frac{\partial(\overline{G}^2/\overline{\rho})}{\partial x} = -g\overline{\rho} \sin \Theta - \frac{\partial \overline{p}}{\partial x} + \frac{\partial \overline{\sigma_{xx}}}{\partial x} - \frac{\partial \overline{(\rho u''^2)}}{\partial x} \quad , \qquad (2.34)$$

The last four terms on the right hand side correspond to the irreversible pressure loss due to frictional effects. Applying Eq(2.24) and defining $g_{\text{eff}} = g \sin \Theta$ as the acceleration due the vertical component of gravity $g$, we have

$$\frac{\partial \overline{G}}{\partial t} + \frac{\partial(\overline{G}^2/\overline{\rho})}{\partial x} = -\overline{\rho}g_{\text{eff}} - \frac{\partial \overline{p}}{\partial x} + \frac{\partial \overline{\sigma_{xx}}}{\partial x} - \frac{\partial \overline{(\rho u''^2)}}{\partial x} \quad , \qquad (2.35)$$

Note that cross-sectional averages make consideration of lateral balances obsolete.

### 2.4.1 Frictional Pressure Loss

In single phase flow, considered here, the frictional pressure loss can be expressed in terms of the dynamic head and an empirical irreversible loss coefficient,

$$\frac{\partial \overline{\sigma_{xx}}}{\partial x} - \frac{\partial \overline{(\rho u''^2)}}{\partial x} = \frac{f}{2D_H} \frac{\overline{G}^2}{\overline{\rho}} \quad , \tag{2.36}$$

where $f$ is the Darcy-Weisbach friction factor [44] for turbulent flow. $f$ can be determined in implicit form by the Colebrook equation which was derived by combining experimental results of laminar and turbulent flow in pipes [12].

$$\frac{1}{\sqrt{f}} = -2\log\left(\frac{\varepsilon}{3.7D_H} + \frac{2.51}{\mathrm{Re}\sqrt{f}}\right) \quad , \tag{2.37}$$

with Reynolds-Number Re and the relative pipe roughness $\varepsilon/D_H$, which is the ratio of the mean height of the roughness of the steel test section to the hydraulic diameter. Later, Haaland gave an approximated explicit relation for the Darcy-Weisbach friction factor [30].

$$f = \left[-1.8\log\left(\left(\frac{\varepsilon}{3.7D_H}\right)^{1.11} + \frac{6.9}{\mathrm{Re}}\right)\right]^{-0.5} \tag{2.38}$$

Here, for the conditions in HPLWR fuel assemblies (bundle flow), an $\varepsilon/D_H = 0.00275$ is assumed [4].

### 2.4.2 Local Pressure Loss

Local pressure losses are needed to represent inlet and outlet devices like orifices. The pressure loss of an orifice is given by [70]

$$\Delta p = K\frac{1}{2}\overline{\rho}\tilde{u}^2 = K\frac{\overline{G}^2}{2\overline{\rho}} \quad , \tag{2.39}$$

where K is the geometry dependent pressure loss coefficient. The subscripts *in* and *out* denote an orifice at the inlet and exit of a fuel assembly. The momentum equation can now be expressed in Lagrangian form as

$$\frac{\partial \overline{G}}{\partial t} + \frac{\partial(\overline{G}^2/\overline{\rho})}{\partial x} = -\frac{\partial \overline{p}}{\partial x} - \overline{\rho}g_{\mathrm{eff}} - \left[K_{\mathrm{in}}\delta(x) + K_{\mathrm{out}}\delta(x-L) + \frac{f}{D_H}\right]\frac{(\overline{G}^2/\overline{\rho})}{2} \quad , \tag{2.40}$$

where $\delta(x)$ is the Dirac Delta function. Applying Eq(2.24) and dropping the overbar for convenience as above

$$\frac{\partial G}{\partial t} + \frac{\partial(G^2 v)}{\partial x} = -\frac{\partial p}{\partial x} - \frac{g_{\mathrm{eff}}}{v} - \left[K_{\mathrm{in}}\delta(x) + K_{\mathrm{out}}\delta(x-L) + \frac{f}{D_H}\right]\frac{(G^2 v)}{2} \quad . \tag{2.41}$$

## 2.5  Energy Conservation Equation

Conservation of energy is given by

$$
\begin{bmatrix} \text{rate of} \\ \text{creation of} \\ \text{energy} \end{bmatrix} \triangleq \begin{bmatrix} \text{energy} \\ \text{outflow} \\ \text{rate} \end{bmatrix} - \begin{bmatrix} \text{energy} \\ \text{inflow} \\ \text{rate} \end{bmatrix} + \begin{bmatrix} \text{energy} \\ \text{storage} \\ \text{rate} \end{bmatrix} = 0 \ . \tag{2.42}
$$

This implies [26]

$$
\rho \left( \frac{\partial h}{\partial t} + u \frac{\partial h}{\partial x} + v \frac{\partial h}{\partial y} + w \frac{\partial h}{\partial z} \right) = \frac{\partial p}{\partial t} + u \frac{\partial p}{\partial x} + v \frac{\partial p}{\partial y} + w \frac{\partial p}{\partial z} + \tag{2.43}
$$
$$
\frac{\partial}{\partial x} \left[ \lambda_{th} \frac{\partial T}{\partial x} \right] + \frac{\partial}{\partial y} \left[ \lambda_{th} \frac{\partial T}{\partial y} \right] + \frac{\partial}{\partial z} \left[ \lambda_{th} \frac{\partial T}{\partial z} \right] + \mu \Phi \ ,
$$

where the enthalpy $h$ is given by

$$
h = e + \frac{p}{\rho} \ , \tag{2.44}
$$

with the internal energy $e$, and the temperature T. $\lambda_{th}$ is the thermal heat conductivity and $\Phi$ is the dissipation function given by

$$
\Phi = 2 \left[ \left( \frac{\partial u}{\partial x} \right)^2 + \left( \frac{\partial v}{\partial y} \right)^2 + \left( \frac{\partial w}{\partial z} \right)^2 \right] + \left( \frac{\partial v}{\partial x} + \frac{\partial u}{\partial y} \right)^2 + \tag{2.45}
$$
$$
\left( \frac{\partial w}{\partial y} + \frac{\partial v}{\partial z} \right)^2 + \left( \frac{\partial u}{\partial z} + \frac{\partial w}{\partial x} \right)^2 - \frac{2}{3} \left( \frac{\partial u}{\partial x} + \frac{\partial v}{\partial y} + \frac{\partial w}{\partial z} \right)^2 \ .
$$

Similar to the approach for the momentum and mass conservation equation, the cross-sectional average results in

$$
\overline{\rho \frac{\partial h}{\partial t}} + \overline{\rho u \frac{\partial h}{\partial x}} = \frac{q'' P_H}{A_{x-s}} + \overline{\frac{\partial}{\partial x} \left[ \lambda_{th} \frac{\partial T}{\partial x} \right]} + \overline{\mu \Phi} \ , \tag{2.46}
$$

where

$$
\frac{q'' P_H}{A_{x-s}} = \overline{\frac{\partial}{\partial y} \left[ \lambda_{th} \frac{\partial T}{\partial y} \right]} + \overline{\frac{\partial}{\partial z} \left[ \lambda_{th} \frac{\partial T}{\partial z} \right]} \ . \tag{2.47}
$$

Compared to the amount of nuclear energy which is transfered into the coolant channel (through the heated perimeter $P_H$) the terms

$$
\overline{\frac{\partial p}{\partial t} + u \frac{\partial p}{\partial x} + v \frac{\partial p}{\partial y} + w \frac{\partial p}{\partial z}} \tag{2.48}
$$

are neglected in Eq(2.46). Furthermore, the thermal energy which is generated due to dissipation has no practical signification. Employing Eq(2.12) and Eq(2.13), Eq(2.46) becomes

$$
\overline{\rho} \frac{\partial \tilde{h}}{\partial t} + \overline{\rho} \tilde{u} \frac{\partial \tilde{h}}{\partial x} = \frac{q'' P_H}{A_{x-s}} + \overline{\frac{\partial}{\partial x} \left[ \lambda_{th} \frac{\partial T}{\partial x} \right]} - \overline{\rho u'' \frac{\partial h''}{\partial x}} \ . \tag{2.49}
$$

The averaged convection term on the right hand side can be viewed as additional heat transfer in x-direction. However, for the case of a coolant channel in a nuclear reactor,

this term and the axial heat conduction are generally neglected [53]. In the steady-state the energy equation is dominated by the balance of the convection term $\overline{\rho}\tilde{u}\frac{\partial \tilde{h}}{\partial x}$ and the heat transfer though the cladding of the fuel rods. Thus, applying Eq(2.21) the one-dimensional energy conservation equation results to:

$$\frac{\partial \tilde{h}}{\partial t} + \frac{\overline{G}}{\overline{\rho}}\frac{\partial \tilde{h}}{\partial x} = \frac{q'' P_H}{\overline{\rho} A_{x-s}} \quad . \tag{2.50}$$

Note that the produced nuclear energy appears directly as a source term (r.h.s. Eq(2.50)). Applying Eq(2.24) to Eq(2.50) finally results in:

$$\frac{\partial h}{\partial t} + Gv\frac{\partial h}{\partial x} = v\frac{q'' P_H}{A_{x-s}} \quad , \tag{2.51}$$

where - as above - the overbar and overtilde are droped for convenience.

Finally, the thermal-hydraulic equation system is summarized here:
Mass conservation:

$$\frac{\partial h}{\partial t} = v^2 \frac{\partial G}{\partial z}\left(\frac{\partial v}{\partial h}\right)^{-1} \quad . \tag{2.52}$$

Momentum conservation:

$$\frac{\partial G}{\partial t} + \frac{\partial (G^2 v)}{\partial z} = -\frac{\partial p}{\partial z} - \frac{g_{\text{eff}}}{v} - \left[K_{\text{in}}\delta(z) + K_{\text{out}}\delta(z - L) + \frac{f}{D_H}\right]\frac{(G^2 v)}{2} \quad . \tag{2.53}$$

Energy conservation:

$$\frac{\partial h}{\partial t} + Gv\frac{\partial h}{\partial z} = v\frac{q'' P_H}{A_{x-s}} \quad . \tag{2.54}$$

State equation:

$$\rho = \rho(h)_p \quad . \tag{2.55}$$

Note that the notation commonly used in the field of one-dimensional analysis for nuclear reactors with vertical coolant channels is now applied. The axial direction is referred to as z-direction and the corresponding velocity component is denoted as $u$.

# 3 Nondimensional Parameters

Dimensionless groups are useful to reduce the number of independent parameters and to serve as a basis for developing scaling laws [39]. Normally, complementary efforts in computer code development and in experiments using scaled models are made to define the stability characteristics of nuclear reactors. The results of numerical simulations presented this thesis are the very first investigations on HPLWR stability. Experimental data will be taken at the University of Delft once a test section is built up in the end of 2008.

For the linear stability analysis of two-phase flow, the dimensional groups were developed in the late 6o's [36]. These derivations will not be repeated here, but discussed for comparison with the non-dimensional parameters suitable for super-critical water.

## 3.1 Nondimensional Parameters for Boiling Channels

The operating state of a boiling channel is specified by the following parameters: the physical properties of the fluid, channel geometry (length, hydraulic diameter, heated perimeter, frictional characteristics, etc), system pressure level, axial heat input distribution, flow rate or channel pressure drop, and the inlet coolant temperature. For stability investigations the first three quantities and the power level are usually specified. For a given geometry with a uniform power profile, fluid properties, gravity, pressure, inlet velocity, inlet temperature and heat flux are taken into account using four dimensional groups:

- The Froude number also called reduced gravity is the ratio of the inertial to the gravitational forces:

$$\mathrm{Fr} \equiv \frac{u_{\mathrm{in}}^2}{gL_H} \quad , \tag{3.1}$$

  where $g$ is the gravitational acceleration for a vertical flow channel, $L_H$ is the heated length of the channel and $u_{\mathrm{in}}$ is the inlet velocity of the fluid.

- The Euler number also called friction number

$$\Lambda \equiv \frac{fL_H}{2D_H} \quad , \tag{3.2}$$

  with $f$ as the friction factor and $D_H$ is the hydraulic diameter of the flow channel.

- The ratio of reduced velocity involving the channel's flow rate $(GA_{x-s})$ to the power $(\bar{q}''P_HL_H)$ results in the so-called Phase-Change-Number and includes the specific volume ratio and latent heat $h_g - h_f$.

$$\mathrm{N_{PCH}} \equiv \frac{v_g - v_f}{v_f(h_g - h_f)} \frac{\bar{q}''P_HL_H}{GA_{x-s}} \quad , \tag{3.3}$$

where $v_f$, $v_g$ is the specific volume and $h_f$, $h_g$ is the enthalpy of saturated liquid and steam, respectively. $\bar{q}''$, $G$, $P_H$ and $A_{x-s}$ is the axial heat flux, the mass flux, the heated perimeter, and cross-sectional flow area, respectively.

- The Subcooling-Number which is the ratio of subcooling of the fluid at the inlet to the latent heat, weighted with the specific volume ratio.

$$\mathrm{N_{SUB}} \equiv \frac{v_g - v_f}{v_f(h_g - h_f)}\Delta h_{\mathrm{SUB}} \quad , \tag{3.4}$$

where $\Delta h_{\mathrm{SUB}}$ is the difference between the enthalpy of saturated liquid, $h_f$, and the inlet enthalpy, $h_{\mathrm{in}}$:

$$\Delta h_{\mathrm{SUB}} = h_f - h_{\mathrm{in}} \quad . \tag{3.5}$$

A two-dimensional space spanned by the Subcooling-Number versus Phase-Change-Number is the so-called stability plane. In this plane the neutral stability boundary curve separates the stable from the unstable operation conditions of a boiling channel. A typical stability map is shown in Figure 3.1. The first bisectrix in this map are operations points for a heated channel where the boiling boundary (i.e., where $X = 0$) is reached at the exit of the channel. Above the first bisectrix there is subcooled liquid at the exit. All operation points with equal quality at the outlet are in parallel to the first bisectrix until there is saturated steam ($X = 1$) at the exit. Below the iso-quality line for saturated steam there is superheated vapor. The neutral stability boundary for density wave oscillations lies between the iso-quality line $X = 0$ and the iso-quality line $X = 1$, with an asymptote corresponding to constant exit quality for big Subcooling Numbers and a tendency to bigger Phase Change Number for low subcooling number. Further, $\overline{\lambda} = \lambda/L_H$ is defined with the length, $L_H$, of the heated channel as the relative axial height where the boiling boundary is reached assuming thermal equilibrium conditions. All straight lines going through the origin are flow channels with the boiling boundary $\lambda$ at the same relative axial height (Figure 3.1).

## 3.2 Nondimensional Parameters for Heated Channels with Supercritical Fluids

It is natural to represent the results of a linear stability analysis in terms of nondimensional parameters for supercritical water similar to what is done for two-phase flow with the Subcooling-Number ($\mathrm{N_{SUB}}$) and Phase-Change-Number ($\mathrm{N_{PCH}}$). The equations Eq(2.52), Eq(2.53), Eq(2.54) and Eq(2.55) are converted into dimensionless form choosing convenient reference parameters.

Mass conservation equation:

$$\frac{\partial \rho}{\partial t} + \frac{\partial(\rho u)}{\partial z} = 0 \quad . \tag{3.6}$$

Momentum conservation equation:

$$\frac{\partial(\rho u)}{\partial t} + \frac{\partial p}{\partial z} + \frac{\partial(\rho u^2)}{\partial z} = -g\rho\sin\Theta - \frac{f}{2D_H}\rho u^2 \quad . \tag{3.7}$$
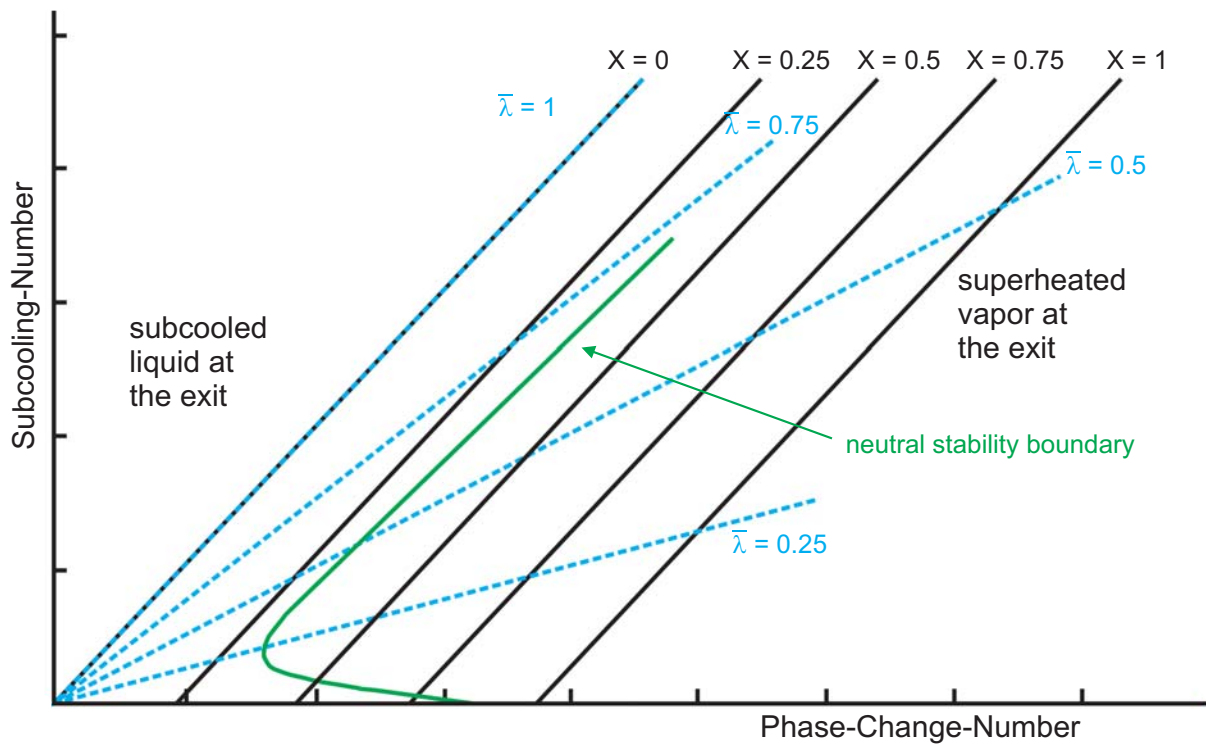
Figure 3.1: $N_{SUB}$ vs. $N_{PCH}$ expand the so-called Ishii-Zuber-Stability-Plane. The first bisectrix is the boiling boundary (quality $X = 0$). For fluid states above the bisectrix we have subcooled liquid. In parallel to $X = 0$ we have iso-quality lines until we reach $X = 1$. Below $X = 1$ we have superheated vapor. Further iso-boiling lengths are straight lines through the origin. [36]

Energy conservation equation:

$$\frac{\partial(\rho h)}{\partial t} + \frac{\partial(h\rho u)}{\partial z} = \frac{\bar{q}''P_H}{A_{x-s}} \quad .$$

(3.8)

State equation:

$$\rho = \rho(h)_p \quad .$$

(3.9)

Due to the characteristics of the relationship between density and enthalpy for a uniformly heated pipe with constant cross-flow area, a characteristic frequency of fluid expansion can be defined for supercritical and constant system pressure conditions as

$$\Omega_\rho = \left(\frac{\partial v}{\partial h}\right)_p G\frac{dh}{dz} = \left(\frac{\partial v}{\partial h}\right)_p \frac{\bar{q}''P_H}{A_{x-s}} \quad .$$

(3.10)

This frequency can be averaged over the heated length $L_H$ of the channel to obtain

$$\overline{\Omega}_\rho = \frac{G}{L_H} \int_0^{L_H} \left(\frac{\partial v}{\partial h}\right)_p \frac{dh}{dz}dz = \frac{G}{L_H} \left(v(L_H) - v_{\text{in}}\right) \quad .$$

(3.11)

It is intuitive to use the heated channel length $L_H$ for non-dimensionalizing geometric parameters

$$z^* = \frac{z}{L_H}, \quad P_H^* = \frac{P_H}{L_H}, \quad D_H^* = \frac{D_H}{L_H}, \quad A_{x-s}^* = \frac{A_{x-s}}{L_H^2} \quad .$$

(3.12)

Furthermore, the channel averaged frequency of fluid expansion can be applied to non-dimensionalize

$$t^* = t\overline{\Omega}_\rho, \quad \Omega_\rho^* = \frac{\Omega_\rho}{\overline{\Omega}_\rho} \quad ,$$

(3.13)

where,

$$u^* = \frac{u}{\overline{\Omega}_\rho L_H}, \quad h^* = \frac{hA_{x-s}u_{\text{in}}\rho_{\text{in}}}{\bar{q}''P_H L_H}, \quad \rho^* = \frac{\rho}{\rho_{\text{in}}}, \quad v^* = \frac{v}{v_{\text{in}}}$$

(3.14)

and finally,

$$\text{Fr} = \frac{u_{\text{in}}^2}{gL_H}, \quad p^* = \frac{p}{\overline{\Omega}_\rho^2 L_H^2 \rho_{\text{in}}} \quad .$$

(3.15)

Dividing Eq(3.6) by $\rho_{\text{in}}\overline{\Omega}_\rho$ results in

$$\frac{\partial\rho^*}{\partial t^*} + \frac{\partial}{\partial z^*}(\rho^*u^*) = 0 \quad .$$

(3.16)

Similarly, dividing Eq(3.7) by $\rho_{in}\overline{\Omega}_\rho^2 L_H$ yields

$$\frac{\partial(\rho^* u^*)}{\partial t^*} + \frac{\partial p^*}{\partial z^*} + \frac{\partial(\rho^* u^{*2})}{\partial z^*} = -\frac{1}{\text{Fr N}_{\text{P-PCH}}^2} - \Lambda \rho^* u^{*2} \quad . \tag{3.17}$$

where the so-called friction number is

$$\Lambda = \frac{f L_H}{2 D_H^*} \quad . \tag{3.18}$$

Dividing Eq(3.8) by $\frac{\bar{q}'' P_H}{A_{x-s}}\frac{\overline{\Omega}_\rho L_H}{u_{\text{in}}}$ yields

$$\rho^* \frac{\partial h^*}{\partial t^*} + \rho^* u^* \frac{\partial h^*}{\partial z^*} = \frac{1}{\text{N}_{\text{P-PCH}}} \tag{3.19}$$

and

$$\rho^* = \rho^*(h^*)_p \quad , \tag{3.20}$$

where the Pseudo-Phase-Change-Number is defined as

$$\text{N}_{\text{P-PCH}} = \frac{\overline{\Omega}_\rho L_H}{u_{\text{in}}} = \frac{v_{L_H} - v_{\text{in}}}{v_{\text{in}}} = \frac{u_{L_H} - u_{\text{in}}}{u_{\text{in}}} \quad . \tag{3.21}$$

Similarly, the Pseudo-Subcooling-Number is given by Eqs(3.11) and (3.21) as

$$\text{N}_{\text{P-SUB}} = \frac{\overline{\Omega}_\rho \lambda}{u_{\text{in}}} = \frac{[v_{L_H} - v_{\text{in}}]\lambda}{v_{\text{in}} L_H} = \frac{[u_{L_H} - u_{\text{in}}]\lambda}{u_{\text{in}} L_H} = \text{N}_{\text{P-PCH}}\frac{\lambda}{L_H} \quad . \tag{3.22}$$

Note that $\lambda$ is defined as the axial length at which the bulk temperature becomes a specified reference temperature. The most striking reference temperature for supercritical water is the pseudo-critical point (e.g. 384 °C at 25 MPa), where a significant change in density occurs. Similarly, for two-phase systems $\lambda$ is the boiling boundary where $h = h_f$ (i.e., the enthalpy of saturated liquid).

Figure 3.2 shows that there is a smooth transition from the saturation temperature to pseudo-critical temperature for the pressure range of interest.

The stability map in terms of $\text{N}_{\text{P-SUB}}$ vs. $\text{N}_{\text{P-PCH}}$ is the super-critical equivalent of the Ishii-Zuber stability plane for two-phase flow (Figure 3.3). The first bisectrix is the iso-exit-enthalpy line corresponding to the pseudocritical temperature. Lines with equal exit enthalpy corresponding to higher exit temperatures are in parallel. Furthermore, in analogy to the two-phase flow case, straight lines through the origin correspond to equal lengths where the reference temperature is reached.

In order to compare these non-dimensional numbers with those normally used for phase change systems, recall that in the case of a homogeneous equilibrium model (HEM) for two-phase flow the form is [53]

$$\left(\frac{\partial v}{\partial h}\right)_p = \frac{\partial\left(v_f + \left(\frac{h-h_f}{h_{fg}}\right)\right)}{\partial h} = \frac{v_{fg}}{h_{fg}} \quad . \tag{3.23}$$
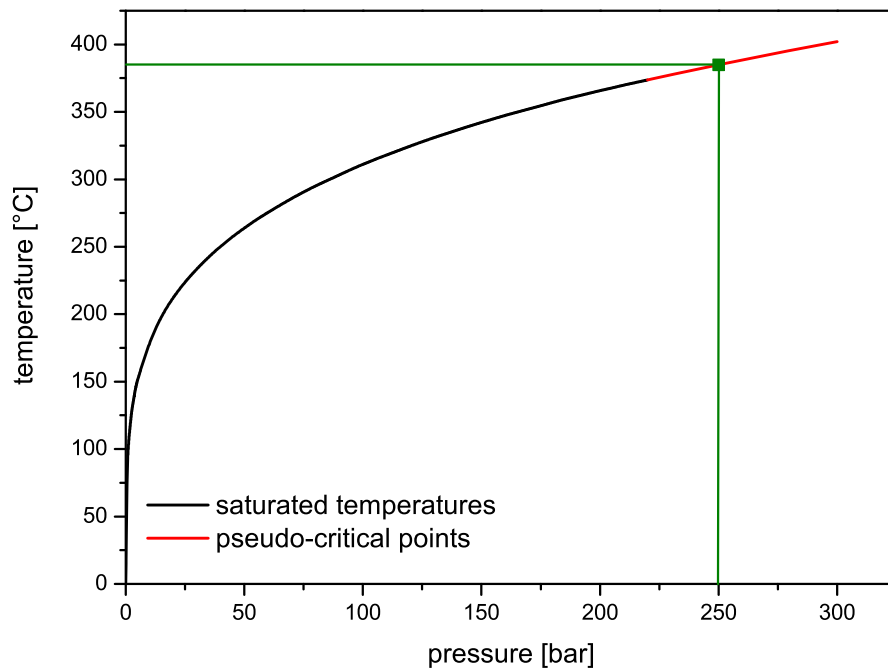
Figure 3.2: Temperature vs. pressure. The black line shows the temperatures of the saturated states at certain pressures for water at sub-critical conditions. The saturated states provide reference properties of the fluid for the Phase-Change-Number and the Subcooling-Number. The end of the black line is the thermodynamical critical point at a pressure of $p_c = 22.06$ MPa and a temperature of $T_C = 373.9$ °C. The red line indicates the pseudo-critical points at the supercritical region which is the referent properties of the fluid for the Pseudo-Phase-Change-Number and the Pseudo-Subcooling-Number. For the case of interest here, the pseudo-critical point at operation pressure of HPLWR (25 MPa) is illustrated in green.
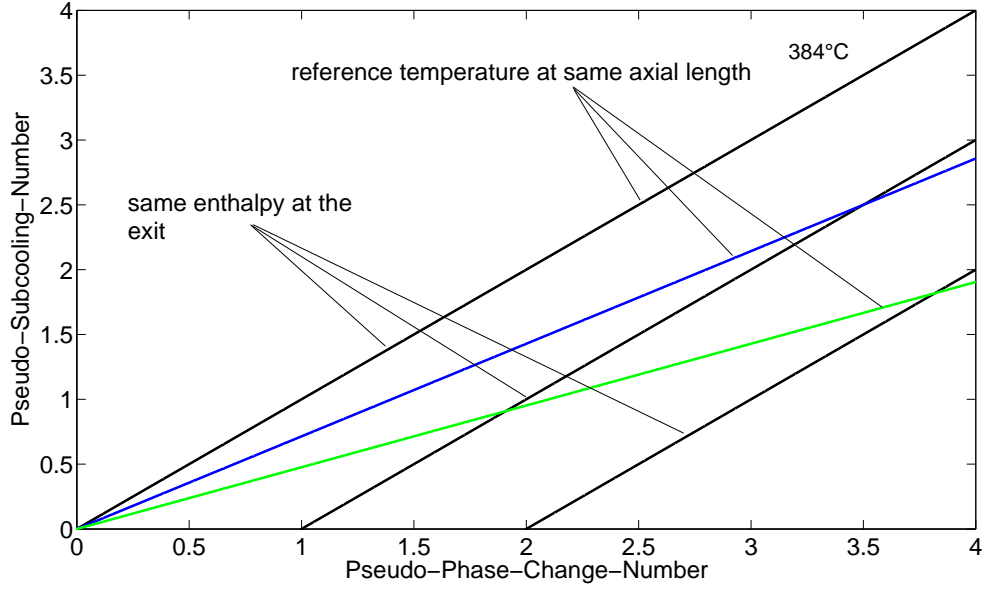
Figure 3.3: The two-dimensional plane of $N_{\text{P-SUB}}$ vs. $N_{\text{P-PCH}}$ is the supercritical equivalent of a two-phase stability map.

Thus, from Eq(3.10) and Eq(3.23) it can be inferred that

$$\Omega_\rho = \overline{\Omega}_\rho = \frac{v_{fg}}{h_{fg}} \frac{\bar{q}'' P_H}{A_{x-s}} \quad . \tag{3.24}$$

Hence Eq(3.21) yields

$$N_{\text{P-PCH}} \equiv \frac{v_{fg}}{h_{fg}} \frac{\bar{q}'' P_H}{A_{x-s}} \frac{L_H}{u_{\text{in}}} \triangleq \frac{v_{fg}}{h_{fg}} \frac{\bar{q}'' P_H}{A_{x-s}} \frac{L_H}{v_f G} \equiv N_{\text{PCH}} \quad , \tag{3.25}$$

where $N_{\text{PCH}}$ is the conventional definition of the Phase-Change-Number [36]. Similarly, an energy balance for a uniformly heated pipe yields [53]

$$\frac{\lambda}{u_{\text{in}}} = \frac{A_{x-s} \Delta h_{\text{SUB}}}{v_f \bar{q}'' P_H} \quad . \tag{3.26}$$

Thus, Eq(3.22) and Eq(3.25) yield

$$N_{\text{P-SUB}} \equiv \frac{v_{fg} (h_f - h_{\text{in}})}{h_{fg} v_f} \triangleq \frac{v_{fg} \Delta h_{\text{SUB}}}{h_{fg} v_f} \equiv N_{\text{SUB}} \quad , \tag{3.27}$$

where $N_{\text{SUB}}$ is the standard subcooling number of phase change systems [36]. Note that, for the case of interest here (uniform axial heat flux),

$$\frac{\lambda}{L_H} = \frac{h_\lambda - h_{\text{in}}}{h_{L_H} - h_{\text{in}}} \quad , \tag{3.28}$$

where at 25 MPa, $h_\lambda = h(384\,°\text{C})$. Thus, Eq(3.22) can be rewritten as,

$$\text{N}_{\text{SUB}} = \frac{(v_{L_H} - v_{\text{in}})}{v_{\text{in}}} \frac{(h_\lambda - h_{\text{in}})}{(h_{L_H} - h_{\text{in}})} \quad . \tag{3.29}$$

This form of the Pseudo-Subcooling-Number is similar in form to that of phase change systems, Eq(3.4).

## 3.3 Alternative Approaches of Nondimensional Groups for Supercritical Flow

Two different nondimensional parameters for supercritical water have been developed by other authors. Zhao et al. [79] selected at a pressure of 25 MPa, $h_A = h = h_\lambda(350\,°\text{C})$ and $h_B = h(404\,°\text{C})$, and approximated the state equation with three linear slopes. Zhao's formulation of the Pseudo-Subcooling-Number, Eq(3.30), is similar in form to that of Eq(3.29):

$$\text{N}_{\text{P-SUB}} = \frac{(v_B - v_A)}{v_A} \frac{(h_A - h_{\text{in}})}{(h_B - h_A)} \quad . \tag{3.30}$$

Nevertheless, the approximations done by Zhao et al. [79] and the choice of two reference temperatures are unnecessary and will make scaling from fluid-to-fluid difficult. Another definition of the Pseudo-Subcooling-Number for supercritical water was proposed by Ambrosini and Sharabi [2]:

$$\text{N}_{\text{P-SUB}} = \frac{\beta_{\text{pc}}}{c_{p,\text{pc}}} (h_{\text{pc}} - h_{\text{in}}) \quad , \tag{3.31}$$

where

$$\beta_{\text{pc}} = \frac{1}{v_{\text{pc}}} \left(\frac{\partial v}{\partial T}\right)_{p,\text{pc}} = \frac{c_{p,\text{pc}}}{v_{\text{pc}}} \left(\frac{\partial v}{\partial h}\right)_{p,\text{pc}} \tag{3.32}$$

and subscript pc denotes pseudo-critical conditions. However, the form with the linear isobaric thermal expansion coefficient is an approximation at a point where fluid properties behave strongly nonlinear (Figure 3.4).

Zhao et al. [79] assumed the validity of a perfect gas law for a supercritical liquid at high temperature. That is,

$$v = \frac{\text{R}T}{p} = \frac{\text{R}h}{pc_p} \tag{3.33}$$

hence,

$$\left(\frac{\partial v}{\partial h}\right)_p = \frac{\text{R}}{pc_p} \quad . \tag{3.34}$$
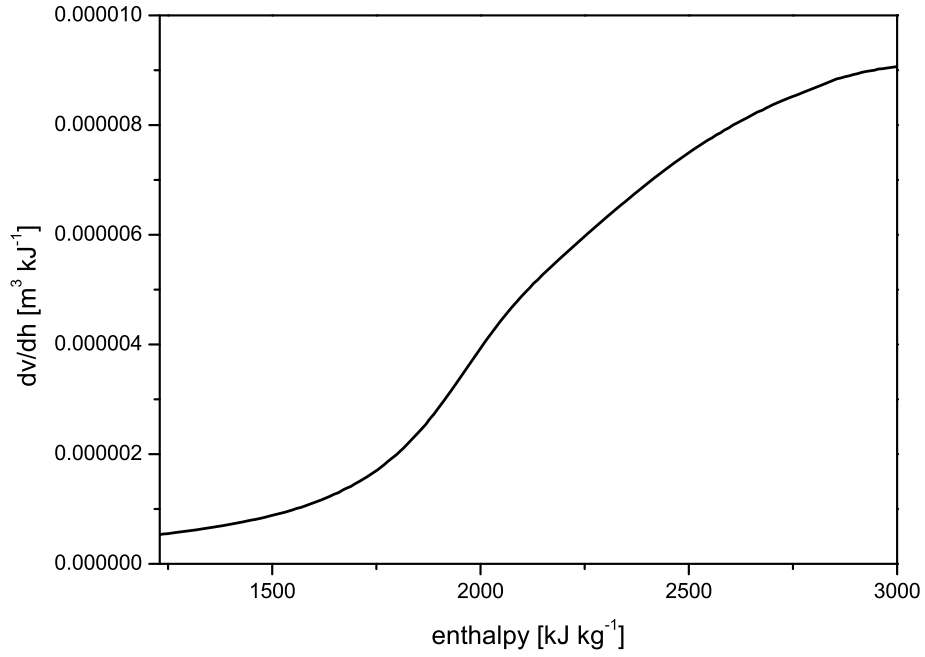
Figure 3.4: Derivative of specific volume with respect to the enthalpy vs. enthalpy.

Yielding, from Eq(3.10),

$$\Omega_\rho = \bar{\Omega}_\rho = \frac{R}{pc_p}\frac{\bar{q}''P_H}{A_{x-s}} \quad . \tag{3.35}$$

Now, since

$$\frac{\partial u}{\partial z} = \Omega_\rho \tag{3.36}$$

and assuming $p >> \Delta p$ (so that p, $c_p$ and R are constant), it can be inferred from Eq(3.36), that

$$u(L_H) - u_{\text{in}} = \bar{\Omega}_\rho L_H \quad . \tag{3.37}$$

Zhao et al. [79] defined an Expansion-Number as

$$N_{\text{exp}} = \frac{\bar{\Omega}_\rho L_H}{u_{\text{in}}} \quad , \tag{3.38}$$

which is formally equivalent to Eq(3.21), however $N_{\text{exp}} \neq N_{\text{P-PCH}}$. Therefore,

$$\bar{\Omega}_\rho = \frac{R}{pc_p}\frac{\bar{q}''P_H}{A_{x-s}} \neq \frac{G}{L_H}\left[v(L_H) - v_{\text{in}}\right] \tag{3.39}$$
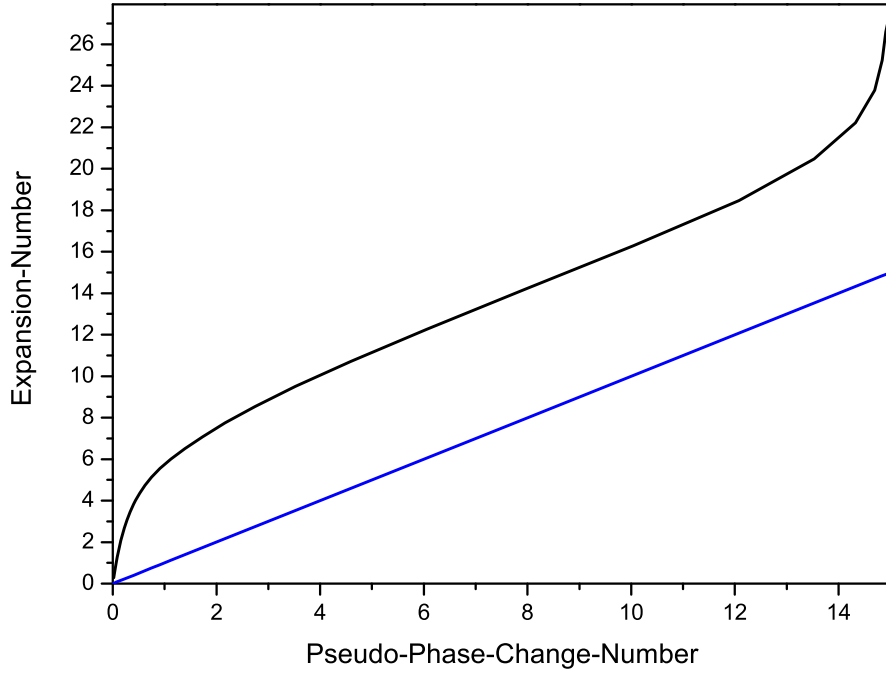
Figure 3.5: Expansion-Number vs. Pseudo-Phase-Change-Number

thus, the expansion number proposed by Zhao et al. [79] differs from the rigorous Pseudo-Phase-Change-Number given in Eq(3.21). In addition, as previously noted, Zhao et al. [79] definition of the Pseudo-Subcooling-Number is different from the rigorous result given in Eq(3.29).

It is interesting to evaluate $\beta_{\mathrm{pc}}$ in Eq(3.31) and Eq(3.32) using the perfect gas assumption. This implies that the Pseudo-Phase-Change-Number proposed by Ambrosini and Sharabi [2] is,

$$\mathrm{N_{P\text{-}PCH}} \equiv \frac{\beta_{\mathrm{pc}}\bar{q}''P_H L_H}{\rho_{\mathrm{pc}}u_{\mathrm{in}}A_{x-s}c_{p,\mathrm{pc}}} = \frac{\mathrm{R}\bar{q}''P_H L_H}{pu_{\mathrm{in}}A_{x-s}c_{p,\mathrm{pc}}} \quad , \tag{3.40}$$

which may be identified as the Expansion-Number ($\mathrm{N_{exp}}$) of Zhao et al. [79]. However, the Pseudo-Subcooling-Number of Ambrosini and Sharabi [2] is different from prior definitions and is given by

$$\mathrm{N_{P\text{-}SUB}} \equiv \frac{\beta_{\mathrm{pc}}}{c_{p,\mathrm{pc}}}\left(h_{\mathrm{pc}} - h_{\mathrm{in}}\right) = \frac{\mathrm{R}\left(h_{\mathrm{pc}} - h_{\mathrm{in}}\right)}{pv_{\mathrm{pc}}c_{p,\mathrm{pc}}} \quad . \tag{3.41}$$

It should be stressed that the approximations used by Zhao et al. [79] and Ambrosini et al. [2] are unnecessary and, as can be seen in Figure 3.5, can yield quite different numerical results from those discussed herein.

# 4 Numerics

The equation set presented in Chapter 2 is implemented in COMSOL [14]. COMSOL is a powerful environment for modeling and solving scientific and engineering problems, which are based on partial differential equations (PDEs). The PDEs can be solved in three application modes: the *coefficient form*, suitable for linear or nearly linear models; the *general form*, which is suitable for non-linear problems (in the mathematical context this form is referred to as strong or hard form); finally, the *weak form*, which is chosen for the implementation of the equation set used here (Section 4.3). After the setup of an application mode, various types of analyses can be performed, including steady-state linear and non-linear analyses, time-dependent analyses and modal analyses. In order to solve the PDEs, COMSOL applies the Finite Element Method (FEM) [29] in conjunction with a variety of numerical solvers. Once a PDE is solved, COMSOL provides post-processing routines for data handling and visualization.

In the authors early published papers on HPLWR stability (e.g [46]) the employed software platform was named FEMLAB. During the time of this thesis FEMLAB changed its name to COMSOL.

## 4.1 COMSOL Notation

COMSOL requests a special notation which will be described in this section. The equation set for the thermal-hydraulic system derived in Chapter 2 is highly non-linear. Thus, either strong or weak form should be used. In the general application mode or strong form the partial differential equation is described as

$$\mathbf{d_a}\frac{\partial \zeta}{\partial t} + \nabla\Gamma = \mathbf{F} \quad , \tag{4.1}$$

where $\zeta$ is a variable in the so-called numerical *subdomain* $\Omega$. $\Gamma$ is the conservative flux function and $\nabla$ is the Nabla operator. $\mathbf{F}$ is the COMSOL source term.

On the boundaries, $\partial\Omega$, Dirichlet $\mathbf{R}$, and Neumann conditions $\mathbf{G}$ are defined as

$$-\mathbf{n}\Gamma = \mathbf{G} + \left(\frac{\partial \mathbf{R}}{\partial \zeta}\right)^T \mu_L; \quad \mathbf{0} = \mathbf{R} \quad , \tag{4.2}$$

where $\mathbf{n}$ is the normal vector on $\partial\Omega$ and $\mu_L$ is a Lagrangian multiplier.

COMSOL is a commercial software. The source code is not available to the author of this thesis. In principle, there are many different possibilities to implement the thermal-hydraulic model into the software. However, most of these possibilities are not resulting in a converged solution. Nevertheless, COMSOL provides a rich model library for chemical, physical and engineering problems. After the inspection of various non-linear models of this library, a conclusion was that the equations set for the thermal-hydraulic systems

must be expressed with time derivatives on the left hand side and, both, spatial derivatives and sources have to be merged into the COMSOL-source-term $\mathbf{F}$ on the right hand side ($\mathbf{F} = (F_1, F_2, F_3)^T$). In that way, the equation set of Chapter 2 becomes:

Energy conservation equation:

$$\frac{\partial h}{\partial t} = \underbrace{v \frac{q'' P_H}{A_{x-s}} - Gv \frac{\partial h}{\partial z}}_{F_1} \quad . \tag{4.3}$$

Momentum conservation equation:

$$\frac{\partial G}{\partial t} = \underbrace{-\frac{\partial (G^2 v)}{\partial z} - \frac{\partial p}{\partial z} - \frac{g_{eff}}{v} - \left[ K_{in}\delta(z) + K_{out}\delta(z-L) + \frac{f}{D_H} \right] \frac{(G^2 v)}{2}}_{F_2} \quad . \tag{4.4}$$

Mass conservation equation:

$$\frac{\partial h}{\partial t} = \underbrace{v^2 \frac{\partial G}{\partial z} \left( \frac{\partial v}{\partial h} \right)^{-1}}_{F_3} \quad . \tag{4.5}$$

Another experience was, that the energy equation must be listed at first position. Next comes the momentum equation, then the mass equation. Since the state equation $\rho = \rho(h)$ is of algebraic form, it can be expressed as a sub-function, the so-called *subdomain expression*. Furthermore, note that the mass term is unity; that means, $d_a = 1$ (e.g. Eq(4.5)).

## 4.2 Dynamic Head

In order to have a good convergence of the equation system, the momentum equation is rearranged. The state variable corresponding to the transient of the momentum conservation equation is the mass flux $G$. In that way a dynamic pressure, $p_d$, can be defined as the sum of the static pressure and the dynamic head,

$$p_d = p + G^2 v \quad . \tag{4.6}$$

Hence,

$$\frac{\partial G}{\partial t} = -\frac{\partial p_d}{\partial z} - \frac{g_{\text{eff}}}{v} - \frac{f}{D_H} \frac{(G^2 v)}{2} \quad . \tag{4.7}$$

Note that the convection term is substituted into the (Dirichlet) boundary conditions. For example, at the inlet of the flow channel (in COMSOL-notation)

$$0 = -p + p_{\text{in}} + G^2 v_{\text{in}} + K_{\text{in}} G^2 v_{\text{in}} \quad . \tag{4.8}$$

Employing $p_d$ instead of $p$, the fast changing component is transfered into the boundary

conditions. This results in a smooth solution for the momentum equation, which is solved in the numerical *subdomain*. Furthermore, the momentum equation is solved with shape functions which are one order smaller compared to the order of shape functions for the mass and the energy equation (for details see [15]). The shape functions for the mass and the energy equation are of order five. The numerical approach chosen solves the conservation equations with high nodal solution. For a heated axial length of 4.2 m, there are 240 nodes. This results in a mesh size of 1.75 cm providing that results of the anaylses are independent of the numerical scheme (see Section 6.3).

## 4.3 The Weak Formulation

To establish a good numerical convergence for the non-linear thermal-hydraulic equation system, the COMSOL solver routines need an accurate Jacobian matrix. A model described in weak formulation automatically produces an exact Jacobian matrix [14]. For the conversion of the strong form to weak formulation, an arbitrary function $\nu$, the so-called test-function, is considered, which is well-behaved on the sub-domain $\Omega$. Multiplying the test-function with the steady-state version of Eq(4.1) and integrating over $\boldsymbol{\Omega}$ yields

$$\int_\Omega \nu \nabla \Gamma \mathbf{dA} = \int_\Omega \nu \mathbf{F} \mathbf{dA} \quad , \tag{4.9}$$

where $\mathbf{dA}$ is the area element. For the case of interest here, a one-dimensional *subdomain* the Eq(4.10) becomes

$$\int_\Omega \nu \frac{\partial \Gamma}{\partial z} dz = \int_\Omega \nu F_z dz \quad . \tag{4.10}$$

Now, integration by parts leads to

$$[\nu \Gamma]_{z_r}^{z_l} - \int_\Omega \frac{\partial \nu}{\partial z} \Gamma dz = \int_\Omega \nu F_z dz \quad , \tag{4.11}$$

where $z_l$ and $z_r$ indicate the left and the right border of $\boldsymbol{\Omega}$. Using the boundary condition from (Eq(4.2)) to finally receive

$$0 = \int_\Omega \left( \frac{\partial \nu}{\partial z} \Gamma + \nu F_z \right) dz + \nu \left[ G + \left( \frac{\partial R}{\partial \zeta} \right) \mu_L \right]_{z_r}^{z_l} \quad . \tag{4.12}$$

By changing the application mode, COMSOL provides an automatic conversion of the strong form to the weak formulation including the transient term.

## 4.4 Analysis Method

It is instructive to consider an overview of the analysis which is performed within COMSOL in strong form . To this end, the equations (Eq(4.3), Eq(4.7) and Eq(4.5)) may be written in matrix form as:

$$\underline{\underline{A}} \frac{\partial \underline{\Psi}}{\partial t} + \underline{\underline{B}} \frac{\partial \underline{\Psi}}{\partial z} = \underline{c} \tag{4.13}$$

where the vector of the unknowns is

$$\underline{\Psi} = \begin{pmatrix} G \\ p_d \\ h \end{pmatrix} \tag{4.14}$$

and,

$$\underline{\underline{A}} = \begin{bmatrix} 0 & 0 & \frac{1}{v^2}\left(\frac{\partial v}{\partial h}\right)_p \\ 1 & 0 & 0 \\ 0 & 0 & \frac{1}{v} \end{bmatrix} \tag{4.15}$$

$$\underline{\underline{B}} = \begin{bmatrix} 1 & 0 & 0 \\ 0 & 1 & 0 \\ 0 & 0 & G \end{bmatrix} \tag{4.16}$$

$$\underline{c} = \begin{pmatrix} 0 \\ -\frac{g_{\text{eff}}}{v} - \frac{fG^2 v}{2D_H} \\ \frac{\bar{q}'' P_H}{A_{x-s}} \end{pmatrix} \tag{4.17}$$

the equation can be evaluated in the time domain numerically (i.e., by differencing the spatial derivatives and using the method of lines) subject to various initial and boundary conditions. In particular, for the so-called parallel channel instability case, a constant static pressure drop ($\Delta p$) across the channel is specified (see Chapter-6). The steady-state solution, $\underline{\Psi}_0$, comes from numerically evaluating the steady-state version of the equation set,

$$\frac{\partial \underline{\Psi}_0}{\partial z} = \underline{\underline{B}}^{-1} \underline{c} \tag{4.18}$$

The principles of the stability analysis in the frequency domain for thermal-hydraulics is illustrated in Figure 4.1. The non-linear equation set is converted into a linear equation set (in time-domain) by applying first order perturbation theory. Assuming a modal ansatz the equations are transfered into an algebraic equation set in the frequency domain. For given boundary conditions and operation parameters a spectra of complex conjugated eigenvalues is computed.

In order to analyze the dynamic stability characteristics of the heated channel, Eq(4.13) is linearized for fully developed flow about the steady-state (i.e., the so-called fixed points), $\underline{\Psi}_0$, and the resultant linear equation is:

$$\underline{\underline{A}}_0 \frac{\delta \underline{\Psi}}{\partial t} + \underline{\underline{B}}_0 \frac{\delta \underline{\Psi}}{\partial z} = \underline{\underline{C}}_0 \delta \underline{\Psi} \tag{4.19}$$

where,

$$\underline{\Psi}(z,t) = \underline{\Psi}_0(z) + \delta \underline{\Psi}(z,t) \tag{4.20}$$

and,

$$\delta \underline{\Psi} = \begin{pmatrix} \delta G \\ \delta p_d \\ \delta h \end{pmatrix} \tag{4.21}$$
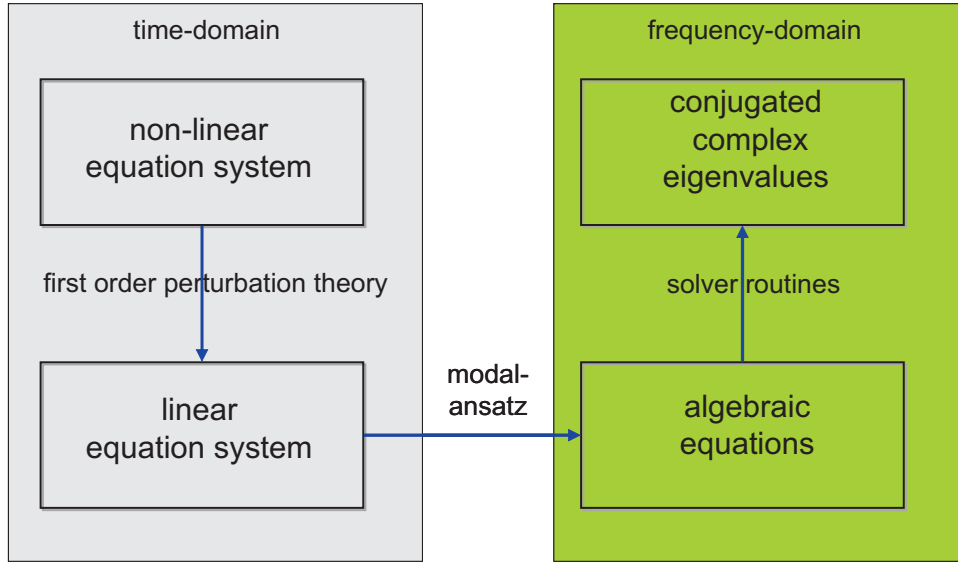
Figure 4.1: Representation of the applied analysis method.

Next, a modal solution of the form,

$$\delta\underline{\Psi}(z,t) = \tilde{\underline{\Psi}}(z)e^{-\Lambda t} \tag{4.22}$$

is applied. Where $\tilde{\underline{\Psi}}$ are the eigenfunctions (i.e., mode shapes) and $\Lambda$ are the complex or real eigenvalues (note that: $\tilde{\underline{\Psi}} \neq \underline{\Psi}_0$). Combining Eqs(4.19) and (4.22) yields the following relation:

$$-\Lambda\underline{\underline{A}}_0\tilde{\underline{\Psi}}_0(z) + \underline{\underline{B}}_0\frac{\partial\tilde{\underline{\Psi}}_0(z)}{\partial z} = \underline{\underline{C}}_0\tilde{\underline{\Psi}}_0(z) \quad . \tag{4.23}$$

If the spatial derivative (using FEM) Eq(4.23) are differentiated the equation can be rewritten as (where $\underline{\underline{D}}_0$ collects contributions from $\underline{\underline{B}}_0$ and $\underline{\underline{C}}_0$),

$$\left(\underline{\underline{A}}_0\Lambda - \underline{\underline{D}}_0\right)\tilde{\underline{\Psi}}(z) = \underline{0} \quad . \tag{4.24}$$

This is the dispersion relation describing the functional dependence of eigenvalues and corresponding eigenfunctions. The only non-trivial solution of Eq(4.24) is

$$det\left(\underline{\underline{A}}_0\Lambda - \underline{\underline{D}}_0\right) = \underline{0} \quad , \tag{4.25}$$

which yields the various eigenvalues,

$$\Lambda = \Lambda_{\text{Re}} \pm i\Lambda_{\text{Im}} \quad . \tag{4.26}$$

Once the eigenvalues are computed, Eq(4.24) yields the eigenfunctions, $\tilde{\underline{\Psi}}(z)$. The considered basic state $\tilde{\underline{\Psi}}_0(z)$ is stable with respect to small perturbations if the real part of

$\Lambda_{\text{Re}}$ of any eigenvalues is positive, and the basic state becomes unstable if a single real eigenvalue, or a pair of conjugate complex eigenvalues, crosses the axis $\Lambda_{\text{Re}} = 0$ into the left half plane, as a parameter (i.e. $N_{\text{P-PCH}}$) is changed. The so-called neutral stability boundary is defined by the most limiting complex conjugated pair of eigenvalues where $\Lambda_{\text{Re}} = 0$. It is noted in Eqs(4.22) and (4.26) that a heated flow channel is linearly stable if $\Lambda_{\text{Re}} > 0$ and linearly unstable if $\Lambda_{\text{Re}} < 0$. Normally various values of inlet temperature are chosen and then the channel power level is varied until $\Lambda_{\text{Re}} = 0$. These parametric results may then be plotted in the $N_{\text{P-SUB}}$ vs $N_{\text{P-PCH}}$ plane (stability map: Chapter-3) to define the neutral stability boundary.

## 4.5  Eigenvalue Solver

COMSOL solves eigenvalue problems employing the *femeig*. *femeig* is an algorithm based on "Arnoldi's minimized iteration" method [3] which has great advantage in large eigenvalue problems. The real latent root problem presented in Eq(4.24) represents an characteristic homogeneous set of equations. Depending on the nodal resolution in the discretization process the order of the matrix which has to be solved can get rather large. Without going into mathematical details, it can be stated, that the conventional iterative solutions procedure would begin by an arbitrary column of $\underline{\tilde{\Psi}}$ and converge to the largest dominant latent root [41]. After obtaining the solution, the dominant mode may be removed by any convenient method, so that the second largest root of the original matrix becomes the dominant one of an altered matrix. The same procedure is now repeated until all desired roots of the eigenvalue problem have been obtained. Since the accuracy of the total solution depends upon the accuracy with which each previous root has been determined, the conventionally method requires huge numerical costs (computational resources) and the convergence can be extremely slow if the roots are not widely dispersed. Thus, in previous stability analysis the nodal solution and the accuracy of the obtained results was rather small.

In contrast, by using *femeig* the solution of the original homogeneous equation is replaced by the solution of a matrix equation of reduced order. The algorithm requires the generation of a series of orthogonal functions through which the simple matrix equation of reduced order is established. The reduced matrix equation is then solved directly in terms of polynomial functions obtained in conjunction with the generated orthogonal functions. That allows the handling of large eigenvalue problems with a high number of degrees of freedom.

The validity of *femeig* was verified in various examples of the COMSOL chemical engineering library [13]. Furthermore, the solver was verified in a master thesis obtaining the same eigenvalues by MATHEMATICA [74] and by a COMSOL-model for the well known strange attractor called Roessler-attractor [25].

## 4.6  Benchmark

Before doing a detailed evaluation of the linear and non-linear stability characteristics of the fuel assemblies for the HPLWR, the thermal-hydraulic model is benchmarked with analytic results which are related to the essential physics associated with density-wave phenomena. Thus, the case of a uniformly heated flow channel is considered through

which subcooled liquid is flowing that is subjected to a small harmonic perturbation in inlet velocity. For the case of negligible thermal fluctuation of the heated wall (i.e., constant wall heat flux, $\bar{q}''$), the exact analytic solution is given by [53]:

$$\delta\hat{h}(\omega, z) = -\frac{\bar{q}''P_H}{\rho_f u_{in} A_{x-s}} \left[ \frac{1 - e^{-i\frac{\omega z}{u_{in,0}}}}{i\frac{\omega z}{u_{in,0}}} \right] \frac{\delta\hat{u}_{in}}{u_{in,0}} \tag{4.27}$$

These complex variables can be rewritten in polar coordinates as:

$$\delta\hat{h}(\omega, z) = \sqrt{Re^2(\omega, z) + Im^2(\omega, z)} Ae^{i(\omega t, \Phi)} \tag{4.28}$$

where the phase angle is,

$$\Phi = tan^{-1}\left(\frac{Im(\omega, z)}{Re(\omega, z)}\right) \tag{4.29}$$

and,

$$Re(\omega, z) = -\frac{\bar{q}''P_H \sin\frac{\omega z}{u_{in,0}}}{\omega u_{in,0}\rho_f A_{x-s}} \tag{4.30}$$

$$Im(\omega, z) = -\frac{\bar{q}''P_H \left[1 - \cos\frac{\omega z}{u_{in,0}}\right]}{\omega u_{in,0}\rho_f A_{x-s}} \tag{4.31}$$

For the case of interest here,

$$\delta u_{in} = Ae^{i\omega t} \tag{4.32}$$

where the amplitude A is a small fraction (say 1%) of the magnitude of the steady-state inlet velocity, $u_{in,0}$. The modulus of Eqs(4.27)and (4.28), $|\delta h(t, z; \omega)|$, can be evaluated at various angular frequencies ($\omega$) and times (t), and the results compared with the numerical results of COMSOL. Typical results for t = 50 sec and two different angular frequencies are shown in Figure 4.2. It can be seen that good agreement was achieved. This shows that the thermal-hydraulic model can predict enthalpy waves, and it thus should be able to predict the density perturbations which drive density-wave oscillations.

## 4.7 Validation

Due to the lack of experimental data on the linear stability boundary for supercritical water, a validation was performed based on the DWO stability experiment by Solberg [36]. In particular, a subcritical two-phase system at 80 atm was evaluated using a homogeneous equilibrium model (HEM), which has an equation of state very similar to shown state equation at 7 MPa in Figure 1.10. The experiment of Solberg consisted of a circular tube with heated length of 2.9 m and an diameter of $D = 5.25$ mm. Inlet and
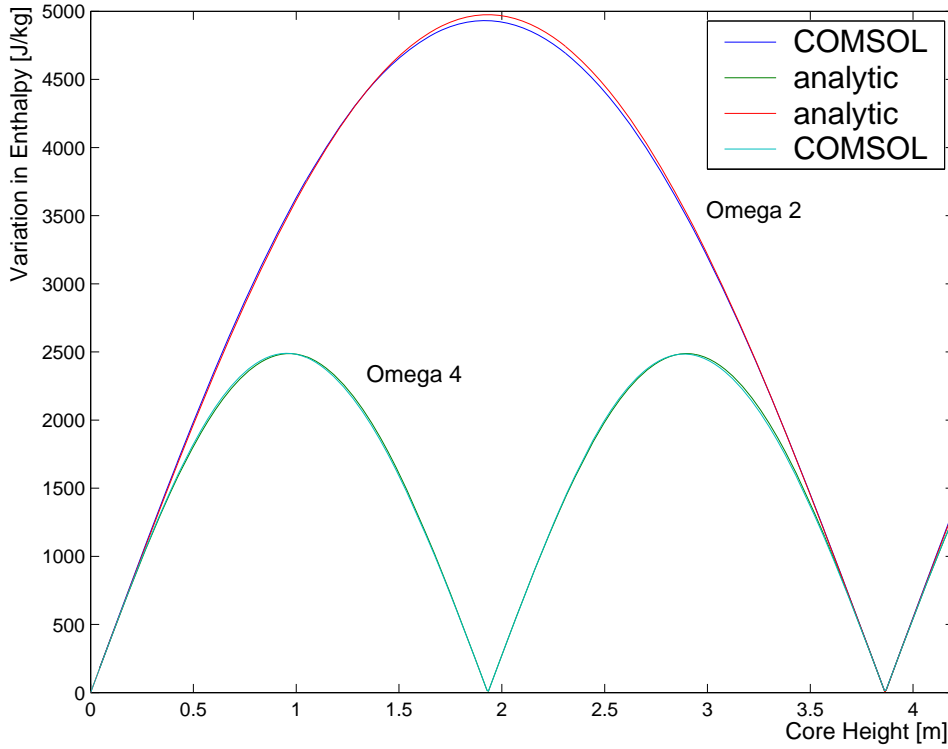
Figure 4.2: Analytic results and numerical solution of an enthalpy wave.

exit orifices were used. The corresponding inlet and exit pressure loss coefficients were $K_{\text{in}} = 35.6$ and $K_{\text{exit}} = 0.006$. A typical parallel channel boundary condition was applied enforcing constant pressure drop of the channel of $\Delta p = 47.8$ kPa. The circular tube was uniformly heated by its electrical resistance. Once a certain inlet temperature was chosen the heat flux into the flow channel was stepwise increased until an unstable density wave oscillation was observed. The data is represented in terms of Phase-Change-Number $N_{\text{PCH}}$ (Eq(3.3)) and Subcooling-Number $N_{\text{SUB}}$ (Eq(3.4)) in the stability map:

$$\text{N}_{\text{PCH}} \equiv \frac{v_g - v_f}{v_f(h_g - h_f)} \frac{\bar{q}'' P_H L}{G A_{x-s}}, \quad \text{N}_{\text{SUB}} \equiv \frac{v_g - v_f}{v_f} \frac{h_f - h_{\text{in}}}{(h_g - h_f)} \tag{4.33}$$

The specific volumes and the enthalpies of the saturated fluid states for water at 80 atm can be obtained using the water steam table [72]: $v_f = 0.00139\ \text{m}^3\text{kg}^{-1}$; $v_g = 0.02317\ \text{m}^3\text{kg}^{-1}$; $h_f = 1322.148$ kJ kg$^{-1}$; $h_g = 2757.025$ kJ kg$^{-1}$. Obviously, the heated perimeter is $P_H = \pi D$ and the cross-sectional flow area is given by $A_{x-s} = \pi D^2/4$.
The state equation is,

$$v = v(h) = v_f + (v_g - v_f)\frac{(h - h_f)}{(h_g - h_f)}(h > h_f) \tag{4.34}$$

For the numerical evaluation, various values of the inlet temperature are chosen and then the channel power level is varied until $\Lambda_{\text{Re}} = 0$. In Figure 4.3 the resulting linear stability map in the Phase-Change-Number/ Subcooling-Number plane is shown in black. The well known shape for the neutral stability boundary can be observed which has an asymptotic behavior of near constant exit quality at large Subcooling-Numbers and
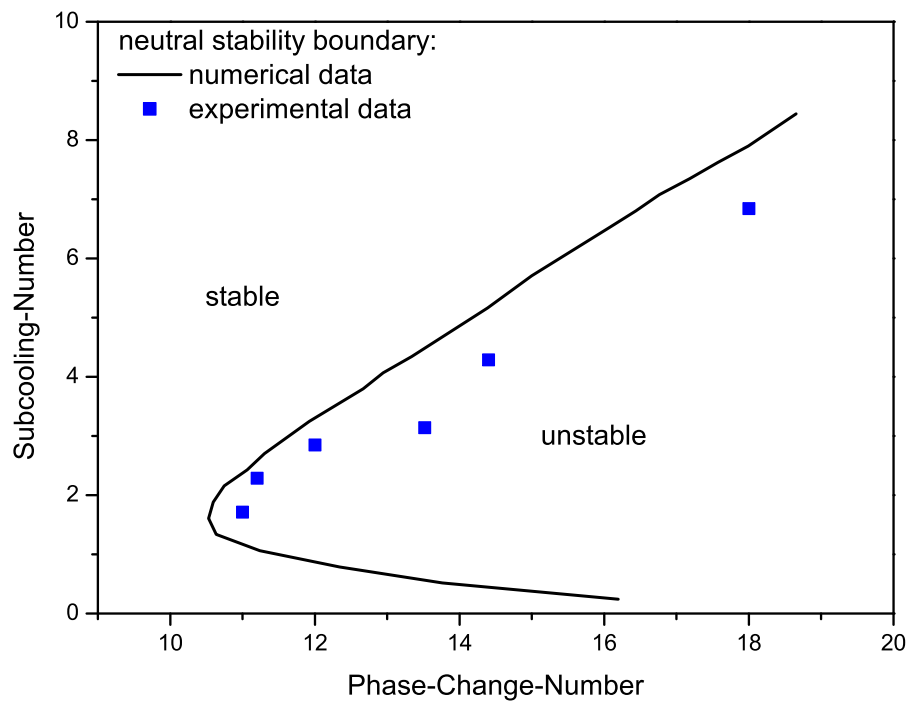
Figure 4.3: Comparison of the neutral stability boundary predicted by the numerical model (black) and experimental data (blue squares).

enhanced stability at low Subcooling-Numbers. The data obtained by the experiments by Solberg is plotted in blue. Note that even though the homogeneous equilibrium model is employed here, which does not take into account effects of subcooled boiling (thermal non-equilibrium) nor drift flux (mechanical non-equilibrium) a quite good agreement between experimental data and numerical evaluation can be observed. In particular, the HEM results in a conservative prediction of the linear stability limit.

# 5 Analysis of Steady-State Flow

As discussed in Chapter 1.5, heated two-phase flow channels exhibit for certain operation parameters an s-shaped steady-state pressure drop/mass flux characteristic. An operation point in the negative slope region of this curve is unstable and leads to flow excursion or so-called Ledinegg instabilities. This instability phenomena is characterized by sudden change in flow rate to a lower value and can only occur if for a certain imposed pressure drop $\Delta p$ several values of flow rate are possible. To calculate the transient the time-dependent conservation equations must be solved. However, the stability criterion (a negative slope in pressure drop/ flow rate curve) is based on steady-state considerations. Flow maldistribution and PDO are very close connected to Ledinegg instabilities and have the same stability criteria.

## 5.1 Steady-State Stability Analysis

The steady-state characteristic of the coolant flow in a fuel assembly can be represented by a single flow channel with equivalent hydraulic diameter and heated perimeter. The equation system given in Eq(4.3), Eq(4.7), and Eq(4.5) can be calculated for the steady-state solution. One exemplary result is shown in Figure 5.1 for an inlet temperature of 310 °C and a linear heat rate of 30 W/m. As there is no negative slope in pressure drop/ mass flux characteristics, there will be no appearance of Ledinegg instabilities, flow maldistribution and pressure drop oscillation under reactor operation conditions.

It has to be pointed out that Ambrosini et al. [1] predicted the occurrence of Ledinegg instability in a flow channel under supercritical pressure conditions. Although, to the authors best knowledge, the published results by Ambrosini et al. [1] are correct, the parameters selected to achieve Ledinegg instability are far out the parameter range for a nuclear reactor. Even in the case of two-phase flow systems the appearance of flow excursions is mainly connected to low system pressure. Typically, the pressure drop/ mass flux characteristics of a two/phase system at 70 bar (pressure level of BWRs) do also not show a negative slop. Thus, the obtained results of the steady-state stability analysis for HPLWR are similar to the experience made with two-phase system.
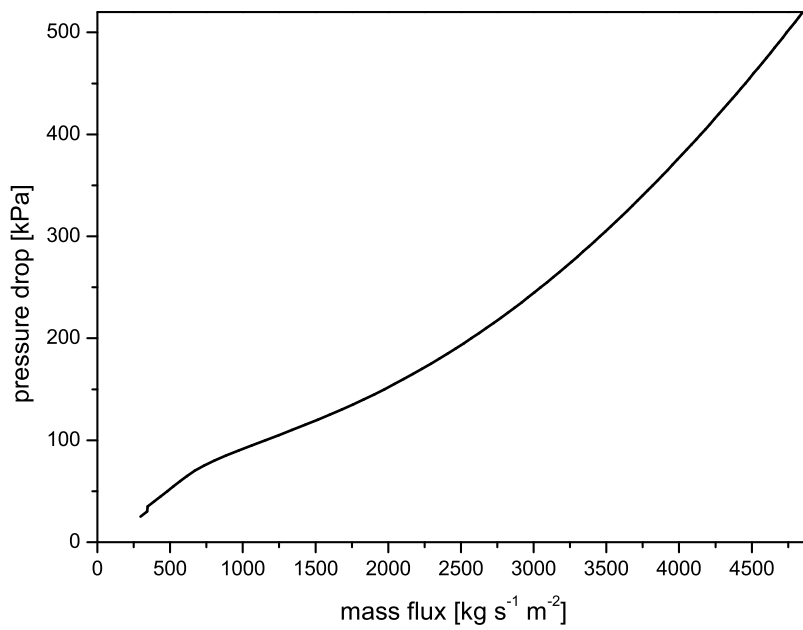
Figure 5.1: Pressure drop vs. mass flux for a heated flow channel at system pressure of 25 MPa ($T_{in} = 310\ °C$ and $q' = 30\ W/m$). As there is no negative slope in characteristics, there will be no appearance of Ledinegg instabilities, flow maldistribution, and pressure drop oscillation.

# 6  Linear Stability of DWO at Supercritical Pressure Conditions

In the previous chapter, the thermal-hydraulic features of the coolant flow were analyzed with respect to their steady-state characteristics. It was shown that flow excursion does not occur at normal operation conditions of the HPLWR. Hence, the only remaining relevant instability phenomena are the various types of density wave oscillation.

## 6.1  The Parallel Channel Case

In a HPLWR III-pass core there are 52 fuel assembly clusters in one heat-up stage. Each cluster consists of nine fuel assemblies. This arrangement can be represented by an array of 468 parallel one-dimensional flow channels, connected by a common inlet plenum and a common outlet plenum (Figure 6.1).

It is obvious that all flow channels must satisfy an equal pressure boundary condition in the lower and upper plenum. Inevitably, due to slight differences in design and operation condition, in such an array of parallel fuel assemblies, one channel is the "most unstable" one. That means, it reaches the threshold of density wave oscillations at certain operation parameters (e.g., by increasing the power level) first. As the total amount of channels is big, the oscillation of mass flow in the single unstable fuel assembly will approximately not affect the total mass flow through the whole core. Thus, the operation parameters of the other stable (steady-state) fuel assemblies remain uneffected. Hence, the stable channels impose a constant pressure drop boundary condition - or so-called parallel channel boundary condition - on the unstable one. This case is referred to as the single channel DWO or the parallel channel case.



Figure 6.1: Scheme of an array of parallel channels coupled by common plena.

Similar thoughts can be carried out including heater dynamics and neutronic feedback during core-wide DWO. The fluctuation in density during DWO of a single unstable fuel assembly will have approximately no effect on the moderation ability of the total fluid within the core. Thus, the single channel DWO can be treated as thermal-hydraulically and neutronically decoupled.

## 6.2 Linear Stability Analysis

To predict the stability threshold of density wave oscillations it is necessary to analyze the time characteristic of the thermal-hydraulic system. In general, this can be done in two ways: either the system has to be solved in the time-domain or a frequency-domain method has to be applied. The results of a linear stability analysis in the frequency-domain will be presented in this chapter. The computational efficiency and the prosperities in predicting the onset of DWO stability of boiling water reactors makes the frequency method very attractive. However, nonlinear transient informations are beyond the scope of the method.

As stated in Section 4.4, the thermal-hydraulic model is converted into a linear equation set (in time-domain) by applying first order perturbation theory. Assuming a modal ansatz, the equation set is transferred into an algebraic equations set in the frequency domain. For a given basic state, parallel channel boundary conditions and inlet temperature of the fluid, a spectra of conjugated complex eigenvalues is computed. Figure 6.2 exemplarily shows the eigenvalue spectra for three power levels of a typical fuel assembly of the evaporator (in detail: $\Delta p = 150$ kPa, $L_H = 4.2$ m, $D_H = 5.336$ mm and $T_{\text{in}} = 310\,°\text{C}$) in terms of imaginary part $Im(\Lambda)$ vs. real part $Re(\Lambda)$ of the eigenvalue. The black points correspond to a power level with $N_{\text{P-PCH}} = 2.4$. The considered basic state is stable, with respect to small perturbations if the real part of all eigenvalues is positive. Thus, the flow channel is in the stable region. By increasing the $N_{\text{P-PCH}}$ ($N_{\text{P-PCH}} = 6$: blue; $N_{\text{P-PCH}} = 7$: red), the real part of the most limiting pair of eigenvalues becomes smaller until it becomes negative and the channel is unstable. The red spectra corresponds to the case where the flow channel just passes neutral stability.

The important parameter for the impulse response is the decay ratio of the perturbation. It is determined as

$$DR = exp\left[-2\pi\frac{Re(\Lambda)}{|Im(\Lambda)|}\right] \quad . \tag{6.1}$$

The decay ratio is a criterion for stability, since values smaller than 1 correspond to stable fuel assemblies. At neutral stability, the decay ratio becomes 1 (Figure 6.3).

## 6.3 Mesh Dependence of Eigenvalues

Before performing the detailed stability analysis, the effect of the discretization on the numerical results is investigated. The most sensitive parameter for stability analysis is the real part of the leading mode, resulting directly in the value of the decay ratio. Previous works indicates that the decay ratio significantly depends on the axial mesh size. Exemplarily, the decay ratio for a flow channel with an inlet temperature of $T_{\text{in}} = 310\,°\text{C}$ very close to the neutral stability boundary is illustrated as a function of mesh size (Figure 6.4). In contrary to former works made in the field of supercritical stability analysis, no dependency of the results on the mesh size can be observed. This fact was very evident, since the numerical scheme solves the conservation equations with fifth
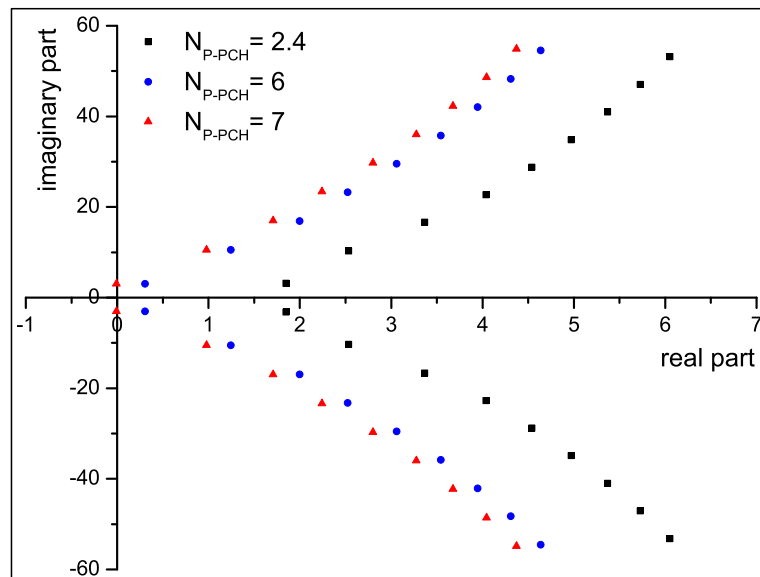
Figure 6.2: Spectrum of eigenvalues for an inlet temperature of $T_{in}$ = 310 °C and different power level. The black points correspond to a power level with $N_{P\text{-}PCH}$ = 2.4. All real parts of the eigenvalues are positive. Thus, the flow channel is in the stable region. By increasing the $N_{P\text{-}PCH}$ ($N_{P\text{-}PCH}$ = 6: blue; $N_{P\text{-}PCH}$ = 7: red), the real part of the most limiting pair of eigenvalues becomes smaller until it gets negative and the channel is unstable.
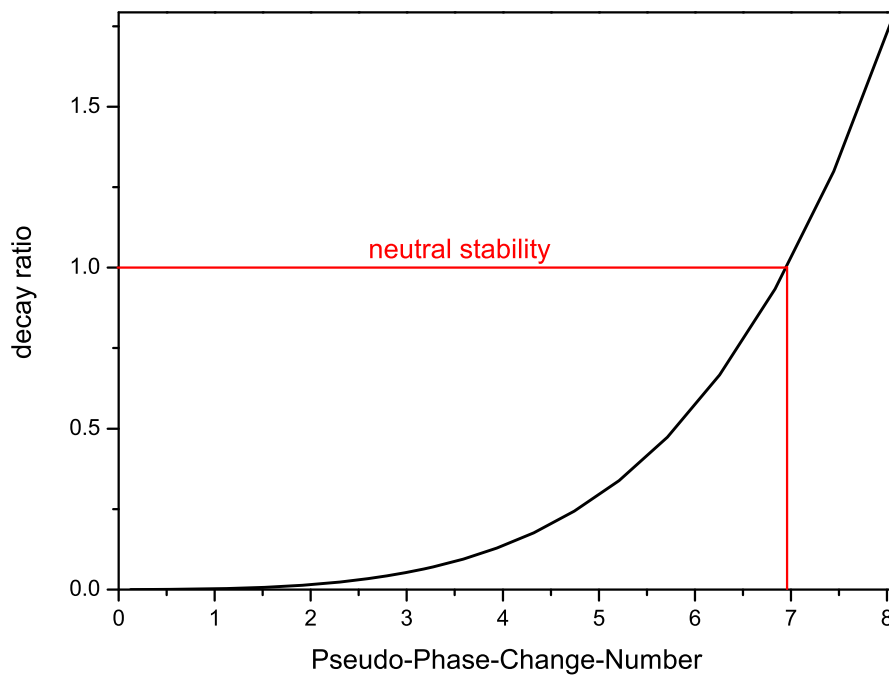


Figure 6.3: Decay ratio vs. Pseudo-Phase-Change-Number.
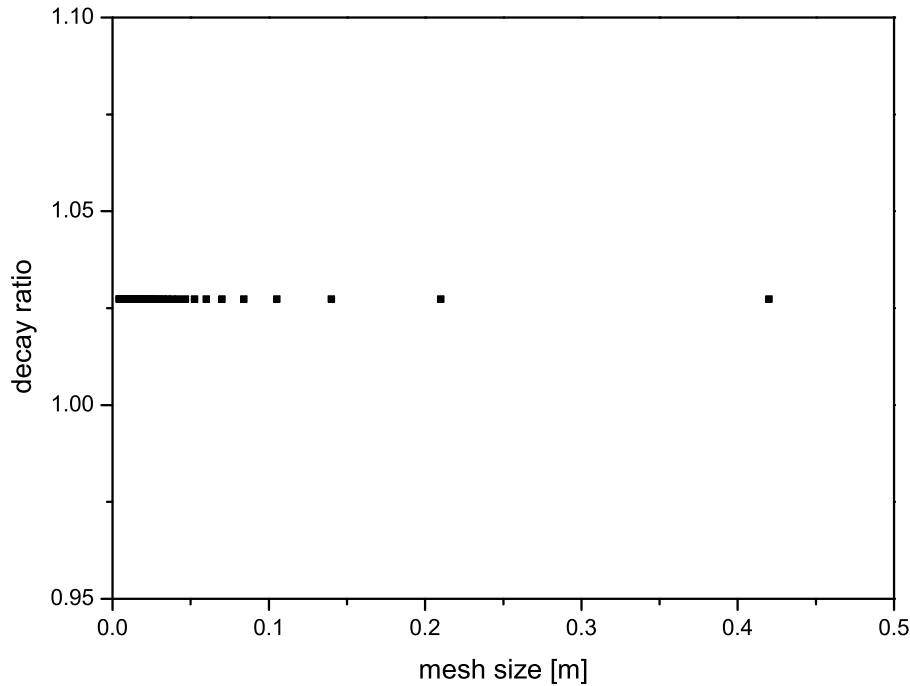
Figure 6.4: Decay ratio vs. mesh size.

order shape functions.

## 6.4 Stability Map

In order to contract stability maps, various values of inlet temperature are chosen, and then the channel power level is varied until the neutral stability boundary is reached. These parametric results may then be plotted in the $N_{P\text{-}SUB}$ vs. $N_{P\text{-}PCH}$ plane (stability map: Chapter 3) to define stable and unstable operations regions of the HPLWR. In the same map, the operation range of the HPLWR III-pass core components can be illustrated (Figure 6.5). Since the inlet and the exit fluid temperatures are known (and so the corresponding enthalpies), the specific volumes can be determined using the state equation. Thus, the $N_{P\text{-}PCH}$ can be calculated for each heating stage at its average operation point and at its operation point with the maximal enthalpy rise estimated by the hot channel factor analysis. For the $N_{P\text{-}SUB}s$, a uniform power profile is assumed. Between the operation points of the average and the hot component, the operation range is indicated by a green line for the evaporator and a blue line for the superheater I. Since the difference in specific volume at the exit between a average and a hot fuel assembly of superheater II is only 0.0033 m$^3$ kg$^{-1}$, the corresponding operation range approximately appears as one single operation point in the figure. The operation ranges of both superheaters lie in the negative $N_{P\text{-}SUB}$ region. This is obvious since, the pseudo-critical point is chosen as reference temperature. The component with the highest values in $N_{P\text{-}SUB}$ is the evaporator.
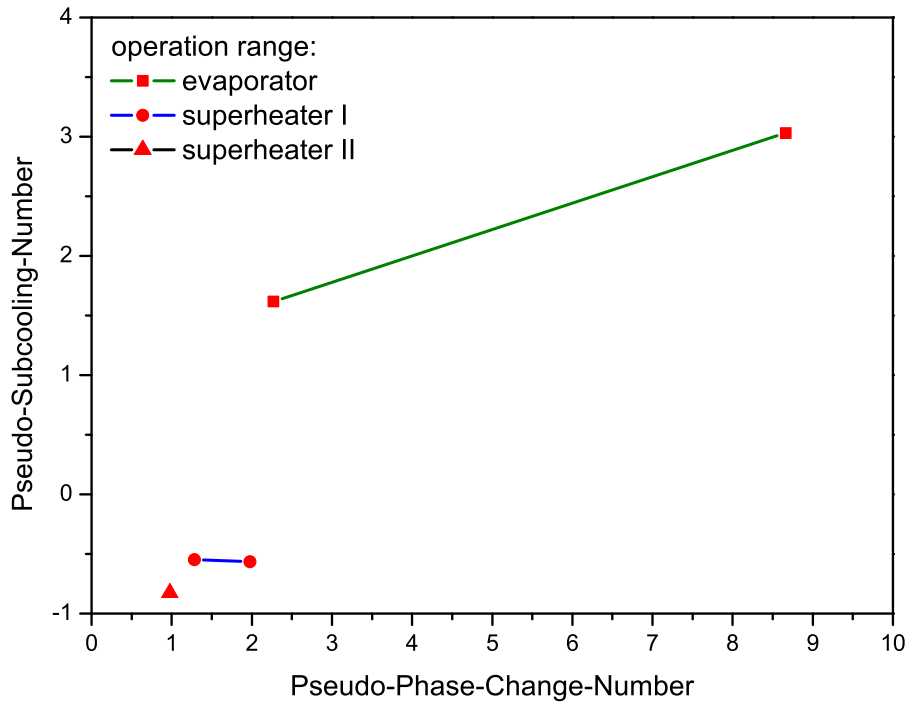
Figure 6.5: Operation range of core components in the stability map.

In Figure 6.6 the stability map is illustrated. The neutral stability boundary (NSB) is given in black, separating linearly stable operation points (left hand side of NSB) from linearly unstable operation points (right hand side of NSB). The shape of the NSB is similar to the well known shape obtained for two-phase systems (for comparison see: Figure 4.3). An asymptotic behavior of near constant exit enthalpies at large Pseudo-Subcooling-Numbers and enhanced stability at low Pseudo-Subcooling-Numbers can be observed. Note that, lower Pseudo-Subcooling-Numbers corresponds to higher inlet temperature of the fluid. By increasing the Pseudo-Phase-Change-Number, the power level is increased. Furthermore, it can be seen that while the normal operation point of the evaporator is in the linear stable region, a part of the operation range lies on the right hand side of the NSB - in the linear unstable region (green line in Figure 6.6). The consequences of this fact are discussed in Chapter-10.

Iso-decay-ratio can also be plotted in the same stability map (Figure 6.7). It is also interesting to note the effect of reference temperature on the evaluation of Eq(3.22) and thus $N_{\text{P-SUB}}$. Figure 6.8 shows a reference temperature of $T_{\text{bulk}} = 350\ ^\circ\text{C}$ (right hand side plot and abscissa in blue), while the black curve is based on $T_{\text{bulk}} = 384\ ^\circ\text{C}$, which is the pseudo-critical point at 25 MPa (abscissa in black). Since the neutral stability boundary should be independent of the reference temperature, both curves in Figure 6.8 (left hand side) differ only by an offset in the Pseudo-Subcooling-Number.
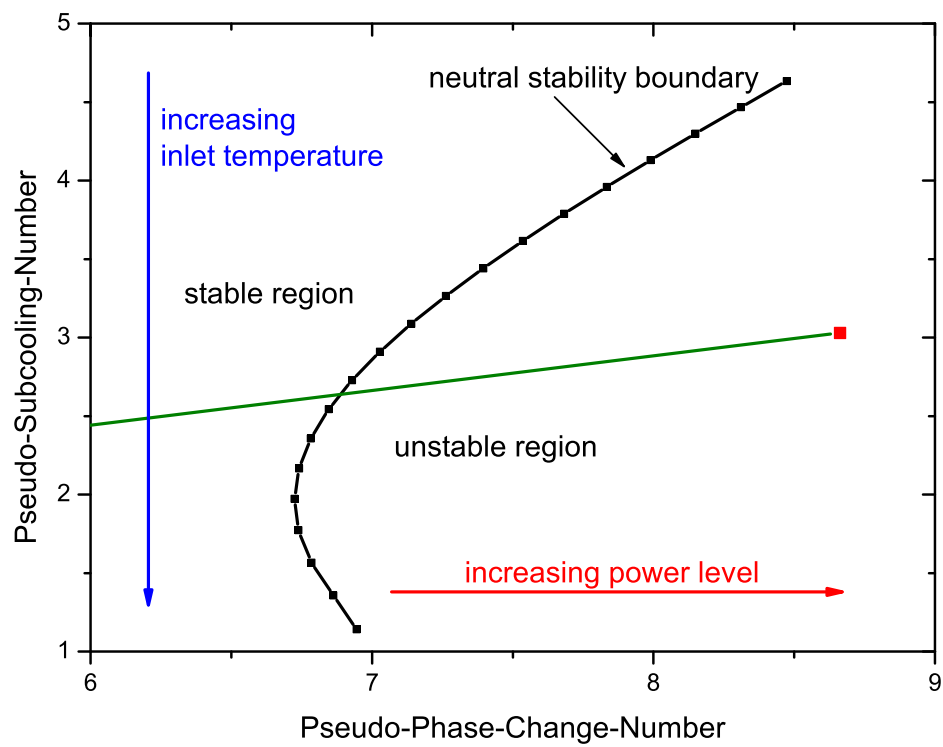
Figure 6.6: Neutral stability boundary in the $N_{\text{P-SUB}}$ vs. $N_{\text{P-PCH}}$ plane (black curve). The operation range of the evaporator is given in green.
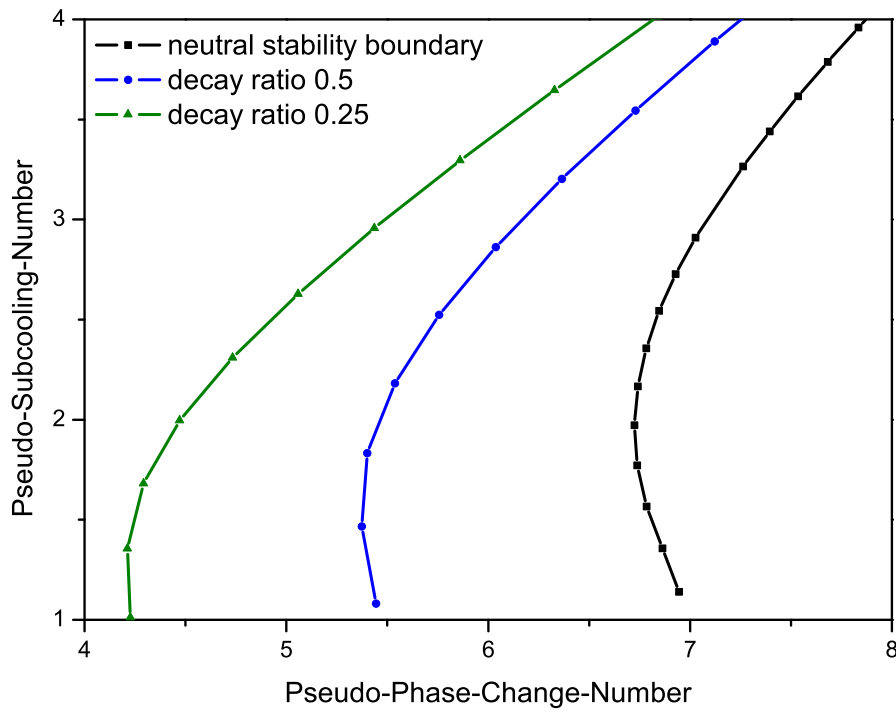
Figure 6.7: The curve of decay ratio $DR = 1$ which is equivalent to the neutral stability boundary (black curve) in the $N_{P\text{-SUB}}$ vs. $N_{P\text{-PCH}}$ plane. Furthermore, the curve of decay ratio $DR = 0.5$ and $DR = 0.25$ (blue and green curve, respectively).
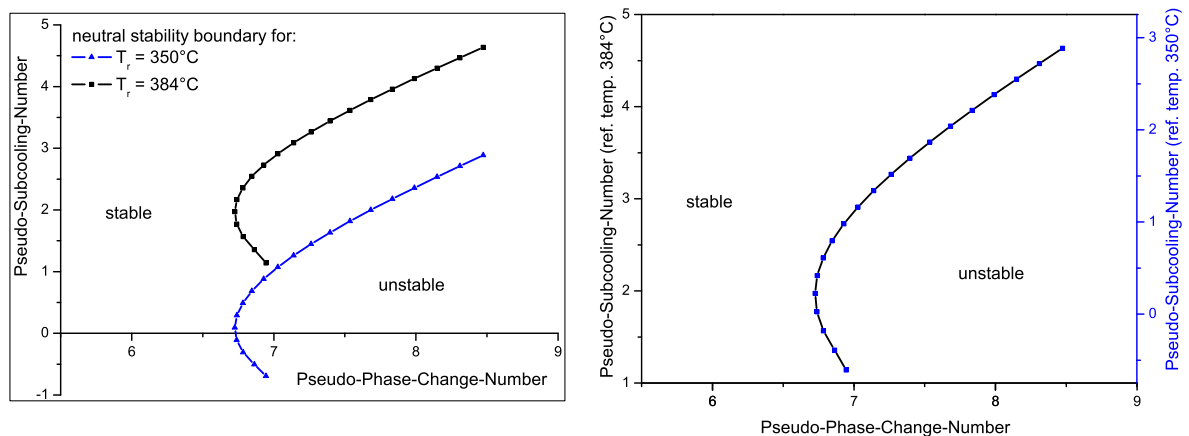


Figure 6.8: Effect of different reference temperature. The neutral stability boundary is independent of the reference temperature, both curves differ only by an offset in the Pseudo-Subcooling-Number.

## 6.5 Simplified Stability Criterion

It is interesting to note that Ishii et al. [36] developed a simplified stability criterion for two-phase systems. With this criterion the upper branch of the neutral stability boundary (big $N_{SUB}s$) in the $N_{PCH}$-$N_{SUB}$-plane is approximately parallel to a line with constant exit quality, $X_{exit}$:

$$N_{SUB} = N_{PCH} - \frac{\rho_f - \rho_g}{\rho_g} X_{exit} \quad . \tag{6.2}$$

As before, $\rho_f$ and $\rho_g$ are the saturated density for the fluid and gaseous phase, respectively.

$$X_{exit} \leq \left[ \frac{2\left(k_{in} + 2\Lambda + k_{exit}\right)}{1 + \Lambda + k_{exit}} \right] \frac{\rho_g}{\rho_f - \rho_g} \quad , \tag{6.3}$$

where $k_{in}$ and $k_{exit}$ are the inlet and the outlet loss coefficients, and $\Lambda$ is the Euler-Number (Eq(3.2)). This simplified stability criterion should be used with great caution, since it neglects effects such as drift flux, subcooled boiling, nonuniform heat flux profile and distributed local losses (e.g. spacers) and wall heat capacity, which have a well known influence on the stability limits. Nevertheless, it can be useful for a quick rough estimation of the neutral stability boundary and for an analytic check of numerical results of a homogeneous equilibrium model. For fluid at supercritical pressure condition, the simplified stability criterion is given by (Eq(6.2) into Eq(6.3))

$$N_{P\text{-}SUB} \approx N_{P\text{-}PCH} - \left[ \frac{2\left(k_{in} + 2\Lambda + k_{exit}\right)}{1 + \Lambda + k_{exit}} \right] \quad . \tag{6.4}$$

The match of this criterion (blue) with the numerically calculated neutral stability boundary (black curve) can be seen in Figure 6.9. The inlet loss coefficient was set to 5, the exit loss coefficient was set to 0.5.

## 6.6 Sensitivity on Design and Operation Parameters

The sensitivity on the threshold of instability of various design and operation parameters is analyzed in this section. The conclusion will finally be presented in Table 6.1.

### 6.6.1 Inlet and Outlet Flow Restrictions

An inlet pressure loss caused by an orifice is strongly stabilizing, as Figure 6.10 shows. This phenomenon directly corresponds to the experience made with inlet pressure losses in boiling channels. In two-phase systems the stability boundary sensitively depends on the pressure loss distribution in the region of subcooled liquid (before the boiling boundary is reached) and the region of light fluid (after passing the boiling boundary). For the case of interest here, the subcooled liquid region corresponds to the high density region before the fluid is heated beyond the pseudo-critical point. Any device which increases the pressure loss of the heavy liquid region increases the so-called in-phase pressure loss. On the contrary, the effect of a flow resistance at the channel outlet (or also called out-of-phase pressure loss) is strongly destabilizing (Figure 6.10). Strong care
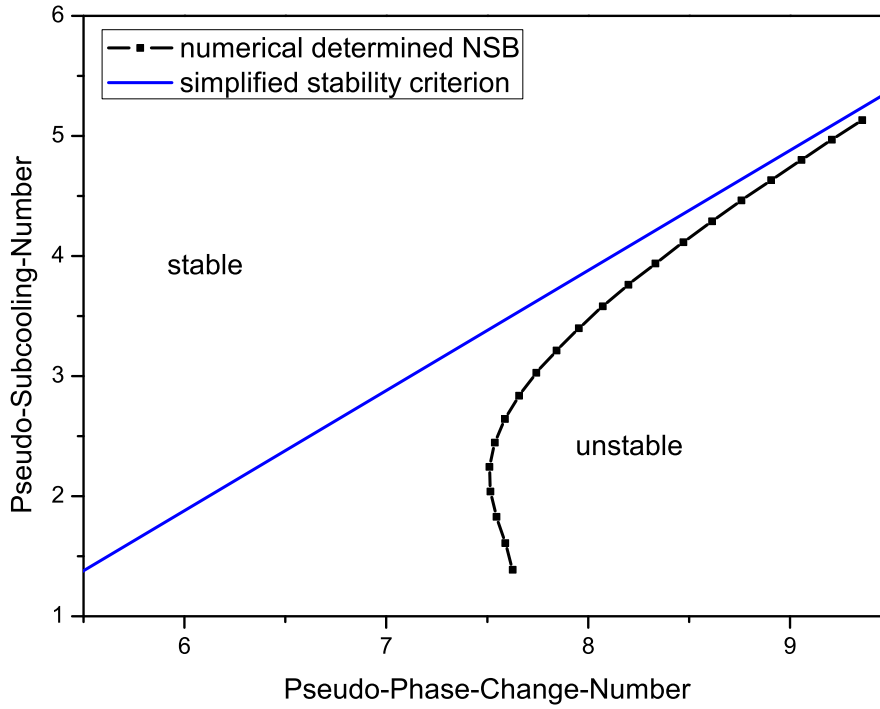
Figure 6.9: Comparison of the simplified stability criterion (blue line) to the numerically calculated neutral stability boundary (black curve; $k_{\text{in}} = 5$; $k_{\text{exit}} = 0.5$).

must be taken with pressure losses at the outlet or the upper part of the coolant channel. Pressure losses of spacers must be taken into account. Since an in-phase pressure loss is the most sensitive parameter for stabilizing a supercritical flow channel, inlet orifices can be customized to assure stable operation with respect to DWOs for otherwise unstable channels.

## 6.6.2 Heated Length

In Figure 6.11 the neutral stability boundary is shown for various heated lengths ($L_H$) in the stability map. The onset of instability is at lower Pseudo-Phase-Change-Numbers for smaller values of $L_H$ ($L_H = 2$ m: blue curve). Increasing the heated length has a stabilizing effect ($L_H = 3$ m: green; $L_H = 4$ m: brown and $L_H = 2$ m: purple). This phenomenon can be explained by the value of the friction term in the momentum equation Eq(3.17); given by

$$\text{friction term} : \Lambda G^2 v = \frac{f \, L_H}{2 D_H} \frac{G^2}{\rho} \quad . \tag{6.5}$$

Since the friction factor is approximately constant across the heated channel ($f \approx 0.033$), the Euler number $\Lambda$ is also approximately constant ($\Lambda \approx 3.1$). The same is true for the mass flux. On the other hand, the density $\rho$ changes about a factor of eight in a HPLWR core. Hence, the friction term is small in the high density region ("in-phase region"). Here, increasing the heated length has a relatively strong effect. In the low density region ("out-of-phase region") the effect is smaller, since the values of the friction term
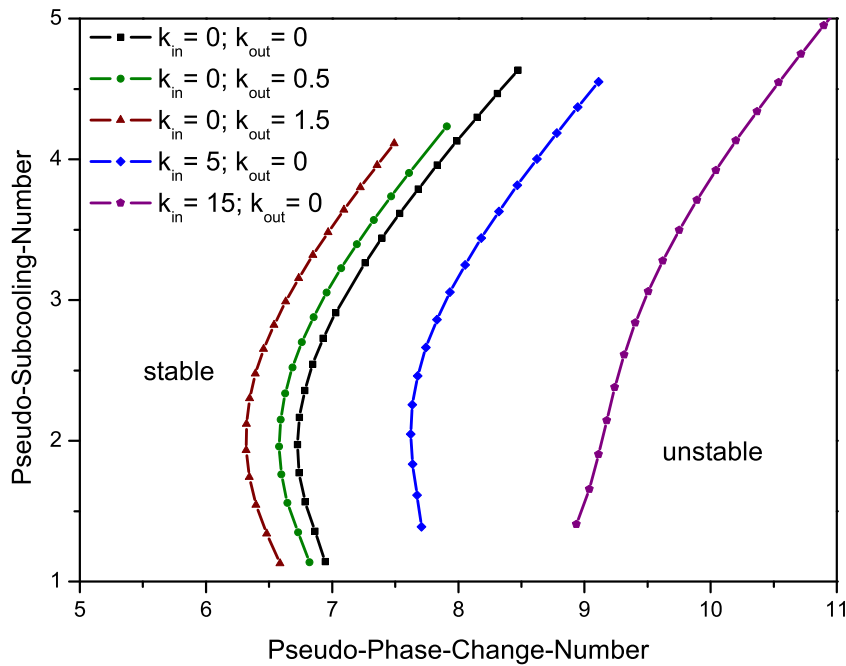
Figure 6.10: The neutral stability boundary for a supercritical flow channel with different inlet or outlet flow restriction (orifices) is shown in the $N_{\text{P-SUB}}$-$N_{\text{P-PCH}}$ plane.

become larger.

For comparison, the HPLWR has a heated length of $L_H = 4.2$ m. It is also interesting to note that the US reference design of a SCWR has an heated length of $L_H = 4.7$ m [79].

### 6.6.3 Hydraulic Diameter

Furthermore, the effect of the hydraulic diameter, $D_H$, of the coolant channel on the margins for instability is analyzed. Figure 6.12 shows the neutral stability boundary for various hydraulic diameters from $D_H = 0.002$ m to $D_H = 0.01$ m. The corresponding neutral stability boundary with a hydraulic diameter for a fuel assembly of HPLWR is given in black. Increasing the hydraulic diameter has a destabilizing effect. Again this can be explained by the impact of the hydraulic diameter on the Euler number (see Eq(6.5)). Increasing the hydraulic diameter reduces the in-phase pressure loss relatively more then the out-of phase pressure loss. It has to be noted that a typical fuel assembly of a supercritical PWR by Vogt et al. [71] and the US reference design of SCWR [45] have a hydraulic diameter of $D_H = 0.0047$ m and $D_H = 0.0024$ m, respectively.

### 6.6.4 Flow Direction

The coolant flow scheme of HPLWR, in detail the heat up in three stages, is rather complicated for a nuclear reactor. Since the coolant flows in both directions, upwards in the evaporator and the superheater II, and downwards in the superheater I, as moderator and gap water, it is interesting to know the effect of the gravitational direction on the
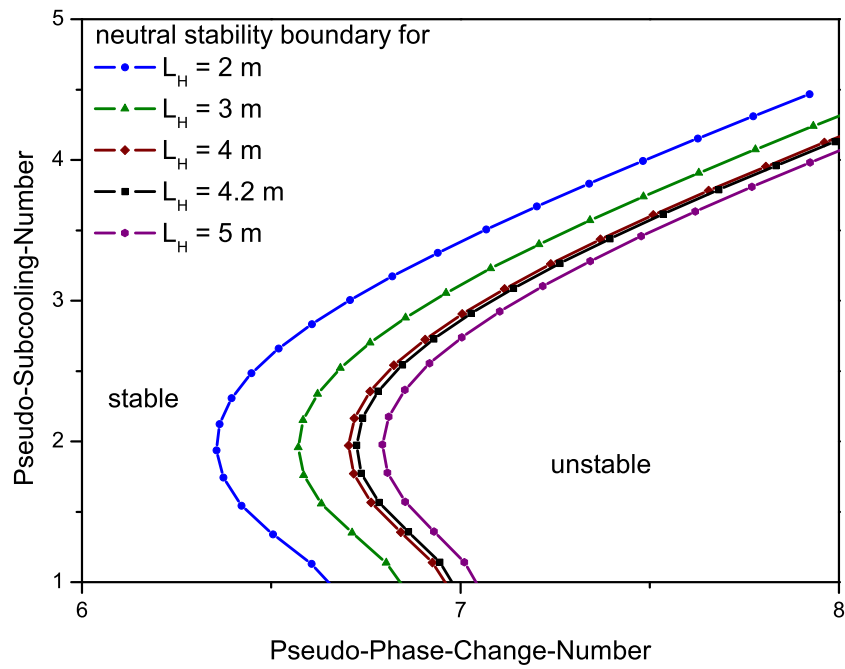
Figure 6.11: Stability map showing the neutral stability boundary for various heated lengths, $L_H$. For comparison, the HPLWR has a heated length of $L_H = 4.2$ m.
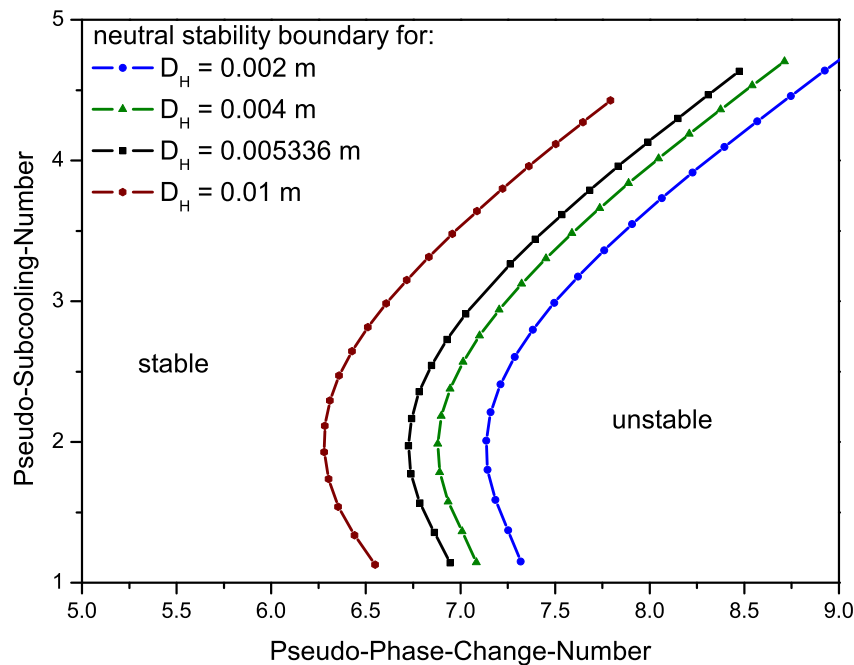


Figure 6.12: The effect of the hydraulic diameter, $D_H$, of the coolant channel on the margins for instability is shown in the $N_{P\text{-}SUB}$-$N_{P\text{-}PCH}$ plane. The neutral stability boundary for hydraulic diameter of $D_H = 0.002$ m, $D_H = 0.004$ m, $D_H = 0.005336$ m and $D_H = 0.01$ m is given in blue, green, black and brown, respectively.
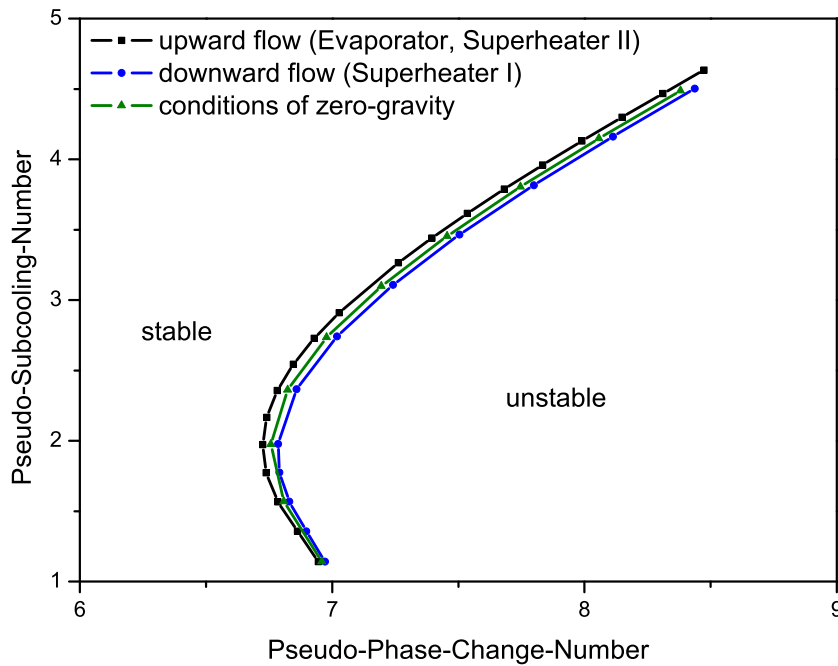
Figure 6.13: The stability plane with the neutral stability boundary was calculated for three cases: case I (in black) corresponds to a heated channel with upwards flowing coolant, conditions found for the evaporator and the superheater II. Case II (in green) represents a numerical calculation for comparison. Here, the gravitational term was set to zero (zero-gravity conditions). Case III addresses a channel with fluid flowing downwards. This case represents the superheater I.

stability. In Figure 6.13 the neutral stability boundary is shown for three identical flow channels where the gravitational acceleration was set positive (9.81 m s$^{-1}$), negative (-9.81 m s$^{-1}$) and to zero-gravity. Case I (in black) corresponds to a heated channel with coolant flowing upwards, conditions found for a fuel assembly of the evaporator and the superheater II. For comparison, case II (in green) represents a calculation where the gravitational term was set to zero (zero-gravity, space conditions). Case III addresses a channel with downward flowing fluid. This case represents the coolant flow in a fuel assembly of superheater I. Even though the hydraulic diameter and the pressure drop is different for the moderator box and gap, the comparison of parameters resulting for the sensitivity study of this chapter implies that the neutral stability boundary is very similar to the blue curve. Thus, the occurrence of unstable DWO in the moderator box and gap can be excluded since the density change in those devices is small.

## 6.6.5 Pressure Drop

The effect on stability of different pressure drops of heated channels is shown in Figure 6.14 in the $N_{P\text{-}SUB}$-$N_{P\text{-}PCH}$ plane. The neutral stability boundary is given for a pressure drop of $\Delta p = 50$ kPa, $\Delta p = 150$ kPa, $\Delta p = 250$ kPa and $\Delta p = 450$ kPa in blue, black, green and brown, respectively. The onset of instability of the lowest shown pressure drop ($\Delta p = 50$ kPa) occurs at slightly lower Pseudo-Phase-Change-Numbers
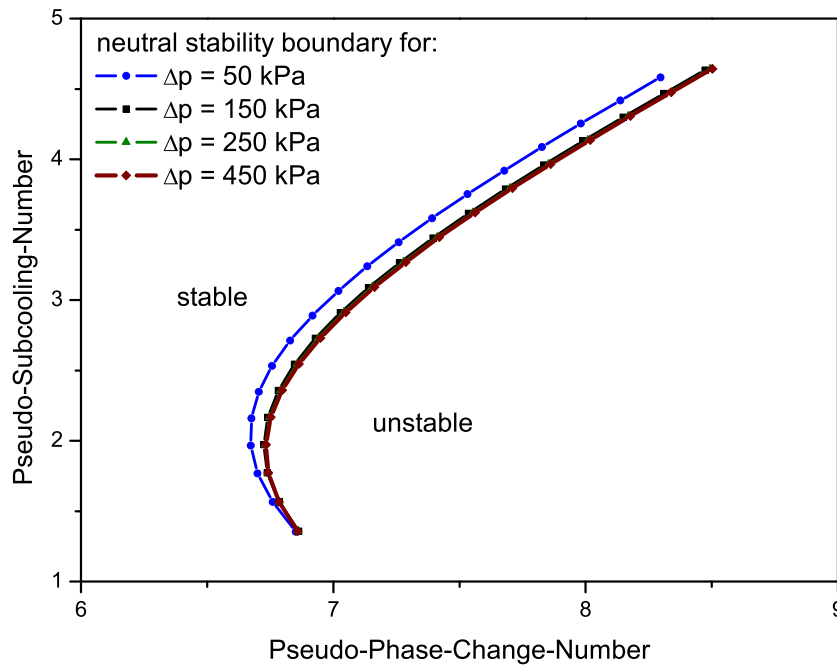
Figure 6.14: The effect of different pressure drops along the heated channel on stability is shown in the stability map ($N_{P\text{-}SUB}$ vs. $N_{P\text{-}PCH}$). The neutral stability boundary is given for a pressure drop of $\Delta p = 50$ kPa, $\Delta p = 150$ kPa, $\Delta p = 250$ kPa and $\Delta p = 450$ kPa in blue, black, green and brown, respectively. The onset for stability of the lowest shown pressure drop ($\Delta p = 50$ kPa) occurs at slightly lower $N_{P\text{-}PCH}$ for nearly the whole range of $N_{P\text{-}SUB}s$.

for nearly the whole range of Pseudo-Subcooling-Numbers. The destabilizing effect of a lower pressure drop is obvious, since it implies a lower mass flow. A lower mass flow relatively diminishes the stabilizing in-phase pressure drop in the high density region in comparison to the destabilizing out-of-phase pressure drop of the low density region. For low Pseudo-Subcooling-Numbers this effect vanishes resulting in approximately the same neutral stability boundary for all pressure drops herein. Pressure drops bigger than $\Delta p = 150$ kPa result in nearly the same stability boundary. In general, for the conditions of interest for HPLWR, the imposed pressure drop is not a very sensitive parameter for the onset of instability.

It is instructive to summarize the effect on the stability limits of the listed design and operation parameter in a table (Table 6.1). Increasing a parameter is symbolized with ↑, decreasing a parameter is illustrated with ↓. Furthermore, a variation with a stabilizing effect for a fuel assembly is visualized with ⊕, the opposite case is given by ⊖.

## 6.7 Approximated State Equation

Different approximations of the state equation of supercritical water used in previous analyses are shown in terms of specific volume vs. enthalpy in Figure 6.15. A first approximation was made by Zuber [82]. In analogy to the modeling for a boiling channel, he proposed an approximated state equation with two regions. Four decades later

Table 6.1: Effect of design and operation parameters on the stability limit of a typical FA.

| parameter | variation ↑ | variation ↓ |
|---|---|---|
| inlet pressure loss | ⊕ | ⊖ |
| exit pressure loss | ⊖ | ⊕ |
| heated length | ⊕ | ⊖ |
| hydraulic diameter | ⊖ | ⊕ |
| flow direction | ⊕ | ⊖ |
| imposed pressure drop | ⊕ | ⊖ |

a III-region model was used by Zhao [79] (indicated with a green dashed line). The approximation consists of a region with "heavy fluid" with constant density, a region of "heavy-light fluid" mixture and finally a light fluid region modeled as an ideal gas assumption. The black curve is the state equation used in this thesis. It consists of a spline function with sixty pieces fitted to the data of the water steam table (black dots in Figure 6.15). The effect of using an approximate two-region or three-region state equation which treated the supercritical fluid like a pseudo two-phase system having linear slopes can be seen in Figue-6.16. NSB are found which resemble the neutral stability boundary of two-phase systems. The used approximate (i.e., piecewise linear) equations of state lead to an overly conservative neutral stability boundary, thus overrestricting operation conditions.

## 6.8 Axial Power Distributions

The influence of the axial power distribution on the onset of the neutral stability boundary is discussed in this subsection. In previous stability calculations, a uniform power profile was assumed to analyze the underlying basic phenomena. However, in a nuclear reactor the power will never be uniformly distributed. In general, the power profile varies with burn-up. Experience from analyses of BWRs show that this has a major impact on stability. Hence, a stability analysis must take into account power profiles of different burn-up stages. At the current state of the HPLWR project, there is no axial power profile for the III-pass-core of HPWLR available. Nevertheless, some basic analysis can be done by applying standard geometric power shapes. Figure 6.18 shows five normalized axial power distributions vs. the height of the flow channel. The black line is the uniform profile. The blue curve is the cosine-shape power distribution often applied for various preliminary core analyses. In green and red the distribution for a top peak and bottom peak shape are illustrated. Further, the power distribution resulting from a coupled thermal-hydraulic/ neutronic analysis of a single pass SCWR-core is shown in purple [33]. This profile will be called the double peak profile. The resulting neutral stability boundaries can be seen in Figure 6.18. In black: the boundary for the uniform power profile. For low Pseudo-Subcooling-Numbers a cosine shape has a stabilizing effect. This agrees with experiences made in stability calculations of boiling flow. The neutral stability boundary at highest Pseudo-Phase-Change-Numbers corresponds to a top peak power profile (green curve). A top peak shape increases the high density region, thus the integral in-phase pressure loss, of the heated channel in the same way as the low density region is diminished. Hence, a top-peak has a strong stabilizing impact on a supercritical
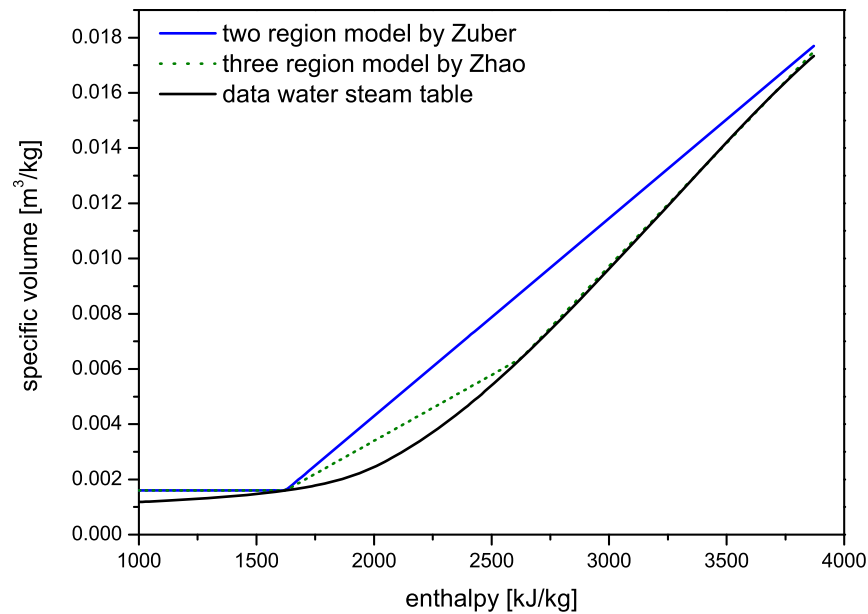
Figure 6.15: Different approximations of the state equation for supercritical water are shown in terms of specific volume vs. enthalpy. In blue, the two region model proposed by Zuber. A III-region model is indicated with a green dashed line. The data of the water steam table is given in black.
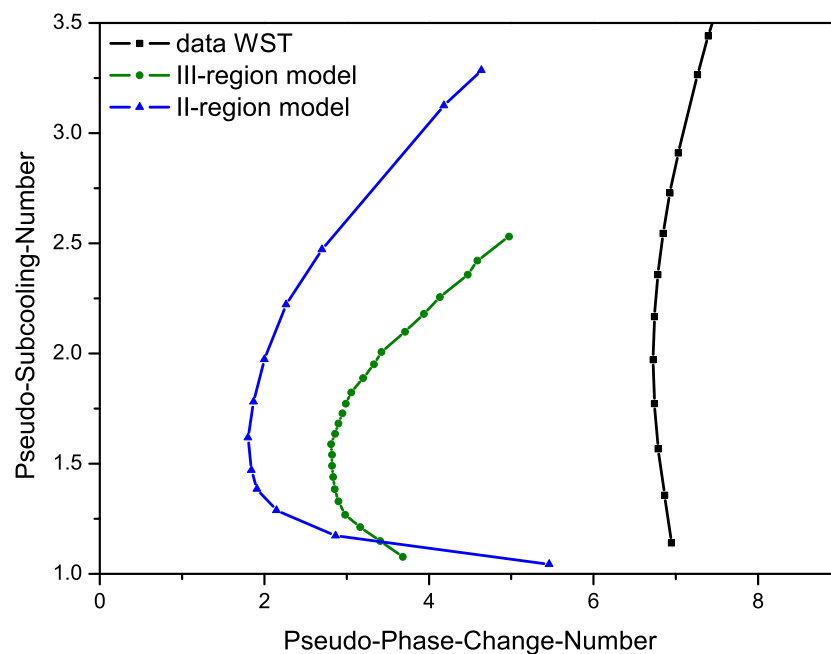


Figure 6.16: Resulting neutral stability boundary for different equation of states: II-region model in in blue; III-region model in green. For the black curve the state equation was derived out of date of the water seam table.
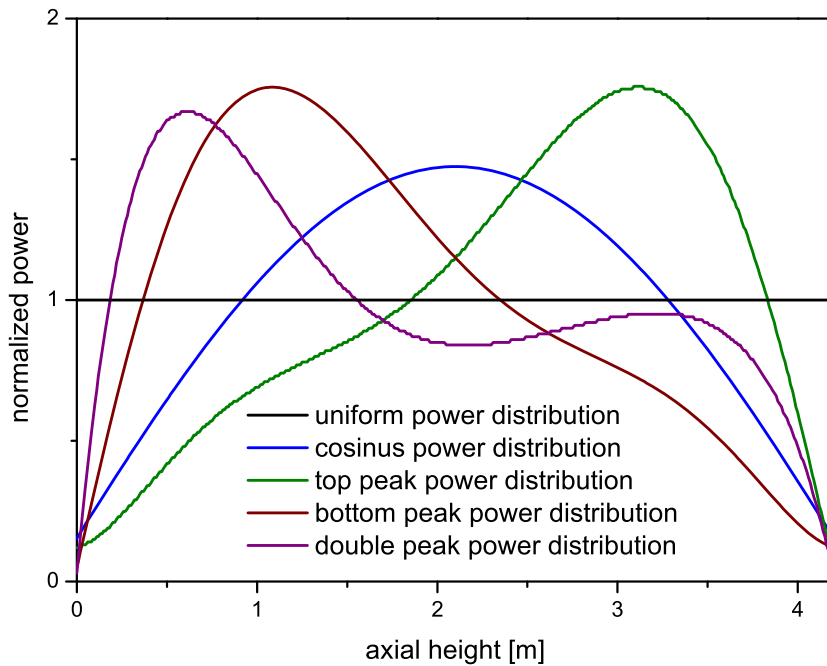
Figure 6.17: The normalized axial power distribution vs. the height of active length is shown. The black line is the uniform heat-up. A cosine-shape power distribution often applied for various preliminary core analyses (blue curve). In green and red the distribution for a top peak and bottom peak shape is illustrated. Further, a double peak power distribution is shown in purple.

flow channel. In contrary, a bottom peak power distribution increases the out-of phase pressure loss in the upper part of the flow channel leading to neutral stability boundary at remarkable lower Pseudo-Phase-Change-Numbers (red curve). The stability boundary of the double peak profile is situated in the range of the bottom peak profile since the first peak far more developed. For high Pseudo-Subcooling-Numbers, the second peak has a stronger stabilizing effect on the stability limits in comparison to the effect at lower Pseudo-Subcooling-Numbers (Figure 6.17).
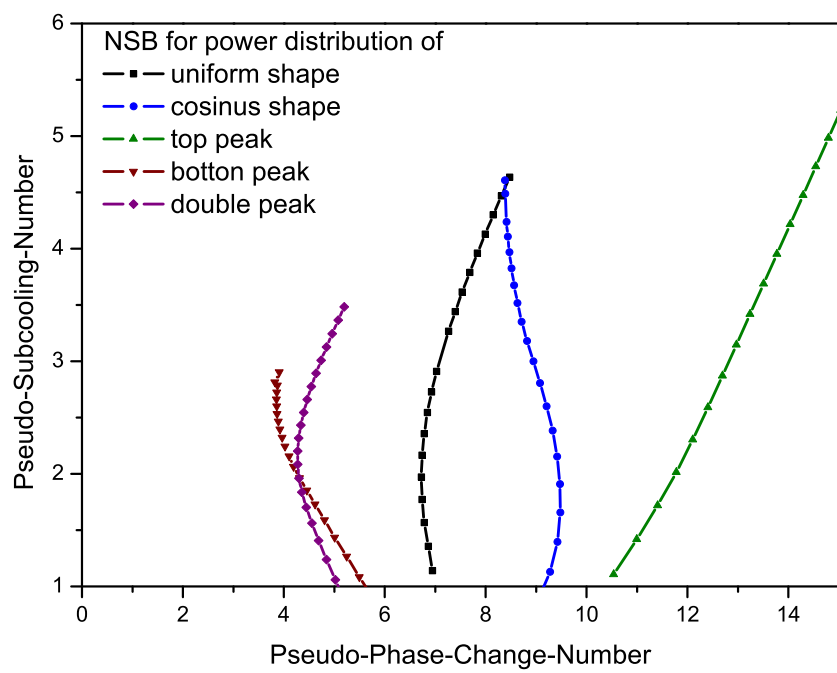
Figure 6.18: Neutral stability boundary for different power profiles: uniform distribution (black curve), cosine-shape in blue; top, bottom and double peak in green, red, and purple, respectively.

# 7 Non-Linear Dynamics

Nonlinear dynamics of the coolant flow in nuclear reactors is somehow the miscarriage in the community of nuclear engineers. Nevertheless, during the operation of BWRs nuclear engineers were confronted with unexpected instability events in various plants (e.g. Caorso (1984) and LaSalle (1988)). In both reactors the transition from a stable operation point to rapidly growing power oscillations were observed. In Spain two BWR plants have experienced unstable nonlinear oscillations that required operational suppression. This demonstrates that basic knowledge of nonlinear dynamics is needed. In particular, the bifurcation branches of the thermal-hydraulic system in a nuclear reactor should be characterized.

## 7.1 Limit Cycle

Stability experiments in a nuclear reactor showed that a stable limit cycle can exist even when the operation point is in the linear unstable region [5]. This effect can only be explained by nonlinear theory. Call Chapter 6, where it was shown that the coolant flow in the fuel assemblies become linear unstable when the parameter N (i.e. $N_{\text{P-PCH}}$) is increased above the critical value $N_c$, where the neutral stability boundary is passed. In the linear stable region ($N_c > N$) a small perturbation is damped until the system returns to normal operation conditions (left hand side of Figure 7.1; $\Delta p = 150\,\text{kPa}$, $T_{\text{in}} = 310\,°\text{C}$). Here, a uniformly heated flow channel under supercritical pressure conditions represented by the Eqs(2.25), (2.41) and (2.51) is disturbed in its basic state by a small step in power level. In the linear unstable region ($N_c < N$) a small amplitude perturbation initially grows exponentially (right hand side of Figure 7.1; $\Delta p = 150$ kPa, $T_{\text{in}} = 310$ °C). However, when the amplitude increases the oscillation reaches a stable limit of maximum amplitude. This solution of the non-linear equation system is called limit cycle. Dynamic non-linear solutions are called attractor. The transition from a linear unstable behavior to a nonlinear stable limit cycle is shown in Figure 7.2 ($\Delta p = 150$ kPa, $T_{\text{in}} = 310$ °C). The solution is attractive even if the initial oscillation of a perturbation exceeds the maximum amplitude of the limit cycle. This means, at a certain value $N_c$ for both small and large-amplitude oscillations the phase plane trajectories (i.e., solution traces) converge to the same stable limit cycle. In general, the transient can be divided into three regions. Starting from the steady-state (or basic state), initially a region of exponential growth in maximum amplitude can be found. Then, the behavior changes and a transition to a saturated state can be observed. The third region is the non-linear saturated state. This saturated state can be illustrated in a phase diagram. In Figure 7.3 the phase diagram is given in terms of mass flux vs. exit enthalpy. A limit cycle can clearly be seen in the linearly unstable region.
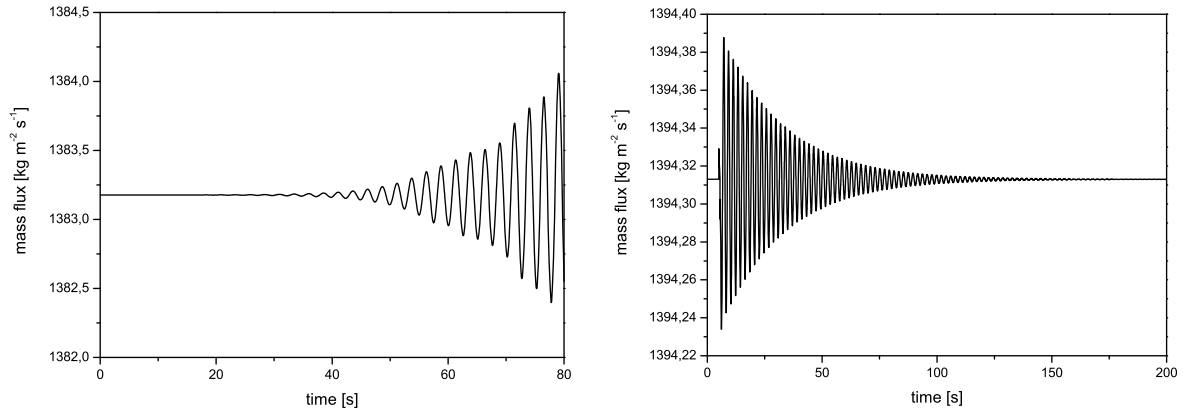
Figure 7.1: Initially system response (mass flux vs. time) due to a small perturbation of power level.
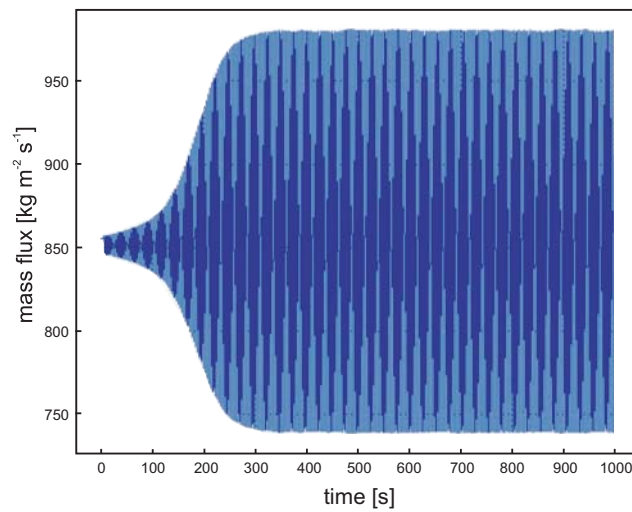


Figure 7.2: Transient of mass flux perturbation until a limit cycle is reached.
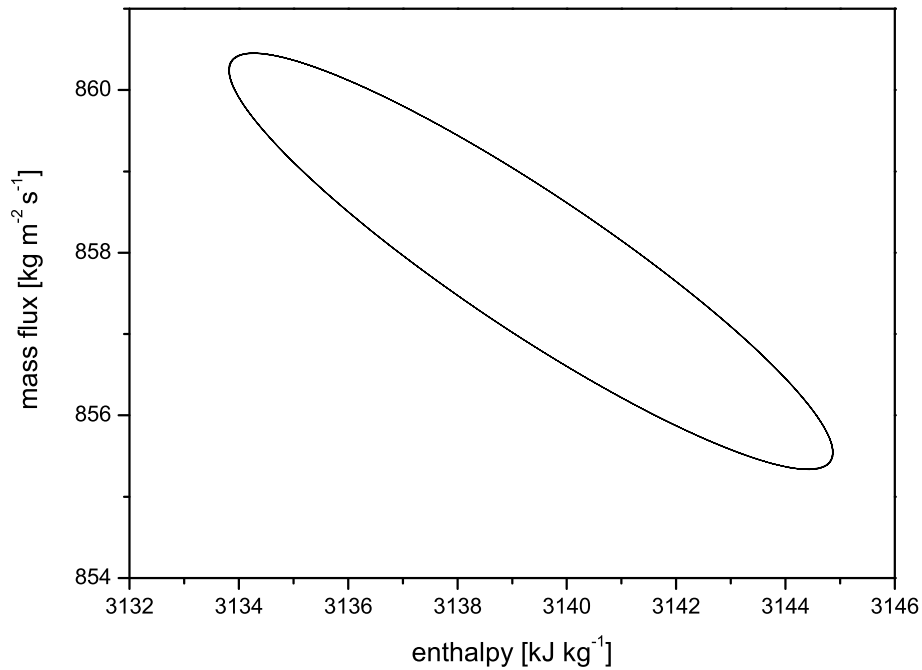
Figure 7.3: Phase diagram: mass flux vs. exit enthalpy. A limit cycle can clearly be seen in the linearly unstable region.

## 7.2 Bifurcation

For BWRs the limit cycle amplitude is a function of N and increases as N is growing, resulting in the Hopf bifurcation diagram 7.4 [40]. For $N_c<$ N the steady-state solution $(X_1 = X_2 = 0)$ is stable. Depending on whether non-linear solution exists for $N_c>$ N or $N_c>$ N a super critical or subcritical bifurcation is found, respectively. The branch with $N_c<$ N is called the supercritical bifurcation branch. For values ($N_c<$ N) a subcritical bifurcation branch can exists (left in Figure 7.4). Separated by the finite value of an unstable limit cycle, there are two basins of attraction, such that the phase-plane trajectories either converge to the negative $N_c$ axis, for small-amplitude perturbations, or diverge exponentially if the perturbation is large enough in amplitude. For a BWR this is a quite dangerous situation since classical linear methodology like frequency domain analysis would indicate a stable operation point. In particular, close to the linear stability boundary the basin of attraction of the steady-state operation point becomes significantly small. Here, a small perturbation (e.g. noise or control rod movement) could result in a growing and undamped system response.

The calculations of the nonlinear-dynamic effects can only be done by paying rather big computational costs. For comparison: the data for a typically linear stability map presented in Chapter 6 is computed with COMSOL in approximately one hour; a limit cycle, which results in a single point of a bifurcation diagram, is computed in three or four days. Nevertheless, it is necessary to investigate the potential of the non-linear dynamics to verify the linear stability analysis in frequency domain, since this method only identify the linear stability limits.
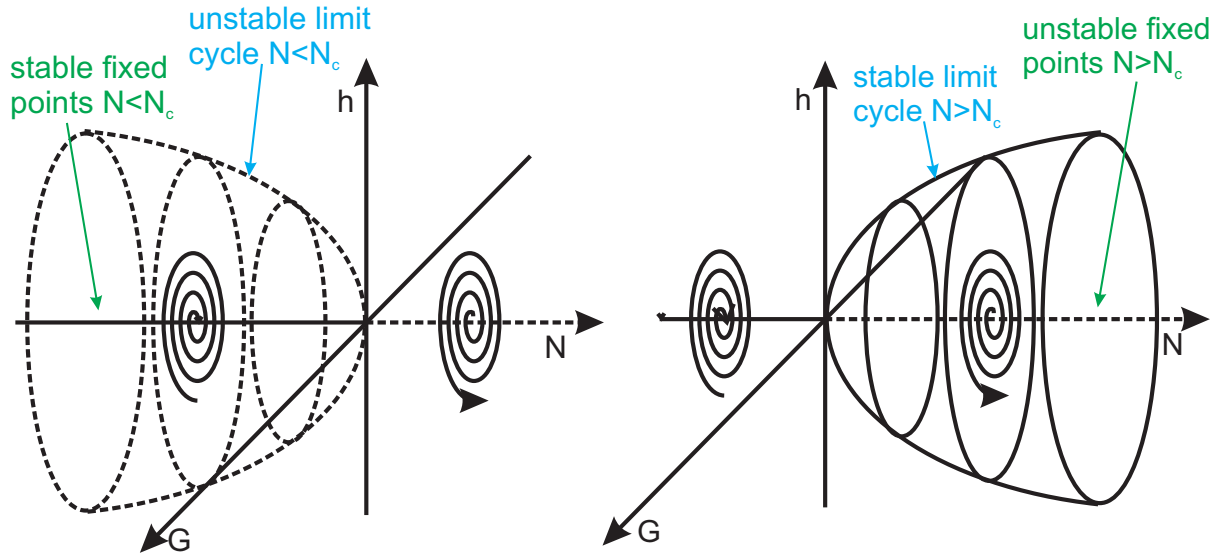
Figure 7.4: Scheme of bifurcation diagram for two-phase flow, left: subcritical Hopf bifurcation, right: supercritical Hopf bifurcation.

Not that in the case of a supercritical Hopf bifurcation the limit cycle amplitude initially increases with increasing N. At a certain second critical value of N, the amplitude of the limit cycle can become unstable resulting in a new limit cycle with a doubled period [40]. Increasing N further results in more period doubling and a so-called cascade is observed.

## 7.3 Delayed Bifurcation Diagram for Supercritical Water

The supercritical branch of the bifurcation diagram is evaluated using the linear stability boundary as the starting point. As above, a parallel channel boundary condition (pressure drop = 150 kPa) is assumed and a uniform axial heat flux is applied, so that the operation is in the unstable region of the linear stability map. Then, the steady-state condition of the flow channel is perturbed by a small step in heat flux. The resulting limit cycle includes the information of the maximum and minimum amplitude of the non-linear stable oscillation. Choosing various power levels, N, the so-called bifurcation diagram for a heated flow channel with supercritical pressure water can be determined (see Figure 7.5, where $N_c$ is the power level at neutral stability).

Starting at the point of neutral stability (i.e., the origin) a delayed bifurcation at a certain distance from $N_c$ can be seen (blue curve). The amplitudes of the limit cycles are small. This implies that the non-linear system is "stable" even when operating in the region of linear instability. As the power level is further increased a mixed supercritical bifurcation is reached whose main attractor has a relatively large limit cycle (in particular: black curve in Figure 7.5) which increases in amplitude as the power level increases (Figure 7.6). In detail, a period doubling can be observed.

Interestingly, it can be seen in Figure 7.5 that if the power level is decreased, a new attractor can be reached (green), having a limit cycle of smaller amplitude than on
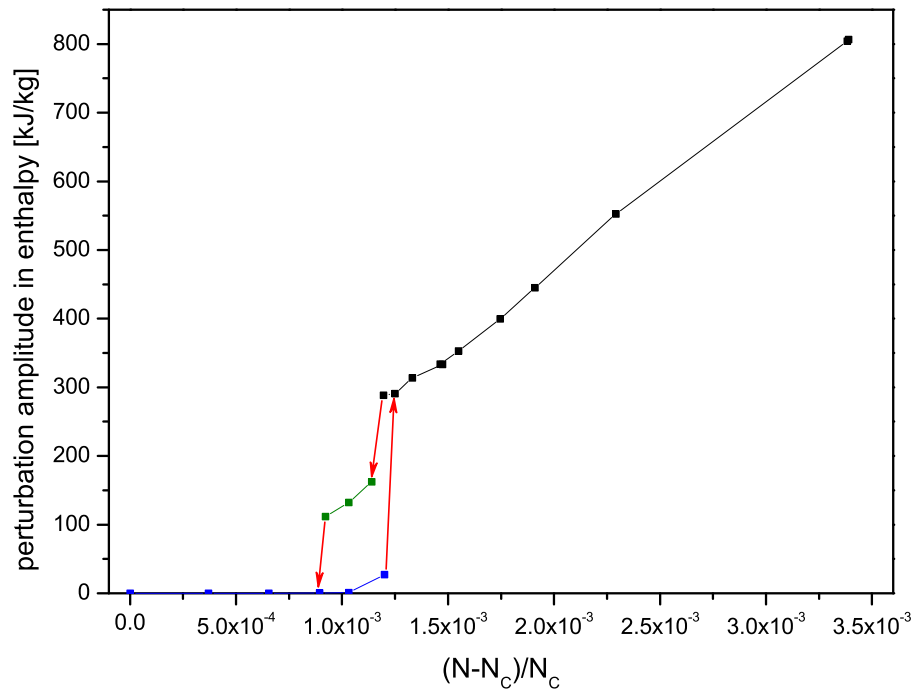
Figure 7.5: Supercritical delayed bifurcation diagram for a flow channel with water at supercritical pressure conditions.

the main attractor and significant hysteresis is experienced. That is, the onset and termination of these limit cycles is at different values of $N - N_c$.

No instability phenomena are expected below the primary bifurcation which is governed by linear theory. Even though the supercritical bifurcation shows that stable non-linear limit cycles (with finite maximum amplitude in oscillation) exist close to the neutral stability boundary, the whole operation range of the HPLWR core components should be in the linear stable region, since oscillation amplitudes become large.
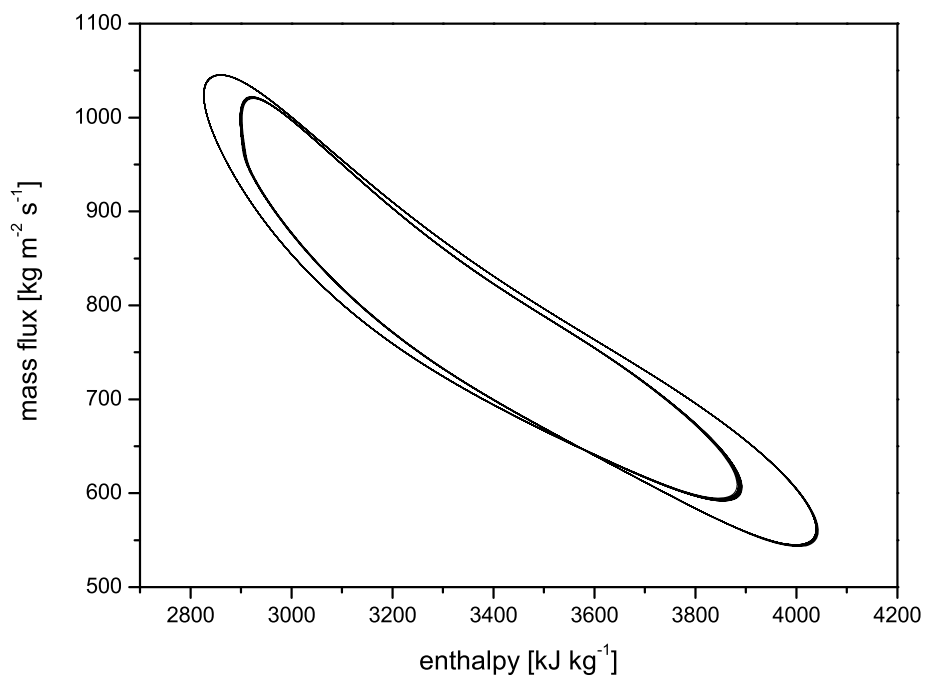
Figure 7.6: Phase diagram mass flux vs. exit enthalpy. For the upper branch of the delayed bifurcation diagram a period doubling for the limit cycle can be observed.

# 8 Multi-Channel Analysis

In the current HPLWR design proposal, nine fuel assemblies are grouped to form one fuel assembly cluster. At the bottom of each fuel assembly cluster a diffuser is located distributing the coolant from the lower plenum into the fuel assemblies (Figure 8.1). This configuration represents an array of parallel flow channels coupled by a common plenum at the inlet. At the outlet of the fuel assemblies also a common exit plenum is situated. In order to investigate the various DWO stability characteristics of the HPLWR fuel assembly cluster, various configurations of parallel identical channel arrays will be analyzed. The thermal-hydraulic model (Eqs(2.52), (2.53), (2.54), and (2.55)) derived for the single channel case is expanded:

$$\frac{\partial h_i}{\partial t} = v_i^2 \left( \frac{\partial v_i}{\partial h_i} \right)^{-1} \frac{\partial G_i}{\partial z} \tag{8.1}$$

$$\frac{\partial G_i}{\partial t} = -\frac{\partial p_{d,i}}{\partial z} - \frac{g_{\text{eff}}}{v_i} + \Lambda \frac{G_i^2 v_i}{2} \tag{8.2}$$

$$\frac{\partial h_i}{\partial t} = \frac{G_i}{v_i} \frac{\partial h_i}{\partial z} - v_i \frac{q''_i P_H}{A_{x-s}} \tag{8.3}$$

$$\rho_i = \rho_i(h_i) = \frac{1}{v_i} \quad , \tag{8.4}$$

which is a coupled set of equations for each channel $i$ in the parallel array with total number of channels $j$ ($i = 1, 2, 3..., j$). The coolant flow is adiabatic in the inlet plenum. Evidently, the total mass flux, $G_{\text{tot}}$, of the array is the sum of the mass fluxes of $i$ channels:

$$G_{\text{tot}} = \sum_{i=1}^{j} G_i \quad . \tag{8.5}$$

The pressure loss, $\Delta p_{\text{plenum}}$, of the lower plenum can be implemented in the boundary conditions of the equation system

$$\Delta p_{\text{plenum}} = \frac{K_{\text{plenum}}}{2} \sum_{i=1}^{j} \frac{G_i}{v_{\text{inlet}}} \quad , \tag{8.6}$$

where the pressure loss coefficient $K_{\text{plenum}}$ can be chosen conveniently to achieve the plenums pressure loss $\Delta p_{\text{plenum}}$.
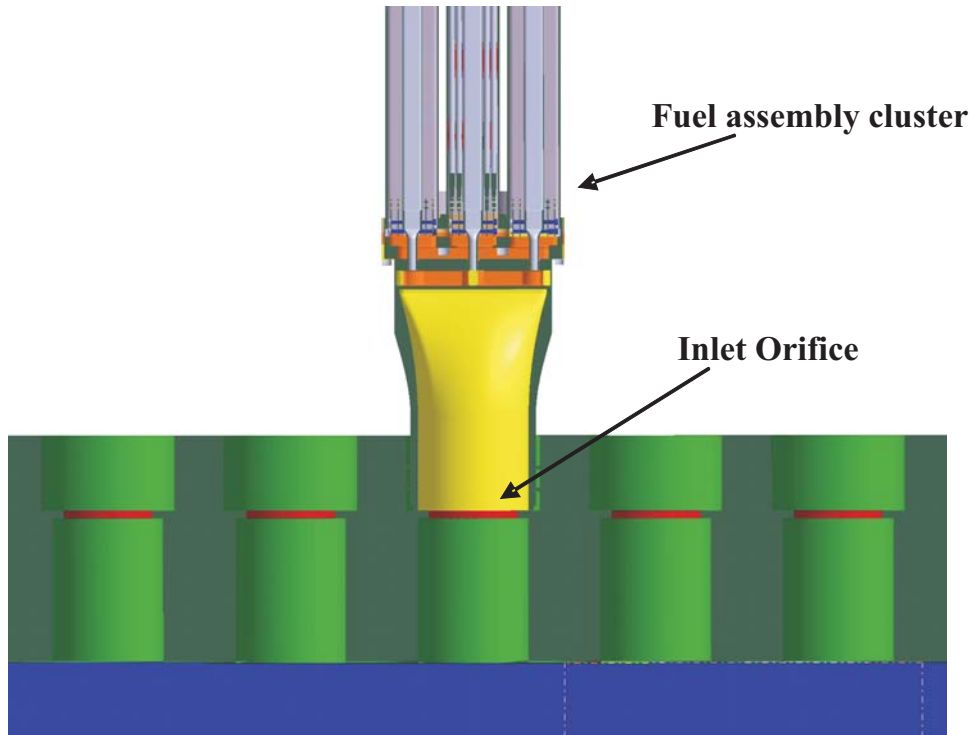
Figure 8.1: Cut trough a foot piece of one HPLWR fuel assembly cluster and the core support plate (green). An orifice (red) at the entrance of the diffuser (yellow) determines the total coolant flow of the fuel assembly cluster.

## 8.1  Twin-Tube Configuration

An array of two coupled identical flow channels is investigated. This at first glance rather simple configuration is of great importance for nuclear reactor applications. Under certain operational parameters fuel assemblies of extended core regions behave as a single thermal-hydraulic unit. The situation when half of the core oscillates with a 180° shift with respect to the other half is referred to as core-wide out-of-phase oscillation. For the HPLWR the following out-of-phase oscillation types should be considered:

- core-region-wide out-of-phase oscillation of the evaporator,

- core-region-wide out-of-phase oscillation of the superheater-I and superheater-II,

- a local out-of-phase oscillation of a few fuel assemblies up to one fuel assembly cluster.

The first type is similar to the core-wide out-of-phase oscillation of BWRs (e.g. [37]). The understanding of the first and the second type (for completeness called core-region-wide) necessitates neutronic considerations since the fluctuation in average fluid density of the oscillating core halves influences the moderation ability (see Chapter 9). The last type is a neutronically decoupled case analyzed in this chapter.

First, a linear stability analysis is performed, which results in an eigenvalue spectrum
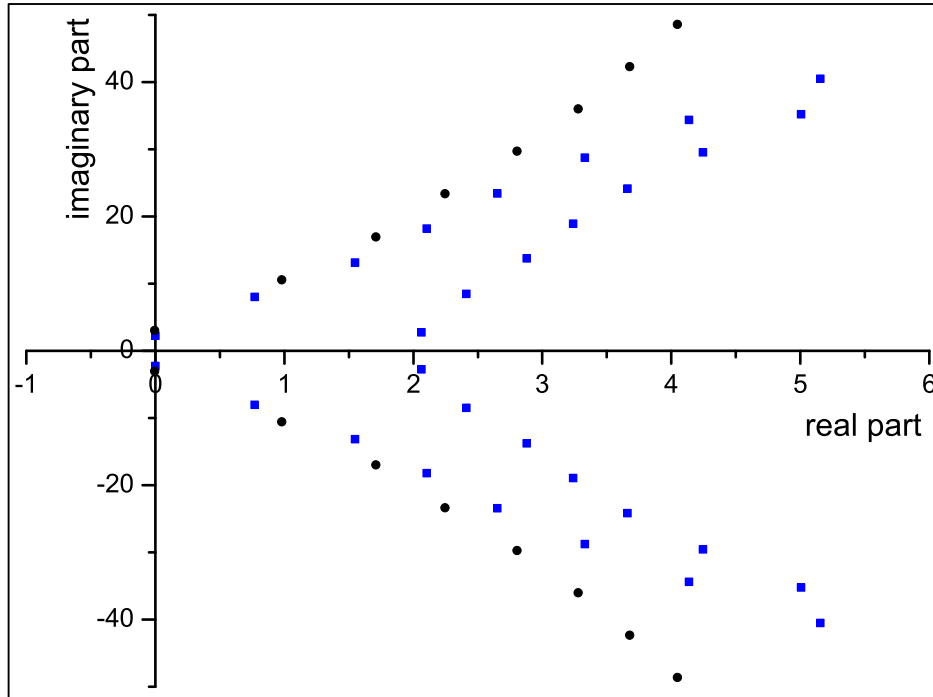
Figure 8.2: Eigenvalue spectra for a single channel (black) and two coupled channels (blue).

for each channel power. In Figure 8.2 the spectrum of a single channel (black) is compared to the spectrum of two coupled channels, where one channels power is high while the other channel is at average power level (blue). Both thermal-hydraulic systems operate at their stability threshold (for $K_{in} = 20$; inlet temperature $T_{in} = 280$ °C). The spectrum of two channels is quite similar to the spectrum of the single channel. For the case of two coupled channels, one can clearly distinguish the eigenvalue branches of hot and average power levels. The hottest channel always defines the leading mode.

Next, the thermal-hydraulic model is evaluated in the time domain. Again, a parallel channel boundary condition (pressure drop $\Delta p = 150$ kPa) is assumed. Furthermore, in both channels a uniform axial heat flux is chosen that corresponds to the stable region of the linear stability map. Then, the steady-state solution of the channel is perturbed with a heat flux perturbation. A typical system response, in this case for the exit enthalpy, of both channels is shown in Figure 8.3. Obviously, for the conditions shown, the induced oscillations have a 180° phase shift (i.e. out-of-phase oscillation).

The neutral stability boundary is calculated for two cases. In the first case, one channel is at the average power level, which is representative for HPLWR conditions ($q'' = 6.2 * 10^5$ W/m$^2$), while the other channels power level was increased until neutral stability is reached. In the second case, the power level of both channels is identical and increased until the thermal-hydraulic system reaches the neutral stability boundary.

For the first case (green), it can be seen in Figure 8.4 that the average power channel has a stabilizing effect on the parallel hot channel. Moreover, there is a mitigating effect of the common inlet orifice. However, this effect is not as strong as the same in-phase pressure loss for a single channel. That is, using an inlet orifice with same pressure
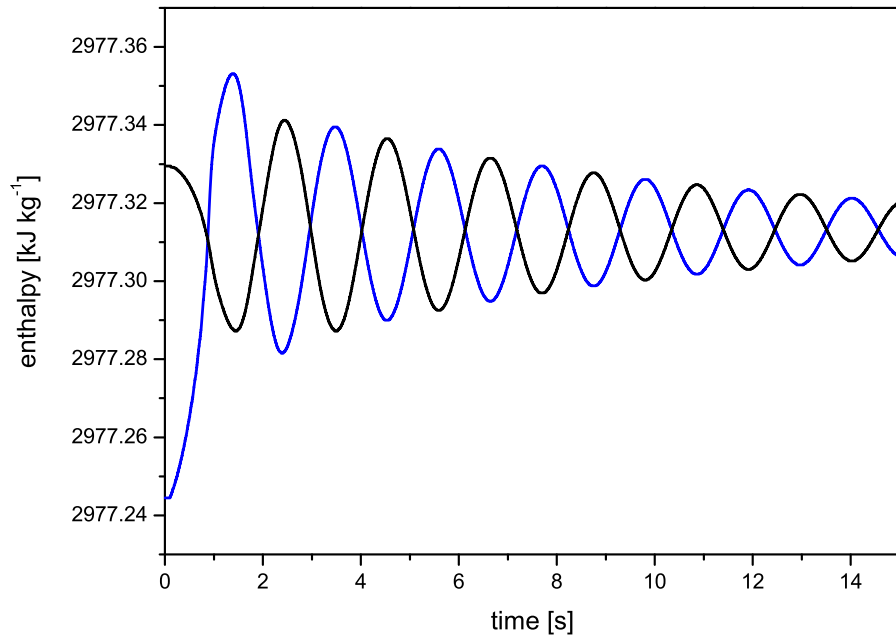
Figure 8.3: System response of exit enthalpy in the linear stable region.
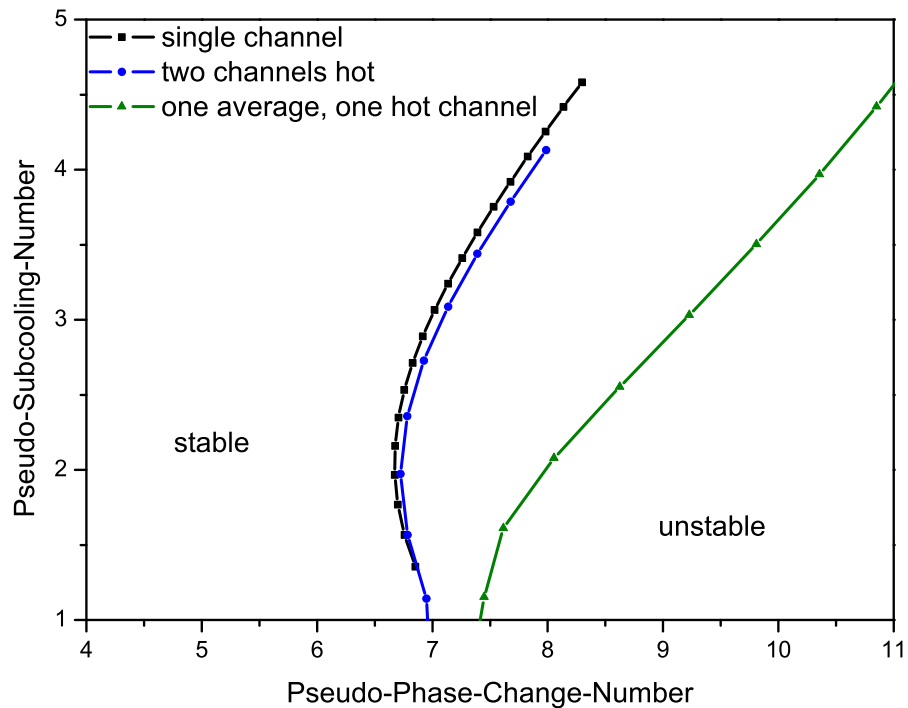


Figure 8.4: Neutral stability boundary for two hydraulically identical coupled channels. Green: one channel stays at average power level, the other is hot. Blue: both channels are hot. For comparison, black: single channel without any inlet or exit losses.
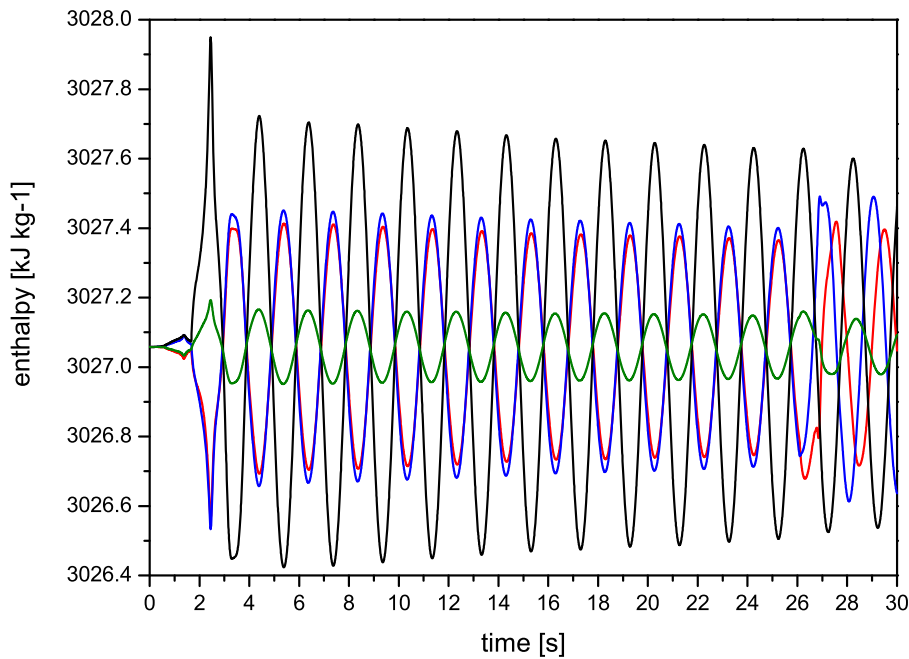
Figure 8.5: Transient of four coupled channels after a small perturbation of power level.

loss for a single channel would result in a Pseudo-Phase-Change-Number of more than 15 at the neutral stability boundary (Figure 6.10). The second case (both channels, blue) displays a more critical operational condition with respect to thermal-hydraulic instabilities, because there is little in-phase pressure loss induced by the common inlet orifice. For comparison, the linear stability limit of a single channel without inlet nor exit losses is shown in Figure 8.4.

## 8.2 Non-Linear Dynamics in Parallel Channel Arrays

The time domain system response can be rather complicated in the parameter range of hysteresis of the delayed supercritical bifurcation (Chapter 7.3). In Figure 8.5 the transient response of an array of four channels is plotted. The first oscillations are not harmonic until the system reaches an "asymptotic response", where the magnitude of oscillation in the hottest channel is still decreasing while the average channels are increasing in amplitude.

## 8.3 HPLWR Fuel Assembly Cluster

An array of nine parallel flow channels represents a typical HPLWR fuel assembly cluster. The system response due to a small perturbation in power level is investigated in the time domain. In general it can be seen that the channel with the highest power level also has the largest magnitude of oscillation. In Figure 8.6 the transient is shown in the linear unstable region in terms of relative exit enthalpy perturbation (in particular
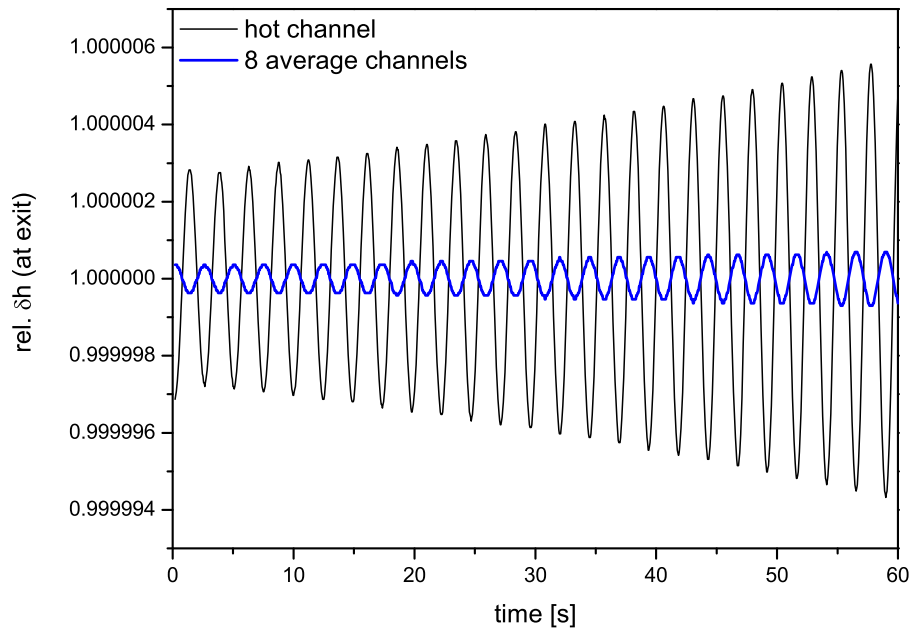
Figure 8.6: Transient of exit-enthalpy in the linear unstable region for a typical HPLWR fuel assembly cluster.

$\Delta p = 150$ kPa, $T_{in} = 310$ °C). The highest power channel oscillates out-of-phase to the other 8 averagely heated channels. The sum of magnitudes of oscillation by the 8 averagely heated channels corresponds to the maximum amplitude of the hot channel. The neutral stability boundary is calculated for various in-phase pressure losses (i.e. 0 kPa -70 kPa) for various modes of heating: e.g. eight channels at average power level, which is representative for HPLWR conditions, while the power level of one channel is increased until neutral stability is reached. Finally, the power level of all channels is set to identical value and is increased until the thermal-hydraulic system becomes unstable. Some of the resulting neutral stability boundaries are shown in Figure 8.7 in the Pseudo-Phase-Change-Number/ Pseudo-Subcooling-Number plane. It can bee seen that a common inlet orifice before the intermediate lower plenum (diffuser) has almost no stabilizing effect on arrays of nine parallel channels since the onset of instability is almost the same as for a single channel without inlet or exit orifices.

## 8.4 Conclusions of Multi-Channel Analysis

An in-phase pressure loss in a common intermediate lower plenum induced by an inlet orifice has almost no effect on the onset of density-wave oscillation in arrays of parallel channels with supercritical water. In order to avoid the discussed instability modes in the critical heat-up stages of a HPLWR three pass core, additional inlet orifices for every single fuel assembly are needed. This type of arrangement is similar to the one used in deployed boiling water nuclear reactors (BWRs).
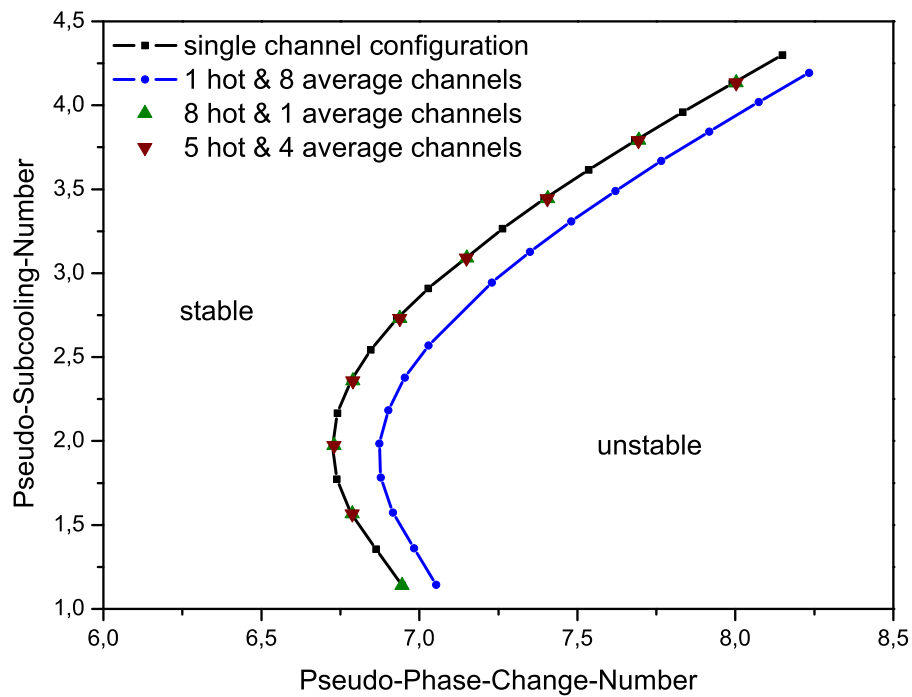
Figure 8.7: Neutral stability boundaries of various DWO modes in a typical HPLWR fuel assembly cluster. Eight channels are at average power level while one channel's power level was increased until neutral stability (blue); the contrary case, one channel is at the average power level while eight channels' power level is increased (green dots); four channels at average power level while five channels are hot (red dots).

# 9 Coupled Thermal-Hydraulic/ Neutronic Analysis

In previous chapters, density wave oscillations were analyzed as thermal-hydraulic flow instabilities, when the power generation in the fuel is assumed to be constant in time. However, this is only true for the case where DWOs appear in a single fuel assembly while all other fuel assemblies stay in steady-state condition.

In a nuclear reactor, power generation occurs via fission of heavy elements - most likely uranium - into lighter elements of the fuel. Figure 9.1 shows a scheme of the chain reaction in a thermal reactor. During the fission of U-235, neutrons with high velocity are released. The probability of absorption of fast neutrons by a uranium atom is rather low. To maintain the chain reaction, the fast neutrons must be slowed down by the moderator. Slow (or thermal) neutrons have a high probability of inducing a new fission process. The fission rate, and therefore the power generation, is directly correlated with the thermal neutron flux and fission cross-section of the fuel. The neutron flux is correlated to the moderation ability of the fluid via its density. Thus, if the density of the fluid fluctuates in a large amount of fuel assemblies due to DWOs, coupled thermal-hydraulic/ neutronic considerations are necessary. A coupled thermal-hydraulic/ neutronic analysis involves:

- a model of the neutron dynamics, which determines the power generated by the fuel,

- a model for the fuel dynamics, which takes into account that the probability of absorption for thermal neutrons correlates with fuel temperature,

- a heat transfer model, which defines the heat flux from the fuel to the fluid,

- a thermal hydraulic model, which characterizes the fluid density distribution due to changes in heat flux.

## 9.1 Reactivity Instability Types

Coupled thermal-hydraulic/ neutronic instabilities - also referred to as reactivity instability - can be divided into two types.

The first type is the so-called in-phase oscillation. For this type of instability, the whole unstable region of a nuclear core behaves as one unit. Such an unstable behavior can affect the whole core, where the oscillations are in-phase for all fuel assemblies. During a core-wide in-phase oscillation, the pressure drop across the core is oscillating and mainly determined by the loop dynamics. For a boiling water reactor, this would involve the recirculation pump loop. For the case of interest here, the HPLWR has no recirculation pump loop. The loop dynamics are given by the flow path through all three heat-up
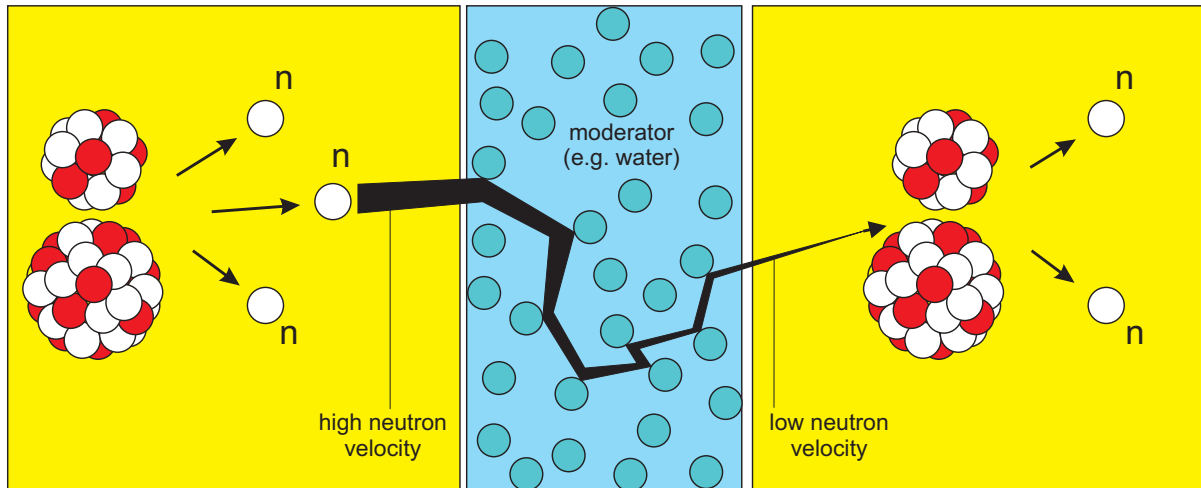
Figure 9.1: Scheme of a chain reaction in a nuclear reactor with thermal neutron spectra. During a fission event in the fuel rod, fast neutrons are released (left hand side). These neutrons are moderated by collisions with the fluid (center). After moderation, the thermal neutrons can induce a new fission process (right hand side).

stages and the components of the direct cycle. In particular, the transfer function of all pipes, turbines, heat exchanger, and so on influences the feed back of the oscillation at the inlet flow. At the present state of this work, no detailed loop characteristics of the HPLWR is available. However, the amount of unstable fuel assemblies can be sufficiently small, so that on the one hand, the total mass flow of the core is approximately determined by the fuel assemblies in steady-state conditions (Figure 9.2) (a thermal-hydraulic decoupled situation). On the other hand, the amount of unstable fuel assemblies can be large enough to require coupled neutronic analysis. This situation can occur if a whole fuel assembly cluster oscillates as one unstable thermal-hydraulic unit and is subsequently referred to as in-phase oscillation. The coupling scheme of an in-phase oscillation is given in Figure 9.3. For the neutron dynamics, a point-kinetic model is applied, providing the neutron density to the fuel rod model. The fuel rod model determines the average fuel temperature, which induces a reactivity feedback to the neutronic model. The average fuel temperature yields the heat flux, which is transfered from the cladding surface to the fluid in the fuel assemblies. Density changes due to heat flux changes are calculated by the thermal-hydraulic model. The variation in average density of the fluid leads to a second reactivity feedback path for the neutronic model.

The second type of reactivity instability is the out-of-phase oscillation. In this type of DWO, half of one heat-up stage of the HPLWR azimuthally behaves to the other half. The oscillations in fluid and power generation characteristics have a 180° phase shift (out-of-phase) in each half. To give an example, when the power rises in one half of the heat-up stage, it is reduced by the same amount in the other half. The average power remains essentially constant. This situation does not require changes in the total inlet flow of the whole core, because the two oscillating regions adjust their mass flow to maintain equal pressure drop across the core (Figure 9.2). The out-of-phase oscillation can be modeled by two thermal-hydraulic flow channels with two separate point-kinetic models and fuel rod models (two sub-models). These two sub-models are coupled by common
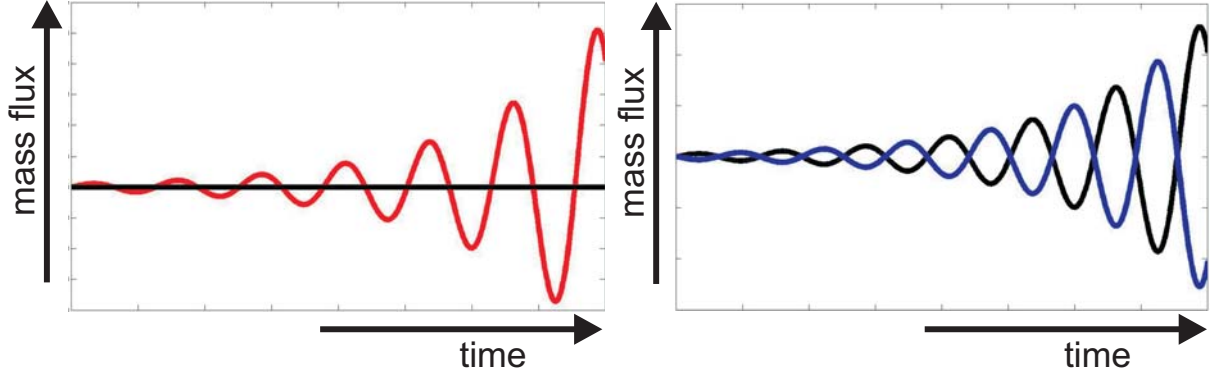
Figure 9.2: Schematic response of the thermal-hydraulic system for two types of reactivity instabilities in time. The in-phase oscillation is shown on the left hand side. Here, the mass flux of the unstable fuel assembly cluster oscillates in the linear unstable region (red curve), while the 51 other fuel assembly clusters stay in steady-state conditions (black line). The out-of-phase oscillation is shown on the right hand side. Half of one heat-up stage of the HPLWR core (blue curve) azimuthally behaves with a 180° phase shift to the other half (black curve).

inlet and outlet plena. The total mass flow of the core, $w_t$, is given by the sum of mass flow, $w_i$ ($i = 1 \bar{\vee} 2$), in each core half.

$$w_t = w_1 + w_2 = \text{constant} \quad . \tag{9.1}$$

If the flow in channel one decreases, the flow increases in channel two by the same amount, and the total flow remains unchanged. The strength of the thermal-hydraulic coupling is essentially defined by the pressure drop in the lower plenum of the HPLWR ($\Delta p \approx 65$ kPa [56]). Beside different boundary conditions, the scheme of the coupled calculation is the same as the in-phase oscillation given in Figure 9.3.

## 9.2  Point-Kinetic Model

A simplified model of the reactor dynamics is given by the point-kinetic equations [18]. The name "point-kinetic" is somehow misleading, because the reactor is not treated as a single point. The idea of this model is that the spatial dependence of the neutron flux, $\Phi(\mathbf{r}, t)$, can be described by a single spatial mode, the so-called fundamental mode, $\Psi(\mathbf{r})$. In this way, a separation ansatz for space and time is applied:

$$\Phi(\mathbf{r}, t) = v_n n(t) \Psi(\mathbf{r}) \quad , \tag{9.2}$$

$$C_i(\mathbf{r}, t) = C_i(t) \Psi(\mathbf{r}) \quad , \tag{9.3}$$

where $v_n$ is the velocity of the neutrons, $n(t)$ is the neutron density, and $C_i$ are the delayed neutron precursors. The spatial flux shape does not change with time. The time evolution of the neutron density $n(t)$ can be represented by

$$\frac{dn}{dt} = \frac{\rho_{\text{reactivity}} - \beta}{\Lambda_{\text{gen}}} n(t) + \sum_{i=1}^{6} \lambda_i C_i(t) \tag{9.4}$$

$$\frac{dC_i}{dt} = \frac{\beta_i}{\Lambda_{\text{gen}}} n(t) - \lambda_i C_i(t), \quad i = 1, \ldots, 6 \quad . \tag{9.5}$$
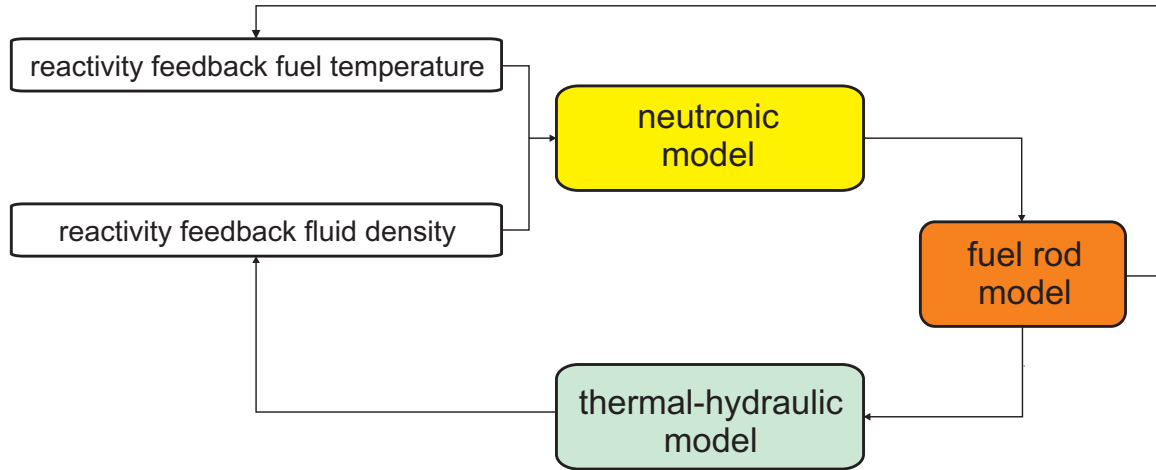
Figure 9.3: Scheme of the coupled thermal-hydraulic/ neutronic calculation. The neutronic model provides the neutron density to the fuel rod model. The fuel rod model determines the average fuel temperature, which induces a reactivity feedback to the neutronic model, and the heat flux which is transfered from the cladding surface to the fluid in the fuel assemblies. Density changes due to heat flux changes of the fluid are calculated in the thermal-hydraulic model. The change in average density of the fluid leads to a second reactivity feedback path for the neutronic model.

This is a set of seven coupled ordinary differential equations, which describes the transient of neutron population and the decay of the delayed neutron precursors. The reactivity $\rho_{\text{reactivity}}$ gives the fraction of new generated neutrons of the whole neutron population during the mean life time of one neutron generation. It is defined as the deviation of the multiplication factor, k, from the critical value ($k = 1$)

$$\rho_{\text{reactivity}} = \frac{k-1}{k} \quad .$$

(9.6)

The mean neutron generation time, $\Lambda_{\text{gen}}$, is given as

$$\Lambda_{\text{gen}} = \frac{l}{k} \quad ,$$

(9.7)

where l is the life time of the prompt neutrons. Most of the fission neutrons appear promptly after the fission event. A small fraction $\beta$ ($\beta \approx 0.7\%$) is emitted with appreciable time delay and can be divided into six delayed neutron groups. For each of these groups, one concentration balance equation is formulated (Eq(9.5)) by the transient of the concentration $C_i$, the fraction $\beta_i$ of generated delayed neutrons and the reduction given by the decay constant $\lambda_i$ of respective delayed neutrons. Delayed neutrons which were generated in former generations are additional source terms in Eq(9.4).

$$\beta = \sum_{i=1}^{6} \beta_i$$

(9.8)

The parameters of the point-kinetic model are listed in Table-9.1 [59].

Table 9.1: Parameters of the point-kinetic model [59].

| fractions | | | decay constants | |
|---|---|---|---|---|
| $\beta_1$ | 0.038 | | $\lambda_1$ | 0.0127 s$^{-1}$ |
| $\beta_2$ | 0.213 | | $\lambda_2$ | 0.0317 s$^{-1}$ |
| $\beta_3$ | 0.188 | | $\lambda_3$ | 0.115 s$^{-1}$ |
| $\beta_4$ | 0.407 | | $\lambda_4$ | 0.311 s$^{-1}$ |
| $\beta_5$ | 0.128 | | $\lambda_5$ | 1.4 s$^{-1}$ |
| $\beta_6$ | 0.026 | | $\lambda_6$ | 3.87 s$^{-1}$ |

## 9.3 Fuel Rod & Heat Transfer Model

The neutron density, n(t), can be directly correlated with the instantaneous volumetric heat generation in the fuel:

$$q''' = w_f \Sigma_f n(t) v_n \quad , \tag{9.9}$$

where $w_f$ is the energy released per fission, $\Sigma_f$ is the macroscopic cross-section of a fission event and $v_n$ is the velocity of the neutron. The temperature in the fuel rod is formulated as a point model. The average temperature, $T_f$, of the fuel rod is expressed by the surface heat flux, q", of the fuel rod [65]

$$(c_{p,\text{fuel}} \, \rho_{\text{fuel}} \, V_{\text{fuel}}) \frac{\partial T_f}{\partial t} = V_{\text{fuel}} q''' - A_S q'' \quad , \tag{9.10}$$

where $c_{p,\text{fuel}}$, $\rho_{\text{fuel}}$, $V_{\text{fuel}}$, and $A_S$ are the heat capacity, the density, the volume and the surface area of the fuel, respectively. The surface heat flux yields the heat transfer from the fuel to the surface of the cladding

$$q'' = h_{\text{transf}}(T_f - T_C) \quad , \tag{9.11}$$

where $T_C$ is the local cladding temperature and $h_{\text{transf}}$ is [66]

$$h_{\text{transf}} = \left[ \left( \frac{r_f + t_c}{r_f} \right) \left( \frac{r_f}{4k_f} + \frac{1}{h_g} + \frac{t_c}{k_c} \right) \right]^{-1} \quad , \tag{9.12}$$

with $r_f$ and $t_c$ as the radius of the fuel rod and the thickness of the cladding. Furthermore, the thermal conductivity of the fuel, gap and cladding is $k_f$, $h_g$ and $k_c$. The heat transfer from the cladding surface to the coolant is given by

$$q'' = \alpha(T_C - T_{\text{bulk}}) \quad . \tag{9.13}$$

The heat transfer coefficient from the cladding surface to the bulk flow $\alpha$ is defined by the Nusselt number Nu, the thermal conductivity $\lambda_{th}$ and the hydraulic diameter $D_H$ as

$$\alpha = \frac{\text{Nu}\lambda_{\text{th}}}{D_H} \quad , \tag{9.14}$$

where the Dittus-Boelter equation for turbulent flow is applied:

$$\text{Nu} = 0.023\text{Re}^{0.8}\text{Pr}^{0.33} \quad . \tag{9.15}$$

The Reynolds number Re and the Prandtl Number Pr are given by Eq(2.5) and Eq(2.8), respectively. All parameters of the fuel rod and heat transfer model are listed in Table 9.2

Table 9.2: Parameters of the fuel rod and heat transfer model.

| $w_f$ | $2.81 \cdot 10^{-11}$ J/per event | $\Sigma_f$ | $1.08456$ m$^{-1}$ |
|---|---|---|---|
| $v_n$ | $5729.58$ m s$^{-1}$ | $c_{p,\text{fuel}}$ | $0.116 \cdot 10^3$ J kg$^{-1}$ K$^{-1}$ |
| $\rho_{\text{fuel}}$ | $10.96 \cdot 10^3$ kg m$^{-3}$ | $V_{\text{fuel}}$ per rod | $0.000148$ m$^3$ |
| $A_S$ per rod | $0.1055$ m$^2$ | $r_{\text{fuel}}$ | $3.35 \cdot 10^{-3}$ m |
| $t_c$ | $0.5 \cdot 10^{-3}$ m | $t_g$ | $0.15 \cdot 10^{-3}$ m |
| $k_f$ | $25.9$ W m$^{-1}$ K$^{-1}$ | $h_g$ | $0.78$ W m$^{-1}$ K$^{-1}$ |
| $k_c$ | $21.5$ W m$^{-1}$ K$^{-1}$ | | |

## 9.4 Reactivity Feedback

In general, reactivity is divided in an external part, $\rho_{r,\text{ext}}$, and an internal part, $\rho_{r,\text{int}}$. The external reactivity is determined by the position of the control rods. The internal reactivity depends on the reactivity feedback of the fuel and fluid dynamics. The reactivity, $\rho_{\text{reactivity}}$, is given by

$$\rho_{\text{reactivity}} = \rho_{r,\text{ext}} + \rho_{r,\text{int}} = \rho_{r,\text{ext}} + \rho_{r,T} + \rho_{r,\text{water}} \quad , \tag{9.16}$$

where the internal reactivity is the sum of reactivity of the fuel temperature $\rho_{r,T}$ and the reactivity of the fluid density $\rho_{r,\text{water}}$. The reactivity coefficients were determined by a coupled neutronic/ thermal-hydraulic steady-state analysis of a HPLWR fuel assembly by Schlagenhaufer [55]:

$$\rho_{r,T} = 2.5848 \cdot 10^{-9}(T_f)^2 - 1.93 \cdot 10^{-5}(T_f) + 0.21384 \quad , \tag{9.17}$$

$$\rho_{r,\text{water}} = -7.1 \cdot 10^{-9}(\bar{\rho})^2 + 4.24 \cdot 10^{-5}(\bar{\rho}) + 0.1688 \quad , \tag{9.18}$$

where $T_f$ is the average fuel rod temperature of Eq(9.10) and $\bar{\rho}$ is the average coolant density given by

$$\bar{\rho} = \frac{1}{L_H} \int_0^{L_H} \rho \quad . \tag{9.19}$$

With the (local) coolant density $\rho$ and $L_H$ is the active length of a fuel assembly.

## 9.5 Stability Maps for Coupled Thermal-Hydraulic / Neutronic DWO

Figure 9.4 shows the stability map obtained by the thermal-hydraulic model and the two coupled thermal-hydraulic/ neutronic models for uniformly heated channels with imposed pressure drop at supercritical pressure. The black line is the previously shown neutral stability boundary (NSB) of the single channel DWO. The NSB of the coupled thermal-hydraulic / neutronic out-of-phase DWO (brown line) has higher N$_{\text{P-PCH}}$s than the single channel DWO for high N$_{\text{P-SUB}}$s. For lower N$_{\text{P-SUB}}$s this is inverted. The crossover is around N$_{\text{P-SUB}} = 3$. The NSB of the coupled thermal-hydraulic/ neutronic in-phase DWO type is approximately at the same N$_{\text{P-PCH}}$s as the NSB for the out-of-phase DWO. As before, the left end of the green line indicates the operation point of an
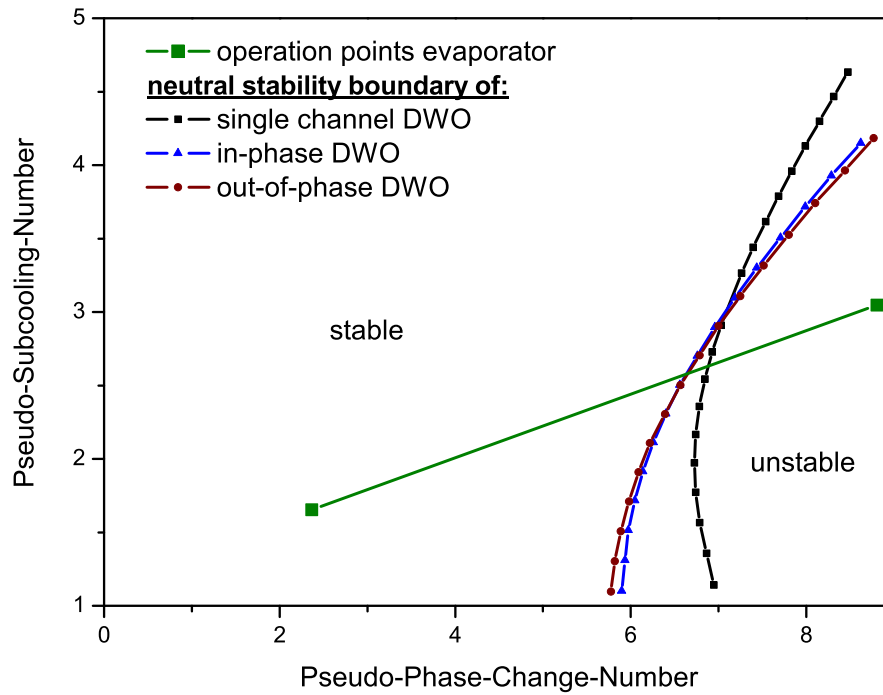
Figure 9.4: The stability map for different types of DWOs is shown. The black line is the previously shown neutral stability boundary (NSB) of the single channel DWO. The NSB of the coupled thermal-hydraulic/ neutronic in-phase and out-of-phase DWOs is plotted in blue and brown, respectively. The green line is the operations points of the evaporator stage of the HPLWR.

average evaporator fuel assembly and the right end indicates a hot fuel assembly of the evaporator. Therefore part of the hot fuel assemblies of the evaporator stage are in the linear unstable region. Thus, an inlet orifice is needed to assure a stable operation of the evaporator stage of the HPLWR.

# 10 Consequences for Design of HPLWR

At this point, the findings from the different analyses can be employed to fix design parameters to assure a stable operation of the HPLWR. In Section 6.6 it is shown that the most effective design change is the installation of orifices at the entrance of otherwise unstable FA. These orifices are customized for a hot FA.

For the case of boiling water reactors, the operation point of the average heated FA should correspond to a decay ratio less than 0.5 for the single channel DWO, and a decay ratio less than 0.25 should correspond to the coupled thermal-hydraulic/ neutronic DWO (reactivity DWO) [64]. Furthermore, the whole operation range, also including hot FAs, should be in the linear stable region of the stability map. Note that the decay ratio is defined in Section 6.2 as:

$$DR = exp\left[-2\pi\frac{Re(\Lambda)}{|Im(\Lambda)|}\right] \quad, \tag{10.1}$$

where $Im(\Lambda)$ and $Re(\Lambda)$ are the imaginary part and the real part of the leading mode at given operation parameters. Hence, the decay ratio should be below 1 for the whole operation range. The stability guidelines of BWRs are extended for the FA of HPLWR heat-up components (evaporator, superheater I and superheater II).

A typical FA of the HPLWR has a total length of 4.887 m [23] with an active length of 4.2 m (the detailed design parameters are given in Table 11). Since no axial power profile is available, a uniform heat-up is assumed. The resulting decay ratios (DR) of the linear stability analysis for fuel assemblies of all three HPLWR heat-up components are listed in Table 10.1. For the cases shown here (the single channel DWO, the in-phase DWO, and the out-of-phase DWO), no inlet and outlet orifices are applied. It can be seen that even without applying orifices, the average and hot FAs of the superheaters fulfill the stability criterion for all three types of DWO. In contrast, average FAs of the evaporator have a decay ratio larger than 0.25 at normal operation parameters for the in-phase and out-of-phase DWO. Furthermore, hot FAs of the evaporator would operate in the linear

Table 10.1: Decay ratios for HPLWR III-pass core heat-up components without orifices.

|  | single channel DWO | in-phase DWO | out-of-phase DWO |
|---|---|---|---|
| average evaporator | 0.034 | 0.5 | 0.52 |
| hot evaporator | 2.25 | 1.19 | 1.18 |
| average superheater I | 0.018 | 0.035 | 0.039 |
| hot superheater I | 0.041 | 0.061 | 0.065 |
| average superheater II | 0.010 | 0.022 | 0.041 |
| hot superheater II | 0.013 | 0.043 | 0.048 |

unstable region. Thus, while the FAs of the superheaters do not need additional inlet flow restriction, all the FAs of the evaporator stage must have inlet orifices. At that way, the evaporator has two sets of orifices. Each fuel assembly cluster has an orifice at the entrance of the diffuser. This orifice adjusts the mass flow so that the coolant of clusters at different positions in the evaporator approximately reaches the same exit temperature. However, in Section 8.4 it is profen that cluster orifices have no stabilizing effect. Therefore, a second set of orifices is installed, resulting in a single orifice at the entrance of each FA in the evaporator.

Now, the stability analysis is done for different inlet loss coefficients, while an exit loss coefficient of 2.5 is assumed. In particular, the orifice coefficient of this single orifice is increased stepwise until the whole operation range of the evaporator is in the linear stable region, and further, until the normal operation point has a decay ratio less than 0.5 for the thermal-hydraulic DWO and less than 0.25 for the reactivity DWOs. Figure 10.1 shows the operation range of the evaporator (green line) in the stability map. With a loss coefficient of 15 for the single inlet orifice, the curves of neutral stability boundary for the in-phase (red) and out-of-phase DWO (blue) are at higher Pseudo-Phase-Change-Numbers than a hot FA of the evaporator. The same fact is valid for the curve of decay ratio 0.5 for the single channel DWO (black).

The pressure loss due to an orifice at the inlet of the evaporator FAs is given by [70]

$$\Delta p = K \frac{\rho_{\mathrm{in}} u_{\mathrm{in}}^2}{2} \quad , \tag{10.2}$$

where $\rho_{\mathrm{in}}$ is the density of the coolant for $T_{\mathrm{in}} = 310\,°\mathrm{C}$ (25 MPa). $u_{\mathrm{in}}$ is the inlet velocity of the coolant and $K$ is a geometry dependent pressure loss coefficient. For a square-edged orifice, the orifice loss coefficient is given by

$$K = \frac{4}{5} \left[ \left( \frac{D_1}{D_2} \right)^4 - 1 \right] \quad , \tag{10.3}$$

while $D_1$ and $D_2$ are the diameter of the flow channel and the reduced diameter by the orifice, respectively. The HPLWR fuel assembly has a cross flow area of 1826 mm$^2$. Thus, a square-edged inlet orifice should have a reduction of the cross-section area to 408 mm$^2$. The inlet orifices for FAs of the evaporator are illustrated in Figure 10.2 [22].

It has to be emphasized that for the dimensioning of the orifices, a uniform power profile is assumed. Once realistic power profiles for different burn-up stages of HPLWR are available, the methods presented here can be repeated. In particular for a power distribution similar to a bottom-peak shape, larger inlet loss coefficients might be necessary. Nevertheless, the fabrication of orifices with such loss coefficients is still possible, and a stable operation of the HPLWR can be assured.
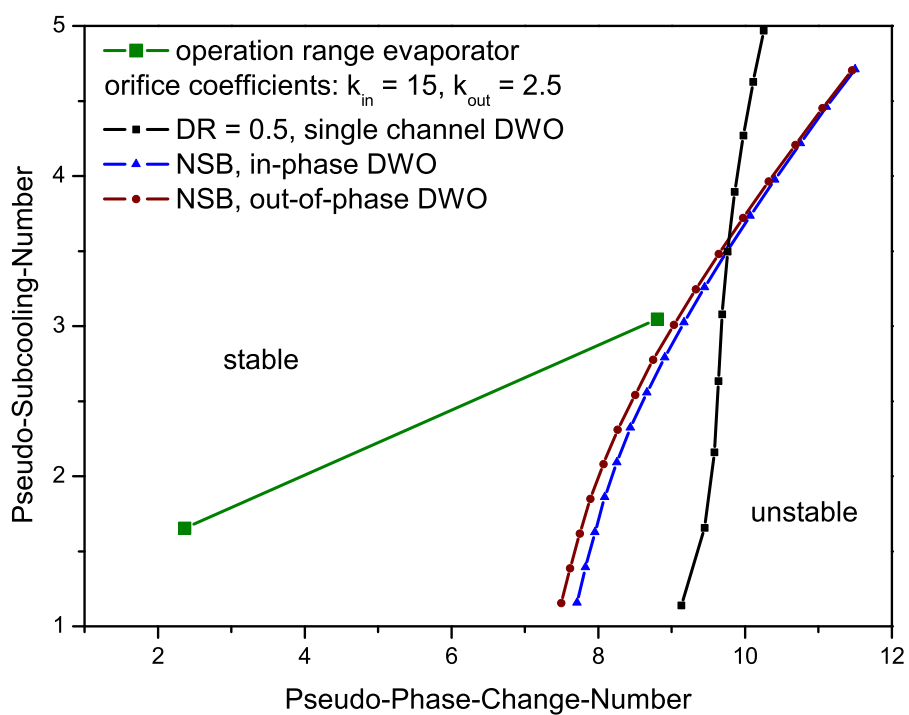
Figure 10.1: Neutral stability boundary is shown for the in-phase (red) and the out-of-phase DWO (blue), while an inlet loss coefficient of $K_{\text{in}} = 15$ and an outlet loss coefficient of $K_{\text{out}} = 2.5$ is applied. The curve of decay ratio 0.5 is given for the single channel DWO. The whole operation range of the evaporator (green line) is in the linear stable region.

Figure 10.2: Footpiece of FA cluster with inlet orifices.

# 11 Conclusions and Recommendation for Future Work

In this thesis for the first time a stability analysis for the High Performance Light Water Reactor (HPLWR) has been presented. This analysis is based on analytical considerations and numerical results, which were computed with a code developed by the author.

Within a HPLWR core, the working fluid experiences a drastic change in thermal and transport properties such as density, dynamic viscosity, specific heat and thermal conductivity as the supercritical water is heated from 280 °C to 500 °C. Even though water at supercritical pressure conditions is a single phase fluid, the density change substantially exceeds that in a Boiling Water Reactor (BWR). Due to these density changes, BWRs are - under certain operation parameters - susceptible to various thermal-hydraulic flow instabilities. For safe operation, flow instabilities have to be avoided. Even though at the present state of this thesis experimental data has not been obtained yet, theoretical considerations and experience from BWRs operation during five decades suggest that investigation of flow instabilities in the HPLWR are an inevitable necessity.

Compared to deployed BWRs or proposed alternative light water reactor concepts with supercritical pressure conditions (e.g. [71], [16], [45], [10]), the HPLWR provides many new design features which have a strong impact on the stability limits. This thesis is the very first work on stability analysis of the three-pass-core concept.

As a very first step, the core components have been classified with respect to the relevant flow instability phenomena. Modeling approaches successfully used for BWR stability analysis have been extended to supercritical pressure operation conditions. In particular, a one-dimensional equation set representing the coolant flow of HPLWR fuel assemblies has been implemented into the commercial software COMSOL. COMSOL provides an environment for modeling and solving the thermal-hydraulic equation set. A mayor advantage is that the same software platform can be used to perform steady-state, time-dependent, and modal analyses.

Steady-state analysis shows, that Ledinegg instabilities, flow maldistribution, and pressure drop oscillation do not occur at normal operation conditions of the HPLWR.

Stable and unstable operation regions of a nuclear reactor are indicated in stability maps. For BWRs these stability maps are spanned by two characteristic numbers, which commonly are the Phase-Change-Number $N_{PCH}$ and the Subcooling-Number $N_{SUB}$ [36]. In this thesis, new characteristic numbers for stability maps have been derived for fluids at supercritical pressure conditions. For subcritical pressures, the new non-dimensional

numbers reduce to the original $N_{PCH}$ and $N_{SUB}$ of phase change systems.

Density Wave Oscillations (DWO) are shown to be the most important instability phenomena in a HPLWR. Thus, the analysis of the time-dependent characteristic of the coolant flow becomes necessary. For BWRs, density wave oscillations are classified into two types. Both types of DWOs have been investigated at supercritical pressure conditions. The first type are the single channel DWOs, where the parallel channel boundary condition is applied. The second type are the reactivity DWOs, which involve core neutronic considerations. In order to determine the onset of instability for the single channel DWOs, the thermal-hydraulic model is linearized about its steady-state and solved in the frequency domain for the eigenvalues. The numerical approach used in this thesis, provides a method in which for the first time in the field of nuclear reactor stability analysis the resulting eigenvalues are almost independent of the nodal solution.
The obtained numerical data is presented in new stability maps. The most limiting pair of conjugated complex eigenvalues yield the neutral stability curve (NSB), separating linear stable from linear unstable operation regions for HPLWR. The sensitivity on various design and operation parameters of NSB is investigated. Results are summarized in a table. Thus, the effect on stability caused by future design changes of the HPLWR can be estimated. In particular, the influence of inlet and outlet orifices, active length, hydraulic diameter, flow direction and pressure drop on NSB are investigated. In accordance with the experience made for two-phase flow, the most effective design parameter to assure a stable operation is the implementation of orifices at the entrance of the fuel assemblies. Furthermore, it has been shown that employing an approximated state equation with linear slopes, which was done in previous works by other authors, leads to overly conservative results.

In general, stability investigations for a nuclear reactor include the analysis of the various power profiles, which results from different burn-up stages of the core. These power profiles are obtained by coupled thermal-hydraulic/ neutronic calculations with expense numerical effort. At the current state of the HPLWR project, there are no axial power profiles available. The effect of standard axial power profiles on the stability boundary is analyzed. The results are in qualitative agreement with calculations of boiling flow. As soon as power profiles are obtained in a future stage of the HPLWR project, the qualitative analysis presented in this thesis can be quantified.

The full non-linear thermal-hydraulic model is solved in the time domain. A delayed supercritical bifurcation is found. A subcritical secondary bifurcation emerges from the primary branch with a limit point at a bifurcation parameter higher than the bifurcation point of the primary bifurcation. The subcritical secondary bifurcation is associated with hysteresis effects. No instability phenomena are expected below the primary bifurcation which is governed by linear theory.Even though the supercritical bifurcation shows that stable non-linear limit cycles (with finite maximum amplitude in oscillation) exist close to the neutral stability boundary, the whole operation range of the HPLWR core components should be in the linear stable region, since oscillation amplitudes become large.

In a HPLWR core, nine fuel assemblies form one functional unit: the fuel assembly cluster. On the bottom of each cluster, a foot piece guides the coolant flow from the

lower plenum to the fuel assemblies. Each cluster can be viewed as an array of nine coupled parallel flow channels, where the foot piece is a common intermediate inlet plenum. In former HPLWR design proposals, there was a common inlet orifice at the entrance of the foot piece. By extending the thermal-hydraulic model to an array of nine flow channels, it is shown that a common inlet orifice has almost no effect on the onset of density wave oscillations. In order to avoid these instability modes, a design change is proposed, which foresees inlet orifices for each single fuel assembly of the evaporator. This type of arrangement is similar to that used in boiling water nuclear reactors.

Furthermore, the thermal-hydraulic model is coupled with a point-kinetic neutronic model via a heat transfer model. Two types of reactivity DWOs are identified: a core-region-wide out-of-phase DWO and an in-phase DWO. For both types, the neutral stability boundaries are determined and compared with the neutral stability boundary obtained for the single channel DWOs. It is found that the threshold of instability is approximately at the same values of Pseudo-Phase-Change-Numbers for all three types of DWOs. In particular, while for large Pseudo-Subcooling-Numbers the single channel DWOs are the limiting phenomena, for small Subcooling-Numbers the in-phase DWOs are the most limiting phenomena. In this thesis it is shown that the thermal-hydraulic COMSOL model can be coupled by a neutronic model to analyze the so-called first mode. In future stability analyses, the point-kinetic approach realized in this thesis should be extended by more sophisticated neutronic models.

It is shown in Chapter 10 that, while no inlet orifices are required for the fuel assemblies of the superheaters, the fuel assemblies of the evaporator must have individual inlet orifices at the entrance of each fuel assembly (to avoid DWOs). To design these inlet orifices, the stability criteria for BWRs are applied to for the HPLWR. A loss coefficient of 15 assures a stable operation of the evaporator.

The results of this thesis lead to design consequences for the HPLWR but they are also of general validity for all light water reactor concepts with supercritical pressure conditions like the PWR-SC [71], the US-SCWR [45] and pressure tube reactor concepts like the CANDU-SC [16].

# Nomenclature

## Roman Characters

| | | |
|---|---|---|
| $A_S$ | m$^2$ | surface area of fuel rod |
| $A_{x-s}$ | m$^2$ | flow cross-section of fuel assembly |
| $c_{p,\text{fluid}}$ | J kg$^{-1}$ K$^{-1}$ | specific heat capacity of the fluid |
| $c_{p,\text{fuel}}$ | J kg$^{-1}$ K$^{-1}$ | specific heat of fuel |
| $c_{p,\text{pc}}$ | J kg$^{-1}$ K$^{-1}$ | specific heat capacity at pseudo-critical conditions |
| $C_i$ | neutrons per m$^3$ | delayed neutron precursor |
| $\mathbf{d_a}$ | | mass term of PDE (COMSOL) |
| $D$ | m | diameter |
| $DR$ | | decay ratio |
| $D_H$ | m | hydraulic diameter |
| $e$ | J kg$^{-1}$ | total energy |
| $f$ | | friction factor |
| $\mathbf{F}$ | | source term of PDE (COMSOL) |
| $g$ | m s$^{-2}$ | gravity acceleration |
| $g_{\text{eff}}$ | m s$^{-2}$ | effective component of gravity acceleration |
| $G$ | kg m$^{-2}$ s$^{-1}$ | mass flux of fluid |
| $\mathbf{G}$ | | Neumann boundary conditions (COMSOL) |
| $G_{\text{tot}}$ | kg m$^{-2}$ s$^{-1}$ | total mass flux of core |
| $h$ | J kg$^{-1}$ | enthalpy of fluid |
| $h_A$ | J kg$^{-1}$ | enthalpy of water at 350°C and 25 MPa |
| $h_B$ | J kg$^{-1}$ | enthalpy of water at 404°C and 25 MPa |
| $h_f$ | J kg$^{-1}$ | enthalpy of saturated liquid |
| $h_{fg}$ | J kg$^{-1}$ | latent heat |
| $h_g$ | J kg$^{-1}$ | enthalpy of saturated steam |
| $h_{\text{in}}$ | J kg$^{-1}$ | enthalpy at the inlet of fuel assembly |
| $h_{L_H}$ | J kg$^{-1}$ | enthalpy at the exit of the heated length |
| $h_{\text{PC}}$ | J kg$^{-1}$ | enthalpy at pseudo-critical conditions |
| $h_{\text{transf}}$ | W m$^{-2}$ K$^{-1}$ | heat transmission coefficient (fuel to fluid) |
| $h_\lambda$ | J kg$^{-1}$ | reference enthalpy |
| $k$ | | multiplication factor |
| $k_c$ | W K$^{-1}$ m$^{-1}$ | thermal conductivity of the cladding |
| $k_f$ | W K$^{-1}$ m$^{-1}$ | thermal conductivity of the fuel |
| $K$ | | pressure loss coefficient |
| $K_{\text{in}}$ | | inlet pressure loss coefficient |

| | | |
|---|---|---|
| $K_{\text{out}}$ | | outlet pressure loss coefficient |
| $K_{\text{exit}}$ | | exit pressure loss coefficient |
| $l$ | s | life time of prompt neutrons |
| $L$ | m | channel length |
| $L_H$ | m | heated length |
| $n$ | neutrons per m$^3$ | neutron density |
| $\mathbf{n}$ | | normal vector on $\Omega$ |
| $p$ | N m$^{-2}$ | system pressure |
| $p_C$ | N m$^{-2}$ | pressure at thermodynamic critical point |
| $p_d$ | N m$^{-2}$ | dynamic pressure |
| $p_{\text{ex}}$ | N m$^{-2}$ | exit pressure |
| $p_{\text{G}}$ | N m$^{-2}$ | pressure of gas in accumulator |
| $p_{\text{in}}$ | N m$^{-2}$ | inlet pressure |
| $P_f$ | m | wetted perimeter |
| $P_H$ | m | heated perimeter |
| $q'$ | W m$^{-1}$ | linear heat rate |
| $q''$ | W m$^{-2}$ | heat flux |
| $\bar{q}''$ | W m$^{-2}$ | uniform heat flux |
| $q'''$ | W m$^{-3}$ | volumetric heat generation rate |
| $r_f$ | m | radius of the fuel pellet |
| R | J K$^{-1}$ mol$^{-1}$ | ideal gas constant |
| $\mathbf{R}$ | | Dirichlet boundary condition (COMSOL) |
| $t$ | s | time |
| $t_c$ | m | thickness of the cladding (fuel rod) |
| $T$ | °C | temperature of coolant flow |
| $T_{\text{bulk}}$ | °C | bulk temperature |
| $T_C$ | °C | temperature at thermodynamic critical point |
| $T_f$ | °C | average temperature of the fuel |
| $T_{\text{PC}}$ | °C | pseudo-critical temperature |
| $u$ | m s$^{-1}$ | velocity of fluid |
| $u_{\text{in}}$ | m s$^{-1}$ | velocity of fluid at the inlet of fuel assembly |
| $u_{L_H}$ | m s$^{-1}$ | velocity of fluid at the exit of the heated length |
| $u_s$ | m s$^{-1}$ | speed of sound in fluid |
| $v$ | m$^3$ kg$^{-1}$ | specific volume of fluid |
| $v_A$ | m$^3$ kg$^{-1}$ | specific volume of water at 350°C and 25 MPa |
| $v_B$ | m$^3$ kg$^{-1}$ | specific volume of water at 404°C and 25 MPa |
| $v_f$ | m$^3$ kg$^{-1}$ | specific volume of saturated liquid |
| $v_g$ | m$^3$ kg$^{-1}$ | specific volume of saturated gas |
| $v_{\text{inlet}}$ | m$^3$ kg$^{-1}$ | specific volume at the channel inlet |
| $v_{L_H}$ | m$^3$ kg$^{-1}$ | specific volume at the exit of the heated length |
| $v_n$ | m s$^{-1}$ | neutron velocity |
| $v_{\text{PC}}$ | m$^3$ kg$^{-1}$ | specific volume at pseudo-critical conditions |

| $V_G$ | m$^3$ | volume of gas in pressure holder |
| $V_{\text{fuel}}$ | m$^3$ | volume of the fuel |
| $w$ | kg s$^{-1}$ | flow rate |
| $w_f$ | J per event | energy released per fission event |
| $X$ | | quality |
| $X_{\text{exit}}$ | | quality at the exit of the heated channel |

# Greek Characters

| $\alpha$ | W K$^{-1}$ m$^{-2}$ | heat transfer coefficient |
| $\beta$ | | delayed neutrons fraction |
| $\beta_{\text{PC}}$ | K$^{-1}$ | linear isobaric thermal expansion coefficient |
| $\Delta p$ | N m$^{-2}$ | pressure drop |
| $\Delta p_{\text{pump}}$ | N m$^{-2}$ | pressure drop of the pump |
| $\Delta p_{\text{loop}}$ | N m$^{-2}$ | pressure drop of loop |
| $\varepsilon$ | m | mean height of roughness |
| $\Gamma$ | | flux function of PDE (COMSOL) |
| $\lambda$ | m | boiling boundary |
| $\lambda_i$ | s$^{-1}$ | decay constants of delayed neutrons |
| $\lambda_{\text{th}}$ | W m$^{-1}$ K$^{-1}$ | thermal conductivity |
| $\bar{\lambda}$ | | relative boiling boundary |
| $\Lambda$ | | eigenvalue |
| $\Lambda_{\text{Im}}$ | | imaginary part of eigenvalue |
| $\Lambda_{\text{gen}}$ | s | mean neutron generation time |
| $\Lambda_{\text{Re}}$ | | real part of eigenvalue |
| $\mu$ | Pa s | dynamic viscosity |
| $\mu_L$ | | Lagrangian multiplyier (COMSOL) |
| $\nu$ | m$^2$ s$^{-1}$ | kinematic viscosity |
| $\rho$ | kg m$^{-3}$ | density |
| $\rho_f$ | kg m$^{-3}$ | density of saturated liquid |
| $\rho_{\text{fuel}}$ | kg m$^{-3}$ | density of fuel |
| $\rho_g$ | kg m$^{-3}$ | density of saturated steam |
| $\rho_{\text{reactivity}}$ | | reactivity |
| $\rho_{\text{r,ext}}$ | | external reactivity (control rod) |
| $\rho_{\text{r,int}}$ | | internal reactivity (control rod) |
| $\rho_{\text{r},T}$ | | reactivity fuel temperature |
| $\rho_{\text{r,water}}$ | | reactivity fluid |
| $\omega$ | s$^{-1}$ | angular frequency |
| $\Omega$ | | numerical subdomain (COMSOL) |
| $\Omega_\rho$ | s$^{-1}$ | characteristic frequency of fluid expansion |
| $\bar{\Omega}_\rho$ | s$^{-1}$ | channel averaged frequency of fluid expansion |
| $\Phi$ | m$^{-2}$ s$^{-1}$ | neutron flux |

| $\underline{\Psi}$ | | vector of flow vairables |
|---|---|---|
| $\underline{\tilde{\Psi}}$ | | eigenfunction |
| $\Sigma_f$ | m$^{-1}$ | macroscopic cross-section of fission event |
| $\tau_w$ | kg m$^{-1}$ s$^{-2}$ | wall shear stress |
| $\zeta$ | | variable in numerical domain (COMSOL) |

# Characteristic Numbers

| Fr | Eq(2.7) | Froude number |
|---|---|---|
| M | Eq(2.4) | Mach number |
| $N_{PCH}$ | Eq(3.3) | Phase-Change-Number |
| $N_{P\text{-}PCH}$ | Eq(3.21) | Pseudo-Phase-Change-Number |
| $N_{P\text{-}SUB}$ | Eq(3.22) | Pseudo-Subcooling-Number |
| $N_{SUB}$ | Eq(3.4) | Subcooling-Number |
| Pr | Eq(2.8) | Prandtl number |
| Re | Eq(2.5) | Reynolds number |
| $\Lambda$ | Eq(3.2) | Euler number |

# Abbreviations

| | |
|---|---|
| BWR | Boiling Water Reactor |
| CANDU | CANada Deuterium-Uranium nuclear reactor |
| CANDU-SC | CANDU Super Critical water reactor |
| CFD | Computational Fluid Dynamics |
| DNB | Departure of Nuclear Boiling |
| DWO | Density Wave Oscillation |
| EPR | European Pressurized water Reactor |
| FA | Fuel Assembly |
| FEM | Finite Element Method |
| FFPP | Fossil Fired Power Plant |
| GFR | Gas-Cooled Fast Reactor |
| GIF | Generation IV International Forum |
| HPLWR | High Performance Light Water Reactor |
| LFR | Lead-Cooled Fast Reactor |
| LWR | Light Water Reactor |
| MSR | Molten Salt Reactor |
| NSB | Neutral Stability Boundary |
| PDE | Partial Differential Equation |
| PDO | Pressure Drop Oscillation |
| PWR | Pressurized Water Reactor |
| PWR-SC | Pressurized Water Reactor - Super Critical |
| RPV | Reactor Pressure Vessel |
| SCWR | Supercritical Water Reactor |
| SFR | Sodium-Cooled Fast Reactor |
| SWR | SiedeWasserReaktor |
| VHTR | Very High Temperature Reactor |

# Bibliography

[1] W. AMBROSINI, *On the analogies in the dynamic behaviour of heated channels with boiling and supercritical fluids*, Nuclear Engineering and Design, Volume 237, (2007), pp. 1164–1174.

[2] W. AMBROSINI AND M. SHARABI, *Dimensionless parameters in stability analysis of heated channels with fluids at supercritical pressures*, ICONE-14-89862, July 17-20, Miami, Florida, USA, (2006).

[3] W. ARNOLDI, *The principle of minimized iterations in the solution of the matrix eigenvalue problem*, Quarterly of Applied Mathematics, Volume 9, (1951), pp. 17–29.

[4] W. BEITZ AND K. GROTE, *Dubbel, Taschenbuch für den Maschinenbau*, Springer, 2001.

[5] B. BERGDAHL, F. REISCH, R. OGUMA, J. LORENZEN, AND F. AKERHIELM, *BWR stability investigation at Forsmark I*, Ann. Nuclear Energy, Vol. 16, No 10, (1989).

[6] A. BERGLES, P. GOLDBERG, AND J. MAULBETSCH, *Acoustic oscillations in a high pressure single channel boiling system*, Symposium on Two-phase Flow Dynamics, Eindhoven, (1967), pp. 535–550.

[7] D. BITTERMANN, D. SQUARER, T. SCHULENBERG, AND Y. OKA, *Economic prospects of the HPLWR*, Nuclear Engineering and Design, Volume 25, GENES4/ANP2003, Kyoto, Japan, (2003).

[8] D. BITTERMANN, J. STRAFLINGER, AND T. SCHULENBERG, *Turbine technologies for High Performance Light Water Reactors*, Proc. of ICAPP-04, Pittsburg, USA, (2004).

[9] J. BOURE, A. BERGLES, AND L.S.TONG, *Review of two-phase flow instability*, Nuclear Engineering and Design, Volume 25, (1973), pp. 165–192.

[10] J. BUONGIORNO, *An alternative SCWR design based on vertical power channels and hexagonal fuel assemblies*, Global-03, paper 1155-1162, New Orleans, USA, (2003).

[11] V. CHATOORGOON, *Supercritical flow stability in two parallel channels*, ICONE-14-89692, July 17-20, Miami, Florida, USA, (2006).

[12] C. COLEBROOK, *Turbulent flow in pipes, with particular reference to the transition region between smooth and rough pipe laws*, Jour. Inst. Civil Engrs., London, (1939).

[13] COMSOL, *Comsol chemical engineering library*, Tech. report, Version 2004, COMSOL, www.comsol.de, (2004).

[14] COMSOL, *Femalb user's guide*, Tech. report, Version 2004, COMSOL, www.comsol.de, (2004).

[15] C. CUVELIER AND A. SEGAL, *Finite Elements Methods and Navier-Stokes Equations*, D. Reidel Publishing Company, 1986.

[16] G. DIMMICK, N. SPINKS, AND R. DUFFEY, *An advanced CANDU reactor with supercritical water coolant: conceptional design features*, Pacific Basin Nuclear Conference, May 4-8, (1998).

[17] K. DOBASHI, Y. OKA, AND S. KOSHIZUKA, *Conceptual design of a high temperature power reactor cooled and moderated by supercritical light water*, Ann. Nuclear Energy 25, pages 487-505, (1998).

[18] J. DUDERSTADT AND L. HAMILTON, *Nuclear Reactors Analysis*, Cambridge University Press, 1976.

[19] K. FISCHER, E. GUELTON, AND T. SCHULENBERG, *Festigkeitsanalyse des Reaktordruckbehälters für einen Leichtwasserreaktor mit überkritischen Dampfzuständen*, Annual Meeting on Nuclear Technologies, paper-723, Karlsruhe, Germany, (2007).

[20] K. FISCHER, E. LAURIEN, A. CLASS, AND T. SCHULENBERG, *Design and optimization of a back-flow limiter for the High Performance Light Water Reactor*, GLOBAL 07, paper-175767, Boise, USA, (2007).

[21] K. FISCHER, E. LAURIEN, A. CLASS, AND T. SCHULENBERG, *Hydraulic analysis of a back-flow limiter for the High Performance Light Water Reactor*, Annual Meeting on Nuclear Technologies, Hamburg, Germany, (2008).

[22] K. FISCHER, T. REDON, G. MILLET, C. KOEHLY, AND T. SCHULENBERG, *Hydraulic analysis of a back-flow limiter for the High Performance Light Water Reactor*, ICCAP-08, paper-8050, Anaheim, USA, (2008).

[23] K. FISCHER, T. SCHNEIDER, T. REDON, T. SCHULENBERG, AND J. STARFLINGER, *Mechanical design of core components for a High Performance Light Water Reactor with a three pass core*, GLOBAL-07, paper-175772, Boise, USA, (2007).

[24] FRAMATOME ANP, *Technology European Pressurized Water Reactor (EPR)*, Tech. report, Paris, France, (2005).

[25] L. GORBAUCH, *Untersuchung eines HPLWR-Brennelements auf gekoppelte Thermohydraulische/ neutronische Stabilität*, master's thesis, University of Karlsruhe, 2008.

[26] H. OERTEL JR., *Prandtl-Führer durch die Strömungslehre*, Vieweg, 2002.

[27] H. OERTEL JR. AND M. BÖHLE, *Strömungsmechanik*, Vieweg, 2002.

[28] H. OERTEL JR. AND J. DELFS, *Strömungsmechanische Instabilitäten*, Springer-Verlag, 1996.

[29] H. Oertel Jr. and E. Laurien, *Numerische Strömungsmechanik*, Vieweg, 2003.

[30] S. Haaland, *Simple and explicit formulas for the friction factor in turbulant flow*, Trans. ASIVIE, Journal of Fluids Engineering 103, (1983), pp. 89–90.

[31] J. Heinecke, *Three pass core design proposal for a High Performance Light Water Reactor*, INES-2, November 26-30, Yokohama, Japan, (2006).

[32] J. Hofmeister, T. Schulenberg, and J. Starflinger, *Optimization of a fuel assembly for a HPLWR*, ICAPP-05, paper 5077, May 15-19, Seoul, Korea, (2005).

[33] J. Hofmeister, C. Waata, J. Starflinger, and E. Laurien, *Fuel assembly design study for a reactor with supercritical water*, Nuclear Engineering and Design, Volume 237, pp. 1513-1521, (2007).

[34] Informationskreis Kerntechnik, *www.kernenergie.de*, Inforum Verlags und Verlwaltungs Gmbh.

[35] S. Ishigai, *Steam Power Engineering, Thermal and Hydraulic Design Principles*, Cambridge University Press, 1999.

[36] Ishii and Zuber, *Thermally induced flow instabilities in two-phase mixtures*, Fourth International Conference On Heat Transfer, Paris, Vol. 5, paper B5.11, (1970).

[37] J. March Leuba and E. Blakeman, *A study of out-of-phase power instabilities in BWRs*, International Reactor Physics Conference, Jackson Hole, Wyoming, (1999).

[38] J. March Leuba and J. M. Rey, *Coupled thermo-hydraulic-neutronic instabilities in boiling water nuclear reactors: a review state of the art*, Nuclear Engineering and Design, Volume 145, (1993), pp. 97–111.

[39] R. Kiang, *Scaling criteria for nuclear reactor thermal hydraulics*, Nuclear Science and Engineering, Vol. 89, pages 207-216, (1985).

[40] R. Lahey Jr., *Modern development in multiphase flow and heat transfer; engineering applications of fractal and chaotic theory*, August 20-29, Karlsruhe, Germany, www.rpi.edu/laheyr/laheypub.html, (2001).

[41] C. Lanczos, *An iteration method for the solutions of the eigenvalue problem of linear differential and integral operators*, Journal of Research, Nat. Bu. Stand., 45, (1950), pp. 255–282.

[42] M. Ledinegg, *Unstabilität der Strömung bei natürlichem und Zwangsumlauf*, die Wärme 61, (1938), pp. 891–898.

[43] MathWorks Inc., *Matlab 7.1 user's guide, www.matlab.com*.

[44] L. Moody, *Friction factor for pipe flow*, Transaction of ASME, 66, 671-84, (1944).

[45] Y. Oka and S. Koshizuka, *Concept and design of a supercritical-pressure, direct-cycle light water reactor*, Nuclear Technology 103, pages 295-302, (1993).

[46] T. Ortega Gómez, A. Class, R. Lahey Jr., and T. Schulenberg, *Stability analysis of a uniformly heated channel with supercritical water*, ICONE 14, paper 89733, July 17-20, Miami, Fl, USA, (2006).

[47] T. Ortega Gómez, A. Class, R. Lahey Jr., and T. Schulenberg, *Density wave oscillations in coupled parallel channels under supercritical pressure conditions*, Proc. ANS/ENS International Winter Meeting, Washington DC, November 11-15, (2007).

[48] T. Ortega Gómez, A. Class, R. Lahey Jr., and T. Schulenberg, *Stability analysis of heated flow channels with supercritical water*, 3rd Internat. Symp. on Supercritical Water-Cooled Reactors - Design and Technology, Shanghai, China, March 12-15, (2007).

[49] T. Ortega Gómez, A. Class, R. Lahey Jr., and T. Schulenberg, *Stability analysis of a uniformly heated channel with supercritical water*, Nuclear Engineering and Design, status: Article in Press, Corrected Proof, (2008).

[50] T. Ortega Gómez, A. Class, R. Lahey Jr., and T. Schulenberg, *Thermal-hydraulic instabilities in a HPLWR fuel assembly*, Annual Meeting on Nuclear Technologies, Karlsruhe, Germany, (2008).

[51] M. Z. Podowski, *Modeling and analysis of two-phase flow instabilities*, NURETH-10, October 5-9, Seoul, Korea, (2003).

[52] F. Radermacher, *Balance oder Zerstörung*, Ökosoziales Forum Europa, 2002.

[53] R.T. Lahey Jr. and F. Moody, *The Thermal-Hydraulics of a Boiling Water Nuclear Reactor*, American Nuclear Society, 1993.

[54] P. Saha, M. Ishii, and N. Zuber, *An experimental investigation of the thermally induced flow oscillations in two-phase systems*, Journal of Heat Transfer, Trans. ASME, (1976), pp. 616–622.

[55] M. Schlagenhaufer, *Kritikalitätsrechnungen zu Reaktoren mit überkritischen Dampfzuständen*, master's thesis, University of Karlsruhe, 2007.

[56] T. Schneider, *Design proposal for the HPLWR three pass core - fuel assembly and core components*, master's thesis, University of Karlsruhe, 2007.

[57] T. Schulenberg, J. Starflinger, and J. Heinecken, *Three pass core design proposal for a High Performance Light Water Reactor*, 2nd COE-INES-2 International Conference on Innovative Nuclear Energy Systems, INES-2, Yokohama, Japan, 2006, (2006).

[58] M. Sharabi, W. Ambrosini, and S. He, *Prediction of unstable behaviour in a heated channel with water at supercritical pressure by CFD models*, Annals of Nuclear Energy, (2007).

[59] D. Smidt, *Reaktortechnik Band 1*, G. Braun, 1971.

[60] D. Smidt, *Reaktortechnik Band 2*, G. Braun, 1971.

[61] D. Squarer, T. Schulenberg, D. Struwe, Y. Oka, D. Bittermann, N. Aksan, C. Maraczy, R. Kyrki-Rajamäki, A. Souryi, and P. Dumaz, *High Performance Light Water Reactor*, Nuclear Engineering and Design, Volume 222, (2003), pp. 167–180.

[62] J. Suhwan, H. Shirahama, S. Koshizuka, and Y. Oka, *Stability analysis of supercritical light water-cooled reactor in constant pressure operation*, Proc. 9th Int. Conf. on Nuclear Engineering, Nice, France, April 12; ASME Paper No. 306, (2001).

[63] Y. Tin Tin, Y. Ishiwatari, J. Liu, S. Koshizuka, and Y. Oka, *Thermal and stability consideration of super LWR during sliding pressure startup*, ICAPP 2005, Paper 5383, May 15-19, Seoul, Korea, (2005).

[64] Y. Tin Tin, S. Koshizuka, and Y. Oka, *Linear stability analysis of a high-temperature supercritical-pressure light water reactor*, Global 2003, November 16-20, New Orleans, LA, USA, (2003).

[65] N. Todreas and M. Kazimi, *Nuclear Systems I, Thermal Hydraulic Fundamentals*, Taylor and Francis, 1989.

[66] N. Todreas and M. Kazimi, *Nuclear Systems II, Elements of Thermal Hydraulic Design*, Taylor and Francis, 1990.

[67] D. Torgerson, B. Shalabya, and S. Panga, *CANDU technology for Generation III+ and IV reactors*, Nuclear Engineering and Design, Volume 236, Issues 14-16, Pages 1565-1572, (2006).

[68] US Department of Defense , the orbiting Defense Meteorological Satellite Program (DMSP), *Korea at night: www.globalsecurity.org/.../dprk-dmsp-dark.jpg*.

[69] US DOE Nuclear Energy Research Advisory Committee, *A technology road map for Generation IV nuclear energy systems*, Technical report, Generation IV International Forum, (2002).

[70] Verein Deutscher Ingenieure, *VDI-Wärmeatlas*, Springer-Verlag, 2002.

[71] B. Vogt, J. Starflinger, and T. Schulenberg, *Near term application of supercritical water technologies*, ICONE-14, paper 89732, July 17-20, Miami, FL, USA, (2006).

[72] W. Wagner and A. Kruse, *The industrial standard IAWPS-IF97 for the thermodynamic properties and supplementary equations for other properties of water and steam*, Heidelberg, Springer, (1997).

[73] J. Whitlock, *The canadian nuclear FAQ*, www.nuclearfaq.ca, (2005).

[74] S. Wolfram, *The Mathematica Book*, Wolfram Media Inc 2004, 2004.

[75] G. Yadigaroglu, *Instabilities in two-phase flow*, Multiphase Flow and Heat Transfer, (1994).

[76] W. YANG AND N. ZAVALJEVSKI, *Preliminary stability analysis for supercritical water reactors*, Global 2003, Paper 87886, November 16-20, New Orleans, LA, USA, (2003).

[77] W. YANG AND N. ZAVALJEVSKI, *Effect of water rods on supercritical water reactor stability*, ICAPP 2005, Paper 5101, May 15-19, Seoul, Korea, (2005).

[78] J. ZHAO, P. SAHA, AND M. KAZIMI, *Analysis of flow instabilities in Supercritical Water-Cooled Nuclear Reactors.*, MIT Report -MIT-ANP-TR-105, (2004).

[79] J. ZHAO, P. SAHA, AND M. KAZIMI, *One dimensional thermal-hydraulic stability analysis of supercritical fluid cooled nuclear reactors*, ICONE-12-49075, Arlington, VA, USA, (2004).

[80] J. ZHAO, P. SAHA, AND M. KAZIMI, *Stability of Supercritical Water-Cooled Reactor during steady-state and sliding pressure start-up*, NURETH-11, Paper 106, October 2-6, Avignon, France, (2005).

[81] J. ZHAO, P. SAHA, AND M. KAZIMI, *Coupled neutronic thermal-hydraulic out-of-phase stability of Supercritical Water Cooled Reactors*, ICAPP-06, Paper 6424, June 4-8, Reno, NV, USA, (2006).

[82] N. ZUBER, *An analysis of thermally induced flow oscillations in the near-critical and super-critical thermodynamic region*, Final Report Nas8-11422, Nasa, May 25, (1966).

# Appendix I

Table .1: Design and geometry data of the HPLWR.

| | |
|---|---|
| system pressure | 25 MPa |
| thermal power | 2400 MW |
| electrical power | 1000 MW |
| net efficiency | 45 % |
| specific core power | 57.9 W m$^{-3}$ |
| height RPV | 14.3 m |
| inner diameter RPV | 4.47 m |
| amount of fuel assemblies in core | 1404 |
| fuel assemblies per fuel assembly cluster | 9 |
| fuel assemblies cluster per heat up stage | 52 |
| total length fuel assembly | 4.851 m |
| total length fuel rod | 4.710 m |
| active length | 4.2 m |
| edge length fuel assembly cluster (outer) | 0.2476 m |
| edge length fuel assembly (inner) | 0.06752 m |
| edge length moderator box (outer) | 0.02688 m |
| amount of fuel rods per fuel assembly | 40 |
| hydraulic diameter | 0.005336 m |
| diameter of fuel pellet | 0.0069 m |
| outer diameter fuel rod | 0.008 m |
| pitch to diameter | 1.18 |
| average fluid temperature at the inlet of RPV | 280 °C |
| average fluid temperature at the outlet of RPV | 500 °C |
| maximum peak temperature in core | 620-630 °C |
| mass flow in core | 1160 kg/s |
| mass flow in downcomer | 870 kg/s |
| mass flow of moderator | 193.3 kg/s |
| mass flow of gap water | 96.6 kg/s |